Pedro Mota Mendes
Master in Sciences of Biomedical Engineering

Correction of Spatial Distortion in Magnetic Resonance Imaging

Dissertation to Obtain the Degree of Master
in Biomedical Engineering

Adviser: Doctor Mário António Basto Forjaz Secca, FCT-UNL
Supervisor: Engineer Filipe José Janela Godinho, Siemens
Co-Adviser: Doctor Nicolas Francisco Lori, FCT-UC

Panel:

President:	Doctor Maria Adelaide de Almeida Pedro de Jesus, FCT-UNL
Examiner:	Doctor Pedro Manuel Cardoso Vieira, FCT-UNL
Vowel:	Doctor Mário António Basto Forjaz Secca, FCT-UNL
Vowel:	Engineer Filipe José Janela Godinho, Siemens

FACULDADE DE CIÊNCIAS E TECNOLOGIA
UNIVERSIDADE NOVA DE LISBOA

December, 2011

Pedro Mota Mendes
Master in Sciences of Biomedical Engineering

Correction of Spatial Distortion in Magnetic Resonance Imaging

Dissertation to Obtain the Degree of Master
in Biomedical Engineering

Adviser: Doctor Mário António Basto Forjaz Secca, FCT-UNL
Supervisor: Engineer Filipe José Janela Godinho, Siemens
Co-Adviser: Doctor Nicolas Francisco Lori, FCT-UC

Panel:

President:	Doctor Maria Adelaide de Almeida Pedro de Jesus, FCT-UNL
Examiner:	Doctor Pedro Manuel Cardoso Vieira, FCT-UNL
Vowel:	Doctor Mário António Basto Forjaz Secca, FCT-UNL
Vowel:	Engineer Filipe José Janela Godinho, Siemens

FACULDADE DE CIÊNCIAS E TECNOLOGIA
UNIVERSIDADE NOVA DE LISBOA

December, 2011

"Nenhuma ideia brilhante consegue entrar em circulação
se não agregando a si qualquer elemento de estupidez."

Fernando Pessoa

Aos meus pais!

Acknowledgments

Em primeiro lugar gostaria de agradecer ao Eng. Filipe Janela, meu supervisor na empresa, por me proporcionar a oportunidade de estagiar na Siemens SA, dando-me a possibilidade de um crescimento a nível pessoal e profissional.

Gostaria de agradecer ao meu orientador na FCT-UNL, o Prof. Mário Forjaz Secca, por sempre se mostrar disponível para me ajudar no projecto e pelo seu interesse pelo mesmo.

Também gostaria de agradecer ao meu orientador no IBILI, o Prof. Nicolás Lori, por sempre me desafiar neste projecto, tornando-o mais interessante e estimulante a nível académico.

Um agradecimento especial à Engª. Liliana Caldeira pela paciência e ajuda prestada ao longo do desenvolvimento deste projecto, contribuindo para um melhor trabalho.

Gostaria também de agradecer à Drª. Celina Lourenço, por toda a ajuda prestada na integração na empresa e por toda a orientação e organização do projecto.

Também gostaria de agradecer a todos os profissionais da Siemens SA que sempre se mostraram disponíveis para ajudar e contribuir para este projecto.

Um obrigado especial aos meus colegas de mestrado na empresa, especialmente à Catarina Runa por toda a ajuda e por todos os cafés que bebemos juntos e por todas as informações trocadas que tornaram o trabalho mais dinâmico.

Um grande agradecimento aos alunos de doutoramento da Siemens S.A., especialmente ao Eng. Filipe Soares e à Engª. Inês Sousa, por toda a ajuda e sugestões prestadas.

Gostaria ainda de agradecer ao IBILI e todos os seus profissionais, pela disponibilidade que sempre mostraram para ajudar no projecto.

A todos os colegas da faculdade que me apoiaram e ajudaram a crescer durante estes cinco anos, especialmente à Cátia Rocha por estar a meu lado em todos os momentos.

Gostaria de agradecer aos meus amigos de longa data Margarida Costa, Teresa Crespo e Tiago Ceia, por toda a amizade que mostraram ao longo destes cincos anos e que me ajudaram a crescer como pessoa.

Um agradecimento especial à Luisa Demétrio, por estar sempre a meu lado nos bons e nos maus momentos, levando-me a nunca desistir e seguir em frente com a cabeça levantada.

Por último, gostava de dar o maior dos agradecimentos a toda a minha família, em especial aos meus pais Francisco Mendes e Filomena Mendes por sempre me apoiarem nesta jornada da minha vida. Tudo o que consegui é também devido a eles.

Abstract

Magnetic Resonance Imaging (MRI) has been a major investigation and research focus among scientific and medical communities. So, new hardware with superior magnetic fields and faster sequences has been developed. However, these improvements result in intensity and spatial distortions , particularly in fast sequences, as Echo Plana Imaging (EPI), used in functional and diffusion-weighed MRI (fMRI and DW-MRI). Therefore, correction of spatial distortion is useful to obtain a higher quality in this kind of images.

This project contains two major parts. The first part consists in simulating MRI data required for assessing the performance of Registration methods and optimizing parameters. To assess the methods five evaluation metrics were calculated between the corrected data and an undistorted EPI, namely: Root Mean Square (RMS); Normalized Mutual Information (NMI), Squared Correlation Coefficient(SCC); Euclidean Distance of Centres of Mass (CM) and Dice Coefficient of segmented images. In brief, this part validates the applied Registration correction method. The project's second part includes correction of real images, obtained at a Clinical Partner. Real images are diffusion weighted MRI data with different *b*-values (gradient strength coefficient), allowing performance assessment of different methods on images with increasing *b*-values and decreasing SNR. The methods tested on real data were Registration, Field Map correction and a new proposed pipeline, which consists in performing a Field Map correction after a registration process. To assess the accuracy of these methods on real data, we used the same evaluation metrics, as for simulated data, except RMS and Dice Coefficient.

At the end, it was concluded that Registration-based methods are better than Field Map, and that the new proposed pipeline produces some improvements in the registration. Regarding the influence of *b*-value on the correction, it is important to say that the methods performed using images with higher *b*'s showed more improvements in regarding metric values, but the behaviour is similar for all *b*-values.

Keywords (Theme): Image Quality, Image Processing, Magnetic Resonance Imaging (MRI), Spatial Distortion Correction

Keywords (Technology): Diffusion-Weighed MRI (DW-MRI), Field Map Correction, Registration

Resumo

A Imagem por Ressonância Magnética (MRI) tem sido alvo de uma grande investigação e foco de pesquisa entre as comunidades científica e médica. Surgem então, novos hardwares com campos magnéticos superiores e sequências mais rápidas. No entanto, essas melhorias resultam em distorções de intensidade e espaciais, particularmente em sequências mais rápidas, como a imagem eco-planar (EPI), utilizada em ressonância magnética funcional (fMRI) e de difusão (DW-MRI). Portanto, a correção de distorções espaciais é útil para obter maior qualidade neste tipo de imagens.

Este projeto contém duas partes principais. A primeira parte consiste na simulação de dados MRI necessários para avaliar o desempenho dos métodos de *Registration* e otimizar os parâmetros dos mesmos. Para avaliar os métodos, foram calculadas cinco métricas de avaliação entre os dados corrigidos e um EPI sem distorções, a saber: Root Mean Square (RMS); Normalized Mutual Information (NMI), Squared Correlation Coefficient (SCC); Distância Euclidiana de Centros de Massa (CM) e Coeficiente Dice de imagens segmentadas. Em suma, esta parte valida os métodos de correção aplicados. A segunda parte do projeto inclui a correção de imagens reais, obtidas no parceiro clínico. As imagens reais são DW-MRI com diferentes valores de *b* (coeficiente de força de gradiente), permitindo a avaliação do desempenho de diferentes métodos em imagens com o aumento do *b* e a diminuição do SNR. Os métodos testados em dados reais são *Registration*, correção por *Field Map* e um *pipeline* proposto, que consiste em realizar uma correção por *Field Map* depois de um processo de *Registration*. Para avaliar estes métodos através de dados reais foram utilizadas as mesmas métricas de avaliação que para os dados simulados, exceto RMS e Coeficiente Dice.

No final, concluiu-se que os métodos baseados em *Registration* são melhores do que o método de correção por *Field Map*, e que o pipeline proposto tem algumas melhorias em relação ao *Registration*. Sobre a influência do valor *b* na correção é importante dizer que os métodos utilizados sobre imagens com valores de *b* mais elevados têm maiores melhorias dos valores das métricas, contudo o comportamento entre métodos é semelhante para todos os valores de *b*.

Palavras-Chave (Tema): Qualidade de Imagem, Processamento de Imagem, Imagem de Ressonância Magnética (MRI), Correção de Distorções Espaciais

Palavras-Chave (Tecnologia): Imagem de difusão de MRI (DW-MRI), Correção por Field Map, Registo

Contents

List of Figures

List of Tables

Acronyms

ADC	Aparent Diffusion Coefficient
BET	Brain Extraction Tool
CLI	Command-Line Interface
CSF	Cerebrospinal Fluid
CT	Computed Tomography
DOF	Degrees of Freedom
DTI	Diffusion Tensor Imaging
DW-MRI	Diffusion-Weighed MRI
EPI	Echo-Planar Image
FAST	FMRIB's Automated Segmentation Tool Brain Segmentation and Bias Field Correction
FFT	Fast Fourier Tranform
FID	Free Induction Decay
FLIRT	FMRIB's Linear Image Registration Tool
fMRI	Function MRI
FMRIB	Oxford Centre for Functional MRI of the Brain
FNIRT	FMRIB's Nonlinear Image Registration Tool
FOV	Field of View
FSL	FMRIB's Software Library
FUGUE	FMRIB's Utility for Geometrically Unwarping EPI's
GD	Gradient Descent
GM	Gray Matter
GPE	Phase Encoding Gradient
GRE	Gradient Echo Sequence
GRO	Readout Gradient
GSS	Slice Selection Gradient

GUI	Graphical User Interface
ITK	Insigth ToolKit
MI	Mutual Information
MPRAGE	Magnetization Prepared Rapid Acquisition Gradient Echo
MR	Magnetic Resonance
MRI	Magnetic Resonance Imaging
NMI	Normalized Mutual Information
NMR	Nuclear Magnetic Resonance
PD	Proton Density
PET	Positron Emission Tomography
POSSUM	Physics-Oriented Simulated Scanner for Understanding MRI
PRELUDE	Phase Region Expanding Labeller for Unwrapping Discrete Estimates
RF	Radio Frequency
SCC	Squared Correlation Coefficient
SD	Spatial Distortion
SE	Spin Echo Sequence
SNR	Signal-to-Noise-Ratio
SPECT	Single-Photon Emission Tomography
STDEV	Standard Deviation
TE	Echo Time
TI	Inversion Time
TR	Repetition Time
WM	White Matter

Chapter 1

Introduction

1.1 Scope

With the need and evolution of medical imaging, Magnetic Resonance (MR) appears as a technique that permits a high-resolution image without using any ionizing radiation. Consequently, Magnetic Resonance Imaging (MRI) has become a major investigation and research focus among scientific and medical communities. Due to this expansion, new hardware with superior magnetic fields and faster sequences has been developed, improving spatial and time resolution. However, these improvements result in intensity and spatial distortions that reduce the MRI quality [1], especially functional (fMRI) and diffusion-weighed MRI (DW-MRI).

Correction of spatial distortion is useful to obtain a higher image quality in faster sequences, such as echo-planar images (EPI), used in fMRI and DW-MRI. Without this correction, fMRI suffers from distortions, and all images used need to be geometrically similar. Also, DW-MR images present spatial distortions that need to be corrected, because the diffusion tensor or coefficient is calculated for each voxel [2], and without this spatial correction the voxel value corresponds to another position. Therefore, these calculated values in DW-MRI are wrong. Another advantadge of spatial distortion correction is the optimized comparison of images from other techniques, such as Computed Tomography (CT), Single-Photon Emission Tomography (SPECT) or Positron Emission Tomography (PET). Finally, another use for this correction is object measurement in MRI, since, if images are not corrected, volume and area measurements will not be accurate and cannot be compared with other measurements [3].

The main causes for spatial distortions can be related to hardware or to tissue [3]. In the second case, the correction is more difficult, as it cannot be characterized for a specific system. Regardless of the cause, every geometric distortion depends on the sequence used; and faster sequences like EPI produce a greater distortion [4]. Regarding EPI, the distortion occurs mainly in the phase-encoding direction [4].

In this study we will explore three methods for spatial distortion correction. These are Registration [5, 6], Field Map Correction [7–10] and a new proposed pipeline. The first two methods were

chosen because they are the most used in literature. Registration consists in aligning a distorted image to one that has no distortion. The image with no distortion can be an MRI (anatomical, functional or diffusion) or an image from another technique, such as CT or SPECT/PET. Field Map correction is a method that consists in calculating the phase map from two gradient echo images acquired with opposite phase-encoding directions, and the calculated field map can be used to correct the distortion of the original image. The new proposed pipeline consists in performing a Field Map correction after a registration process. This process can combine the advantages of both methods and therefore, it is expected to produce better results in EPI correction.

1.2 Presentation of the Project

This project consists in state-of-the-art evaluation regarding spatial distortion correction, and implementation of the most significant methods that are used nowadays. A study to achieve the optimal parameters of the two most important methods in literature will be done.

The principal objective of this project is to implement these methods and optimize them to be used in real medical images, having as a secondary objective the development of a prototype software, that integrates all these methods, to be used in Siemens Healthcare Sector's R & D Group in Portugal. Table 1.1 shows the project's work plan.

Table 1.1: Work Plan of the project

Month	Activity	1st W	2nd W	3tr W	4th W
December	Learn magnetic resonance imaging basics				
	Research data related to artefacts and correction of image distortions in MRI				
January	Learn magnetic resonance imaging basics				
	Choose the algorithms and software to correct the spatial distortion				
February	Detailed analysis of the chosen algorithms for spatial distortion				
March	Understand Siemens' world and in particular the Healthcare Sector				
	Familiarization with Siemens products and solutions				
	Basic formation on anatomy and physiology				
	Familiarization with development software				
	Writing a software manual for FSL				
April	Compare and evaluate algorithms related to spatial distortion correction				
May	Compare and evaluate algorithms related to spatial distortion correction				
June	Compare and evaluate algorithms related to spatial distortion correction				
	Optimization of algorithms for spatial distortion correction				
July	Compare and evaluate algorithms related to spatial distortion correction				
	Propose papers for conference				
	Optimization of algorithms for spatial distortion correction				
	Elaboration of a prototype software				
August	Optimization of algorithms for spatial distortion correction				
	Writing thesis				
September	Writing thesis				
	Revision of proposed paper for conference				

1.3 Contribution of the Work

This project will contribute to a better understanding of the several distortion correction methods in MRI and also provide a comparison between them to better understand the distortions. This study will offer the capability of choosing a method depending on the *b*-value in DW-MRI.

Finally, this thesis will output a prototype software where these several methods are implemented so, in the future, Siemens SA can use them in other projects and for future research in the MRI area.

1.4 Siemens SA Presentation

With 500 production centres in 50 countries and representation in 190 countries, Siemens is spread all over the world. In Portugal, Siemens S.A. encloses two factories, software research & development centres (Lisbon and Porto) and has a significant representation all over the country through its partners and company headquarters. Since 2008, the company is organized in three major sectors: Industry, Energy and Healthcare.

The **Industry Sector** and its solutions address Industry customers regarding production, transportation and building systems. This Sector is organized in five divisions: Industry Automation and Drive Technologies, Building Technologies, Industry Solutions, Mobility and OSRAM.

The **Energy Sector** offers products and solutions for generation, transmission and distribution of electrical energy. This Sector is organized in six divisions: Fossil Power Generation, Renewable Energy, Oil & Gas, Energy Service, Power Transmission and Power Distribution.

The **Healthcare Sector** stands for innovative products and complete solutions, as well as service and consulting in healthcare industry. This Sector is organized in three divisions: Imaging & Therapy Systems, Clinical Products and Diagnostics.

The Imaging & Therapy Systems provides imaging systems for diagnosis and therapy, as well as for a more effective prevention, namely Magnetic Resonance Imaging Systems (MR), Computer Tomography Systems (CT), Radiography and Angiography Systems, Positron Emission Tomography Systems (PET/CT), among others. These systems are networked with high-performance healthcare IT to optimize processes.

The Clinical Products Division focuses on specific market requirements with a dedicated strategy and providing complete and specific solutions for fields such women's health (mammography), urology and surgery, including also the ultrasound systems.

The Diagnostics Division covers business with in-vitro diagnostics, including immune diagnostics and molecular analysis. The Division's solutions range from point-of-care applications to automation of large laboratories.

Thus, Siemens Healthcare Sector is the first fully integrated diagnosis company, providing a complete technological portfolio for the entire supply chain in healthcare.

In Portugal, Siemens SA Healthcare Sector is a market leader in the healthcare area, known for its competence and innovation skills in diagnostic and therapy systems, as well as information technologies and systems' integration. In recent years, Siemens SA Healthcare Sector has promoted the contact and cooperation with key partners in the areas of science and biomedical technology, namely Universities and Research Institutes, establishing a knowledge network and strategic partnerships and thus promoting innovation, research and development in healthcare.

Today, the Healthcare Sector's R&D Group in Portugal is comprised by over 15 elements, working in strategic areas, such as Information Systems, Computational Imaging, Automatic Medical Imaging Analysis, Modeling and Decision Support Tools and Strategic Technology Evaluation. This work has already been demonstrated by one approved patent application, two filed invention disclosures and over ten scientific publications.

Recent Milestones in Portugal

- Breast Pathology Service in Hospital de São João in Porto, Hospital da Luz in Lisbon and Clínica Dr. João Carlos Costa in Viana do Castelo - first total patient focus units, including all necessary technologies for the complete clinical process;
- Hospital da Luz in Lisbon - first hospital in Portugal with SOARIAN® clinical information system, becoming one of the most modern health care installations in Europe;
- Clínica Quadrantes, in Lisbon - in-vitro diagnostics and information technology systems, which together with a PET/CT system, complemented the existing Siemens in-vivo diagnostic systems at the clinic;
- Universidade de Coimbra - 3 Tesla Magnetic Resonance Imaging System exclusively for neuroscience research. This unit is part of the Brain Imaging Network Grid, a scientific cooperation network which integrates the Universities of Coimbra, Aveiro, Porto and Minho.
- R & D Highlights:
  - Patent number DE 10 2007 053 393, System zur automatisierten Erstellung medizinischer Reports;
  - F. Soares, P. Andruszkiewicz, M. Freire, P. Cruz e M. Pereira, Self-Similarity Analysis Applied to 2D Breast Cancer Imaging, HPC-Bio 07 - First International Workshop on High Performance Computing Applied to Medical Data and Bioinformatics, Riviera, France (2007);
  - J. Martins, C. Granja, A. Mendes e P. Cruz, Gestão do fluxo de trabalho em diagnóstico por imagem: escalonamento baseado em simulação, Informática de Saúde - Boas práticas e novas perspectivas, edições Universidade Fernando Pessoa, Porto (2007);
  - F. Soares, M. Freire, M. Pereira, F. Janela, J. Seabra, Towards the Detection of Microcalcifications on Mammograms Through Multifractal Detrended Fluctuation Analysis, 2009 IEEE Pacific Rim Conference on Communications, Computers and Signal Processing, Victoria, B.C., Canada (2009).

Chapter 2

Magnetic Resonance

MRI is based on the nuclear magnetic resonance (NMR) phenomenon that was firstly described by Felix Bloch and Edward Purcell in 1946. In the beginning this technique was only used to study molecular structures and dynamics in the fields of physics and chemistry. 30 years ago, this technique was adapted by Lauterbur and Mansfield to be used for medical purposes, creating MRI [11].

2.1 Nuclear Magnetic Resonance

NMR is based on nuclear spins of Hydrogen atoms present in the human body. When a magnetic field (B_0) is applied to a volume the Hydrogen atoms starts to precessing at a specific frequency, the Larmor frequency (ω_0), in the orientation of the B_0 field, conventionally z or longitudinal orientation. This precessing frequency is also dependent of the gyromagnetic ratio of the element (γ), as showed by equation (2.1).

$$\omega_0 = \gamma B_0 \tag{2.1}$$

The sum of energy of the spins precessing is the magnetization M, and it is the base of NMR.

To create a MR signal, magnetization M needs to be moved from the longitudinal orientation to the transversal plane, for that, a pulse of radio frequency (RF) is used that consists in applying a magnetic field (B_1) during a short period of time (1-5 ms). This pulse rotates at ω_0 frequency in transversal plane in phase with the M vector, which provokes resonance of the Hydrogen spins [11, 12].

With this RF pulse, the M vector produces a magnetic field that can be measured by a transversal coil, applying the Faraday's law of induction. This signal tends to decay after the RF pulse, because the spins tend to orientate with the B_0 field. The decay is called Free Induction Decay (FID) and this is the simplest experience that can be done in MR.

The FID is described by the time constants T_1 and T_2. T_1 describes the relaxation along the main magnetic field B_0 direction (z axis) and is given by the equation (2.2), which is obtained by solving the Bloch equation when $M_z(0) = 0$.

$$M_z(t) = M_0 \left(1 - e^{-\frac{t}{T_1}}\right) \tag{2.2}$$

where M_0 is the initial magnetization. This equation can be described as an exponential curve, where T_1 is the time when magnetization M_z corresponds to 63% (figure 2.1a).

T_2 describes the loss of precession synchrony among the proton spins. This decay happens after the RF pulse is turned off and it is caused by loss energy in random collisions. This transversal loss of magnetization, M_{xy}, can be described by equation (2.3).

$$M_{xy}(t) = M_{xy}(0)e^{-\frac{t}{T_2}} \tag{2.3}$$

This equation is described by the exponential curve of figure 2.1b and T_2 corresponds to the time when transversal magnetization is 37% of the initial magnetization.

However, when a MR signal (FID) is acquired, the decay curve is not given by T_2, in fact it decays faster than T_2 (figure 2.1c). This fact can be explained by additional field inhomogeneities that contribute to a dephase of spins, and the time constant is T_2^*.

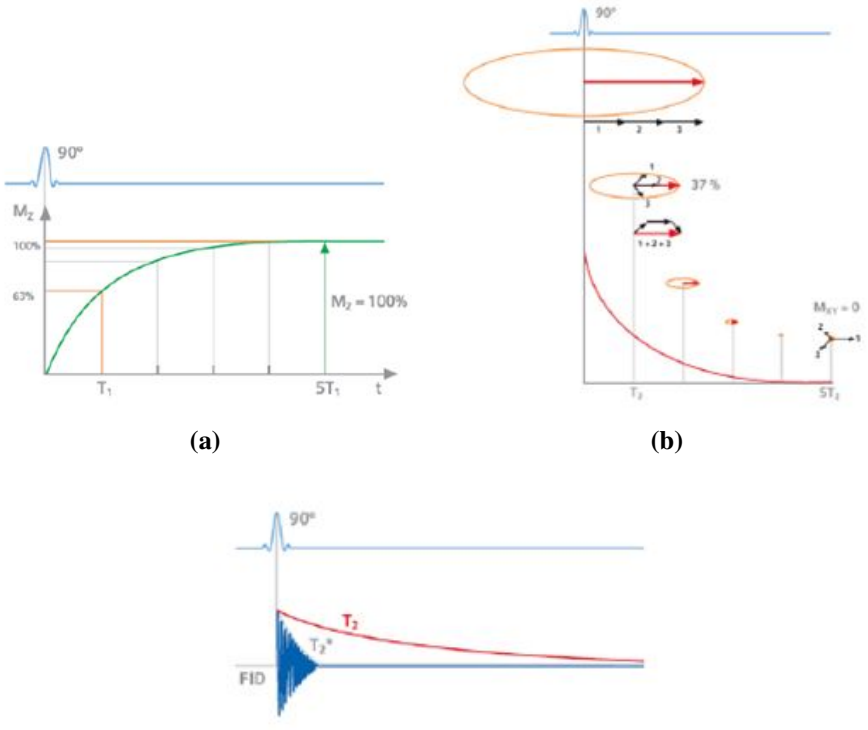

(a) **(b)**

(c)

Figure 2.1: Longitudinal (a), transverse (b) and T2* decay (c) [13]

2.2 Magnetic Resonance Imaging

MRI is a medical image technique based on NMR of the hydrogen atoms (protons) that exist in water, which is the most abundant substance in the human body. The great advantage of MRI relatively to other medical images, is that this technique does not use ionizing radiation, but conserves a high resolution. This technique also gives a variety of parameters that can be measured, such as proton densities (PD), relaxation times, temperature, proton motion, chemical shifts in Larmor frequencies and tissues heterogeneities that provide a great sensibility in a large range of tissues. Finally, this technique has the advantage of being capable of delivering structural and functional images that can improve the knowledge about the human body [11, 14].

2.2.1 Image Contrast

MRI images can be weighted by various parameters to emphasize different tissues, these parameters are T_1, T_2 and PD [14].

To acquire an image weighted in T_1 it is necessary to have a short repetition time (TR). TR is the time between two excitation RF pulses; in other words, it is the relaxion time that protons have between two excitation pulses. If a short TR is used (TR A in figure 2.2), several tissues with different T_1 have different MRI signal amplitudes. If the tissue has a short T_1, relaxation occurs faster and the signal is strong, but if the tissue has a long T_1, it does not have time to relax and the signal becomes weaker (figure 2.2). However, if a long TR (TR B in figure 2.2) is used, all the tissues have time for an almost complete relaxation and the signals of all tissues are similar and strong [14].

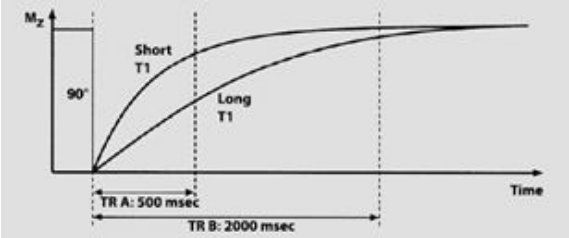

Figure 2.2: Relationship between TR and T1 contrast [14]

When a 90° RF pulse is applied, it surges the FID signal. However, to measure a MRI signal it is necessary to apply another RF pulse to realign the spins, this pulse is called 180° pulse. After a certain time surges a spin echo (figure 2.3a). The time between the 90° excitation pulse and the echo is called echo time (TE), and the 180º pulse occurs at $TE/2$. If another 180º pulse is applied after $TE/2$, another echo will appear with the gap time of TE after the first echo. If a series of 180° is applied pulses we can observe a decrease in the maximum of the echoes and from this decrease, T_2 can be measured as the time constant of the exponential decay (figure 2.3b) [14].

T_2 weighting is directly related to the TE. If a short TE is used (TE A of figure 2.4), the transversal magnetization does not have time to relax. Because of that, the decay occurs only at the beginning

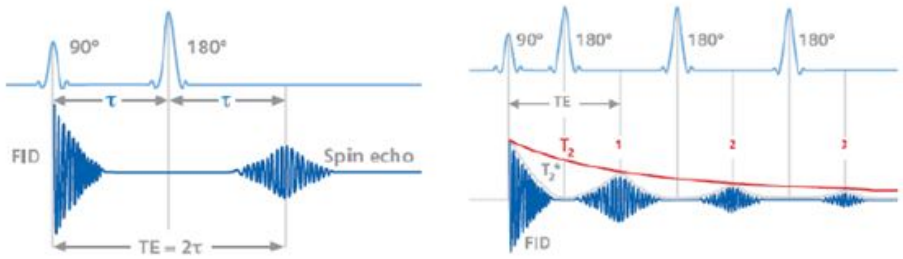

(a) **(b)**

Figure 2.3: Spin echo. Application of a single 180° RF pulse (a), multi-echo sequence (b) [13]

of the relaxation, so the different tissues with different T_2 are all present a strong signal and it is difficult to distinguish them. However, if a long TE is used (TE B of figure 2.4), relaxation occurs continuously and different tissues have different signals. If the tissue has a short T_2, the relaxation is already complete and the signal becomes weak, but if the tissue has a long T_2, the relaxation will not be complete and the signal is stronger [14].

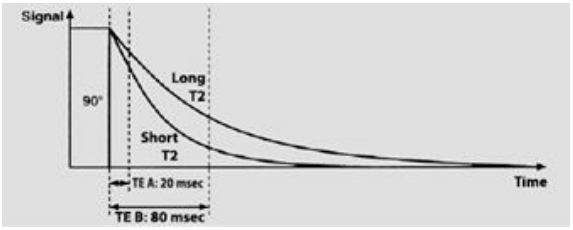

Figure 2.4: Relationship between TE and T2 contrast [14]

Finally, the PD is a weighting that indicates the quantity of protons existent in a certain tissue. To measure PD, it is necessary to adjust TR and TE to reduced the T_1 and T_2 effects in the MRI signal. The TR from the sequence needs to be long to permit a complete longitudinal relaxation of the spins, but the TE must be short, to reduce the effect of transversal relaxation, and so the signal contrast results from the quantity of protons that exists in the tissue and not from the different tissue's decay times [14].

2.2.2 Slice Selection and Spatial Encoding

To produce an MR image, the space must be codified, because with just the main magnet field B_0 all protons of the body have the same frequency and it is impossible to distinguish their position. To make that codification it is necessary to apply three spatial gradient fields G. The fields B_i that are applied to specific position r_i are given by equation (2.4).

$$B_i = B_0 + G \cdot r_i \tag{2.4}$$

These gradients used in MRI have a linear variation and they are applied in each direction (x, y and z). The gradients used in MRI are used for slice selection, frequency encoding and phase

encoding. These threes gradients plus the RF pulses and the data sampling periods are called pulse sequence, which is used to acquire a MR image [12].

In slice selection, direction z is encoded by applying a gradient in this direction (G_{SS}) at the same time as the RF pulse. The central frequency of the RF pulse determines the location in z where protons are excited when G_{SS} is applied, because every slice z_i is excited to a frequency ω_i determined by the gradient [12], as shown in figure 2.5.

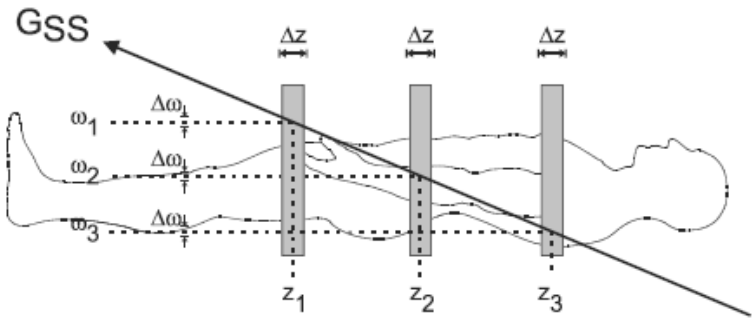

Figure 2.5: Slice selection process. In the presence of a gradient (G_{SS}), the total magnetic field that a proton experiences and its resulting resonant frequency depend on its position. Tissue located at position z_i will absorb RF energy broadcast with a centre frequency ω_i. Each position will have a unique resonant frequency. The slice thickness Δz is determined by the amplitude of G_{SS} and by the bandwidth of transmitted frequencies $\Delta\omega$. [12]

The slice thickness is related directly to the bandwidth of the RF pulse $\Delta\omega$. If the gradient is steeper, the slice will be thinner and if the gradient is shallower, the slice will be thicker [12].

Now that the slice selection in z direction is done, it is necessary to encode that slice, this is called spatial encoding and it is divided in two steps: frequency encoding and phase encoding, that encode the x and y axis [12].

The phase encoding gradient (G_{PE}) is normally applied along the y direction after the RF pulse and makes the protons precess at a different frequency, but when the gradient is turned off, all spins return to the original spin precessing frequency with different phase caused by the time of the gradient application, as figure 2.6 shows. So, all spins in the y-axis can be identified, only by their phase [12].

Finally the frequency encoding gradient or readout gradient (G_{RO}) is applied when the echo of the MR signal appears, making it so that only the region with a specific frequency is read [12]. The figure 2.7 shows the different frequencies ω_i corresponding to different spatial positions x_i.

2.2.3 Image Reconstruction

To understand the information given by the MR signal it is necessary to construct an image. The system acquires the echo with an analogue to digital converter and converts it from a time signal into a frequency signal applying a 1D Fast Fourier Transform (FFT), and this signal is stored in the k-space. k-space is a complex space that has the frequency in the k_x and the phase domain in

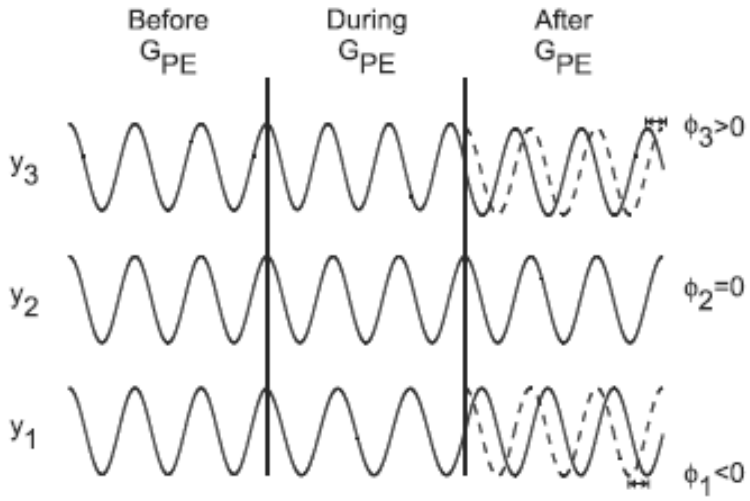

Figure 2.6: Concept of Phase Encoding. Prior to application of G_{PE}, all protons precess at the same frequency. When G_{PE} is applied, a proton increases or decreases its precessional frequency, depending on its position, y_i. [12]

the k_y (figure 2.8) [15].

In most of the sequences, the signal is acquired line by line, corresponding to a different phase each line defined by G_{PE}. In each line all the signals are acquired with different precessional frequencies generated by G_{RO}. The number of lines and columns in k-space corresponds to the frequency samples and phase encodings performed during the MRI signal acquisition. After all k-space is acquired an inverse 2D FFT is performed to transform phase and frequency information into contrast and spatial information [15].

2.3 Magnetic Resonance System

MR systems essentially consist in the main magnet, the magnetic field gradient system and the RF system, and can be represented by figure 2.9.

The main magnet is the principal component of the MR system and it aims to create a homogeneous and strong magnetic field. Presently, two types of magnets are used: the permanent magnets and the super-conducting magnets. The permanent magnets have a magnetic induction between 0.01 and 0.35 T, while the super-conducting magnets can reach values of 9 T, but they are more expensive because they require permanent cooling of liquid helium [13].

The magnetic field gradient system consists in three gradient coils responsible for producing the gradient fields used for slice selection and spatial encoding. To produce the field gradients, it is necessary to produce RF that need to be switched on and off at a very fast speed that can achieve 200 to 400 T/m/s, so the coils must be very reliable and stable. However, these coils have a maximum amplitude of 20 to 40 mT/m [13].

Finally, the RF system has the objective to transmit and receive the RF pulses for spin excitation

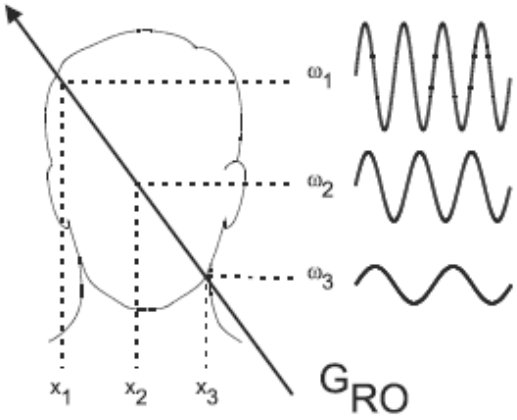

Figure 2.7: Readout Process. Following excitation, each proton within the excited volume (slice) precesses at the same frequency. During detection of the echo, a gradient (G_{RO}) is applied, causing a variation in the frequencies for the protons generating the echo signal. The frequency of precession ω_i for each proton depends upon its position x_i. [12]

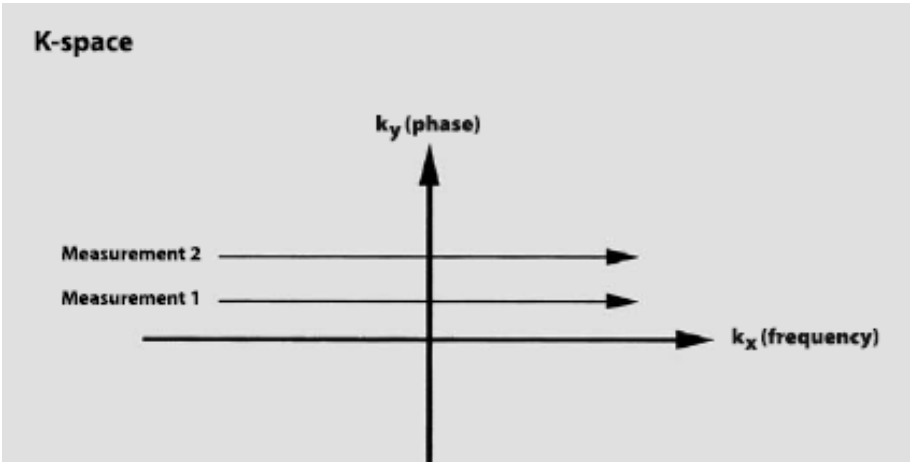

Figure 2.8: k-space. k_x is the frequency axis, k_y the phase axis. Data from each measurement fills a different horizontal line. [14]

and is constituted by the RF antennas (coils), the RF transmission amplifier and RF receiving amplifier [13].

2.4 MRI Pulse Sequences

A pulse sequence is a series of events such as RF pulses, gradient waveforms and data acquisition that produce the desired MRI signal. Different manufacturers of MRI systems use different acronyms to define a pulse sequence, and so in this thesis we will use Siemens acronyms. Generally, the pulse sequences can be grouped into one of the following [16]:

- Spin echo
  - Conventional Spin Echo

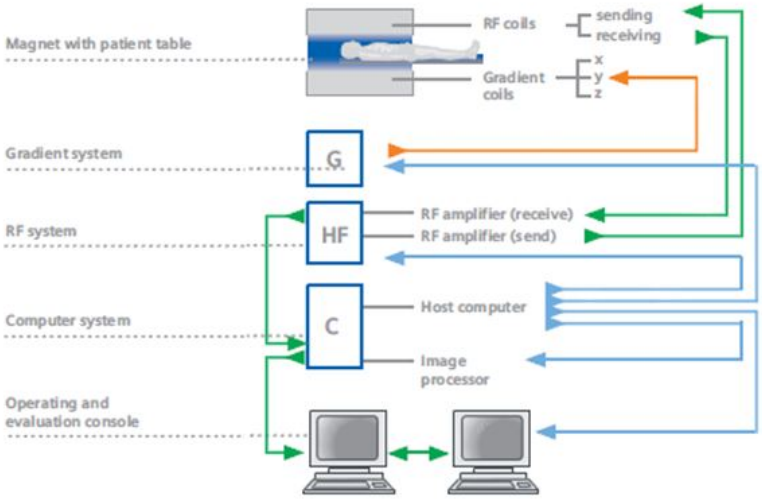

Figure 2.9: MRI system components [13]

  - Fast Spin Echo

- Inversion recovery
- Gradient echo
- Ultra-fast imaging

To produce a spin echo (SE) sequence, it is necessary to apply a 90º excitation pulse, followed by a 180º rephasing pulse (figure 2.10). This pulse sequence is the most used for the majority of MRI applications, because it is useful to show anatomy with a high Signal-to-Noise-Ratio (SNR).

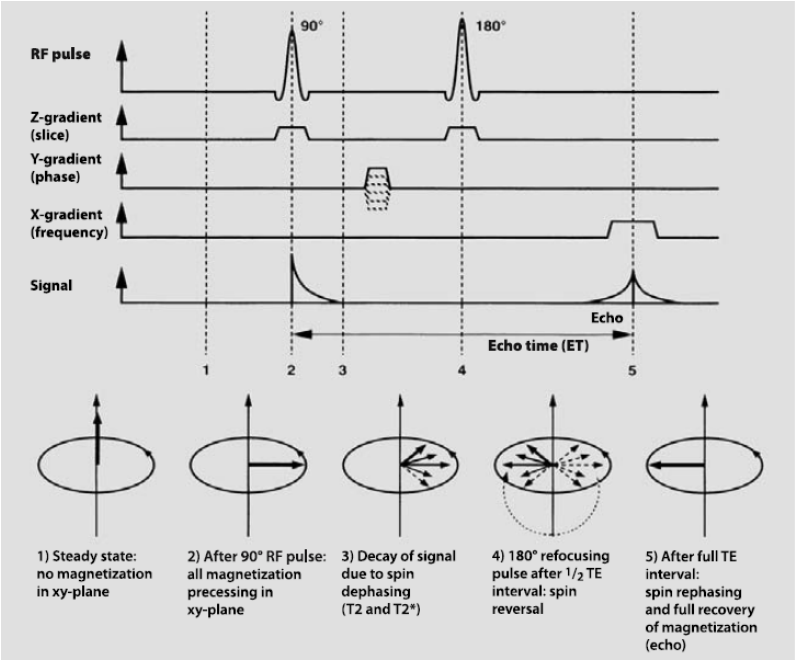

Figure 2.10: Spin Echo Sequence [14]

In fast spin echo sequences (TSE), only a pulse of 90º is used for the acquisition of more than one readout line, and after that, a train of 180º pulses is applied to acquire several lines (figure 2.11). This technique decreases the acquisition time, but can worsen image contrast.

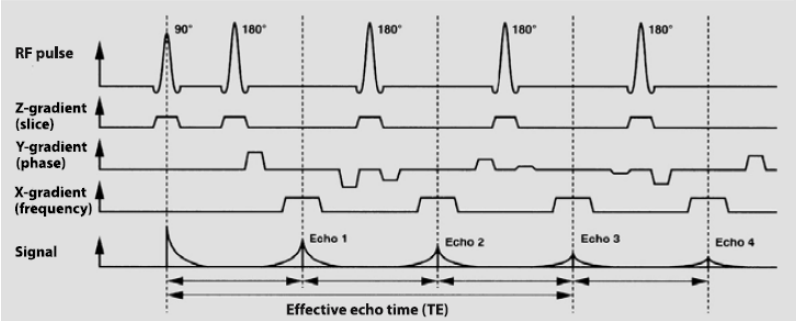

Figure 2.11: Fast Spin Echo Sequence [14]

The inversion recovery sequence (IR) consists in applying a 180º inversion pulse that changes the magnetization and after a time of inversion (TI), a 90º excitation pulse is applied to acquire the signal from transversal magnetization. This technique has the advantage to suppress some tissues, because if we choose the right TI, the tissue in cause can have a null longitudinal magnetization and will have no MR signal (figure 2.12).

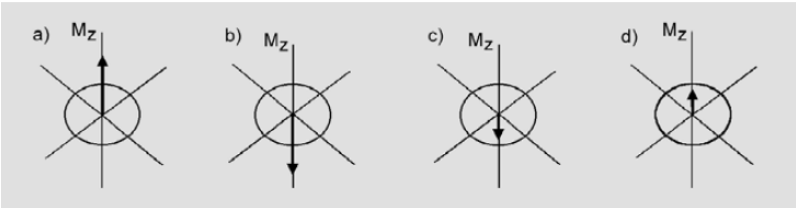

Figure 2.12: Inversion Recovery Sequence. Following the 180° inversion pulse (a), the longitudinal magnetization vector points in the opposite direction (b). T1 relaxation takes place from z to $+z$ (c, d). No signal forms as long as there is no vector component in the transverse plane (the null point of a tissue) [14]

The gradient echo sequence (GRE) has the principle to use a variable flip angle (α) pulse smaller than the 90º pulse. That makes the acquisition time shorter because TR can be smaller. After applying the flip angle pulse, a gradient is used to rephase the FID instead of the 180º pulse and create the echo (figure 2.13). The TE can become shorter and thus can the acquisition time. This sequence has the disadvantage that it cannot remove the field inhomogeneities, so the signal comes always with some weighting of T_2^*.

Recent research in MRI describes some pulse sequences that are capable of acquiring several slices in one breath hold. Usually, this technique uses GRE sequences where the excitation pulse is not totally applied, reducing the TE and so the time of acquisition. The most used ultra fast sequence is the echo-planar image (EPI) that can be done with SE and GRE. In this sequence, a slice of the k-space is acquired with a single excitation pulse just by generating multi echoes, and each phase is encoded by different slopes of gradient (figure 2.14). In a conventional SE sequence, the k-space is acquired line by line, usually from the left to the right, and with every new excitation pulse, begins a new line. On the other hand, EPI sequence has just one excitation pulse per slice,

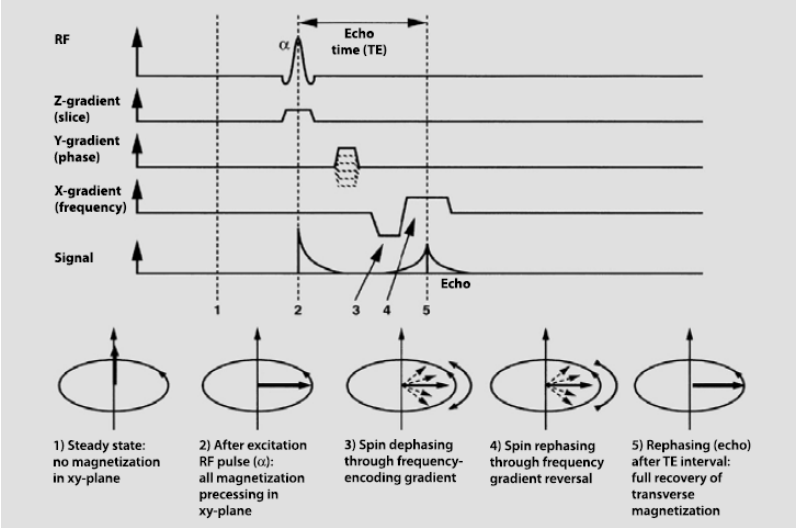

Figure 2.13: Gradient Echo Sequence [14]

so it is impossible to begin a new line. To resolve this problem a blip gradient is applied that inverts the field and a new line is acquired in the opposite direction. The great disadvantage of this sequence is that the resolution is lower compared with other MRI pulse sequences. However, this technique can produce very fast images that can be used in fMRI and DW-MRI.

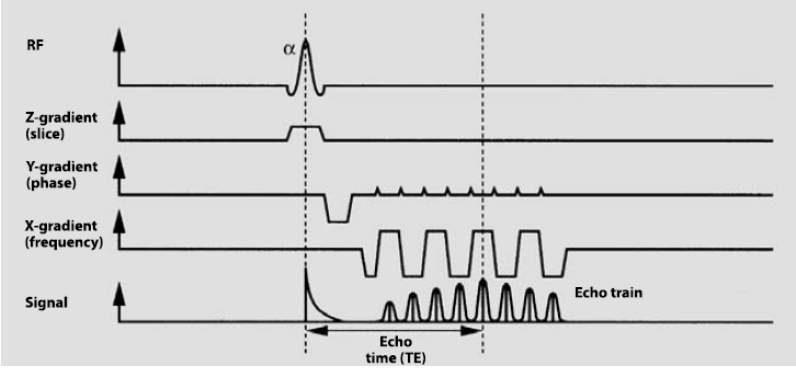

Figure 2.14: EPI Sequence [14]

2.5 Diffusion-Weighted MRI

DW-MRI is a technique that can show the motion of water molecules by diffusion, due to changes in the MR signal. Diffusion is characterized by the D value that is the diffusion coefficient that translates the amount of material transported across a membrane. The change of signal occurs because the MR signal of a biological tissue or fluid is dependent on the mean distance that a hydrogen atom moves. The loss of signal caused by the hydrogen movement, increases with the velocity of the particles in the magnetic gradient field. To measure the movement of the molecules and their direction the operator could change the strength and direction of the applied gradient field [14].

The standard method to measure diffusion movement consists in applying a pair of symmetric gradient pulses before and after the 180º RF pulse (figure 2.15). This will increase the dephased spins in a SE, and therefore they will not rephase at TE, producing a signal loss. This method was first developed by Stejskal and Tanner [12].

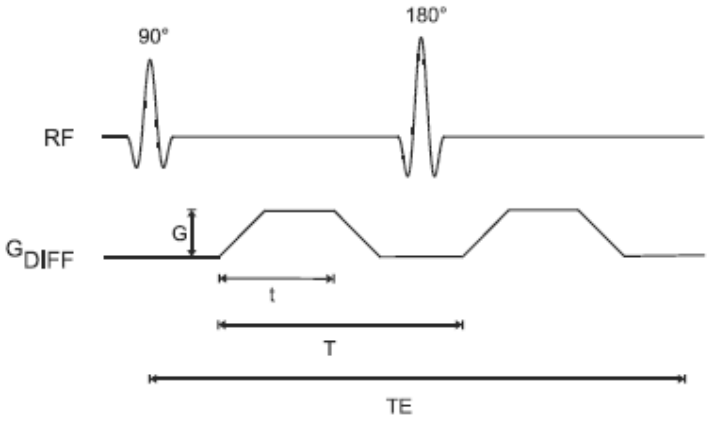

Figure 2.15: Spin echo pulse sequence showing diffusion gradients, known as the Stejskal–Tanner approach. G is the amplitude for each of the gradient pulses, t is the duration of the gradient pulse during which the diffusion weighting occurs, and T is the time between the two pulses. [12]

The sensitivity to the motion in this technique is measured by field strength coefficient (b-value) that can be calculated by equation (2.5). To obtain a greater sensitivity, it is necessary to have a higher b-value. For that, several options exist, such as larger gradient amplitudes (G), longer duration of gradient pulses (t) or longer times between pulses (T).

$$b = \gamma^2 G^2 t^2 (T - t/3) \tag{2.5}$$

The loss of signal can be described by equation (2.6).

$$S(TE) = e^{-TE/T2} * e^{-b*D} \tag{2.6}$$

It is very difficult to measure the diffusion coefficient D, because blood perfusion also causes diffusion movements that cause a loss of signal [12]. Therefore, the *apparent diffusion coefficient* (ADC) is measured, which is an approximation of the D value. To measure ADC, a set of images is acquired with different b-values and the ADC value is extrapolated from equation (2.6), replacing D by ADC [12].

To measure the diffusion in other directions, it is only necessary to change the gradient direction. With just 6 directions, the entire geometry representable by an ellipsoid can be calculated. This technique is called *diffusion tensor imaging* (DTI), which can also be performed with more directions. DTI is specially used for fibre tracking - tractography in the white matter, which consists in calculating the course of a fibre in the brain.

Chapter 3

Spatial Distortion

Artefacts in MRI are voxels that do not represent exactly the anatomy in study [12]. Some artefacts are easy to identify, but others are not, namely the artefacts that provoke a small variance in voxels. One approach to categorize artefacts is to divide them by the cause of signal misregistration [12] in three classes: Motion Artefacts, which include gross physical movement of the patient and internal physiologic motion such as cardiac and peristaltic movement and blood flow; Sequence/Protocol-Related Artefacts that are a consequence of a particular measurement technique or parameters; and External artefacts that are caused by a malfunction of the MR system or a source external to the patient and scanner. In this last one, we can include Spatial Distortions and Intensity Distortions. However, there are many other ways to classify artefacts. In this thesis only Spatial Distortions will be approached and also some methods for their corrections.

3.1 Spatial Distortion Causes

The Spatial Distortions, or according to some authors Geometric Distortions, in MRI can be classified into two groups: hardware-related and tissue-related, depending on the cause of the distortion. The hardware-related distortions are caused essentially by the inhomogeneity in the main magnet, the nonlinearity in the gradient fields and the eddy currents associated to switching gradient coils.

The magnet field's inhomogeneity is caused by deformations in the main magnet, which will produce a different magnetic excitation in the hydrogen atoms, and therefore will produce errors in the readings, because the spins are not excited in the way it was predicted. This can easily be corrected using shimming coils to adjust the inhomogeneities of the main magnet [3, 4, 12]. According to Wang and Doddrell [3] inhomogeneities distortion decreases with the increase of the used gradient strength, for instance in a MR with 1,5 T with a gradient of 1,5 mT/m, the distortion is of 1mm, but if the gradient is 3 mT/m, the distortion will be half of the anterior. This cause of distortion occurs along the readout and slice selection direction, but not along the phase encoding direction, as phase encoding is not sensitive to any field inhomogeneities.

The nonlinearity in gradient fields causes distortion and the system that reconstructs the image

expects that the gradients have no deviation and are temporally stable. This distortion appears on the periphery of the Field of View (FOV), when it is larger than 35 cm [15]. Finally, the eddy currents artefacts are due to the fast switching of the gradient coils, which causes currents in the patients, cables and wires around the patient or in the magnet itself. These currents will appear as a signal drop in the margin of the image, and the distortion is reduced by optimizing the sequence of the gradient pulses [14].

According to Holland *et al.* [10], "increasing the main field strength or the time to acquire a frequency-encoded line will proportionally increase the distortion". These problems are present in SE and GRE EPI, but in the second two more problems occur. This is due to the well-known through-plane dropout in regions of susceptibility change and the in-plane dephasing. The fact that spatial distortions worsne with increasing field strength is corroborated by Cusack *et al* [17], who explain that with the increase of the static field, the susceptibility differences become larger and so the spatial distortions also increase.

The causes for the distortions provoked by the tissues are susceptibility difference and chemical shift. It is difficult to correct the spatial distortion caused by the tissue and a dedicated correction is needed, unlike the distortions caused by hardware that can be measured and characterized for an individual system [3].

The susceptibility difference has the same effect as the main magnet field inhomogeneities, because it produces a non-homogeneous magnetic field. This difference occurs in great changes of the magnetic susceptibilities. In most of the cases, this occurs in tissue-air interfaces, such as lungs or nasal cavities. Another way to produce this effect is when the tissue has some metal in its vicinity, which will also interfere with the magnetic field. The susceptibility difference will produce a quicker dephasing of spins (T_2^*) [15]. One way to prevent this distortion, when related to the presence of metal in the proximity, is to be careful with its presence every time that a MR exam is performed, due to its influence in the magnetic field

Independently of the cause of the spatial distortion, the sequence used in image acquisition influences the distortion, so all the distortions are sequence-dependent and can occur in all kinds of MRI techniques such as structural, functional, diffusion, etc.[3]. Faster sequences usually cause more spatial distortion; this is the case in EPI sequences that cause a pixel shift in the phase encoding direction [7, 10]. This is caused by the relatively long time between sampling points in that direction when compared to the frequency encoding direction [10]. This kind of sequence and spiral imaging pulse sequence cause spatial distortion due to the fast acquisition times and the magnetic field inhomogeneities [4].

3.2 Spatial Distortion and Phantoms

Some studies have been made to measure and correct spatial distortions with the help of phantoms. To measure spatial distortion are usually used phantoms that normally have a set of reference points, which can be 2D or 3D. The 2D phantoms can only measure distortions in two dimen-

sions, but they are simple to use and the spatial distortions are easily perceptible [3]. Nowadays, already exists a significant quantity of 3D phantoms, and Wang *et al.*[3, 18] proposed a new 3D phantom design (shown in figure 3.1a) that consists of grid sheet layers aligned in parallel with equal spacing along the z axis. The great advantage of this phantom is that it can incorporate as many control points as the user wants, just by decreasing the gap between the grids, and it is easy to understand and measure the spatial distortion.

Other similar phantom proposed by Mattila *et al.*[19] consists in a series of acrylic plates aligned in spherical holes that can be filled with the desired liquid (see figure 3.1b). This phantom was designed with dimensions that allow studying more effectively the images acquired with EPI sequences, because the reference structures are large enough to be sampled in the EPI voxel sizes, and small enough to not have a high structure density and cause overlap of signals from different structures. The second phantom is already designed for fMRI e DW-MRI images, but it cannot measure diffusion yet.

In the field of diffusion MRI, Perrin *et al.*[20] developed a phantom that permits studying the white matter fibre crossing. As shown in figure 3.1c, this phantom is constituted by 2 cross sets of fibres with dimensions similar to the axons that are parallel in each set, mimicking the human white matter fibres. These fibres are permeable, which is important to allow water molecules to exchange between both extra- and intra-compartments, simulating intra and extra molecular diffusion.

(a) Wang *et al.* phantom[3, 18]

(b) Mattila *et al.* phantom[19]

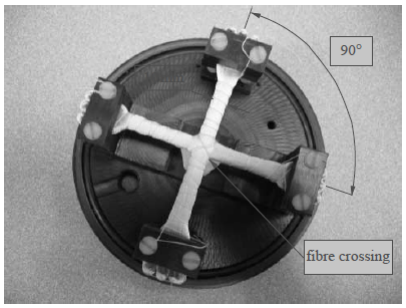

(c) Perrin *et al.* phantom[20]

Figure 3.1: Phantoms used in MRI to measure and correct spatial distortions

3.3 Spatial Distortion Correction

By 2005, spatial distortion correction in MRI was performed only in 2D, but it was expected that 3D methods become available soon [3]. To execute a distortion correction it is necessary to find the functions that transform the distorted image space into the undistorted space, these functions are called mapping functions [3]. These functions can be derived using 2D or 3D phantoms using the information about the distortion given by them, as explained in section 3.1

Several methods have been published to correct spatial distortions in diffusion weighted images, such as the use of gradient pre-pulse [5]; bipolar gradients [5]; twice-refocused SE [5]; calibration data [5]; acquisition of additional images with reversed diffusion gradients [5]; use RF refocusing, as in single shot spin-echo, multishot or steady state free precession pulse sequences in combination with parallel imaging [1] and retrospective correction methods [4, 5]. The advantage of the retrospective methods, such as Registration, is that they do not need a sequence modification or additional data acquisition.

Another way to correct spatial distortion is the use of shim coils [17] that also have the advantage of not needing any additional data acquisition or specific sequence, but a calibration before the image acquisition is necessary and according to the author this correction does not remove all spatial distortions in the MRI.

There are several approaches to correct MRI with a spatial distortion. In this thesis three methods will be studied: Registration, Field Map correction and a new proposed pipeline. The first two methods were chosen because they are the most implemented in the referenced literature for DW-MRI correction that uses EPI sequences. The pipeline consists in performing a Field Map correction after a registration was performed, and analysing the improvements regarding the other two methods.

3.3.1 Registration

Registration is a method that consists in aligning two images [6], namely *source image* to *reference image*. Regarding distortion correction, *source image* is the image with distortion and *reference image* is the image without distortion. This is not completely satisfying, though, as the reference image might also present distortion. The image without distortion is usually a MRI image, but it can also be a CT image. This technique can also be used for various other applications, such as comparison of two images from different medical imaging modalities, e.g. SPECT/PET and MR. Another example is the comparison of exam images of the same patient obtained at different time points, in order to understand if the patient's clinical situation remains unchanged or not, which can only be done on geometrically similar images. This method can also be used for functional and diffusion MRI, whenever necessary to align a series of images. A disadvantage of this technique is the necessity of a distortion-free MR or CT image. In the case of fMRI, registration is done on a single image of the series, which can present spatial distortion. Equally, for DW-MRI, registration is performed on an EPI image with a field strength coefficient (b-value) equal to zero, which

can also present spatial distortion. Thus, this method requires always an image without spatial distortion or the correction will not be totally efficient.

Registration techniques can be categorized as rigid or non-rigid, depending on the type of transformation existent between the two images. Rigid models are usually used for rigid motion correction, when it is merely necessary to determine rotation and translation [6]. However, if the deformation is non-linear, the model used must be non-rigid, because the rigid motion model will not produce an optimal alignment [6].

Registering two images consists in determining the geometric transformation that matches one image to the other. However, this problem has no easy solution. To better understand this issue, it can be divided into four components [21]: *transformation model*, *interpolator*, *similarity metric* and *optimizer*. These four components are applied to obtain transformation that approximates closely the *source image* (moving image) to the *reference image* (fixed imaged), as shown in the diagram of 3.2. An example of an "ideal" registration is presented in figure 3.3.

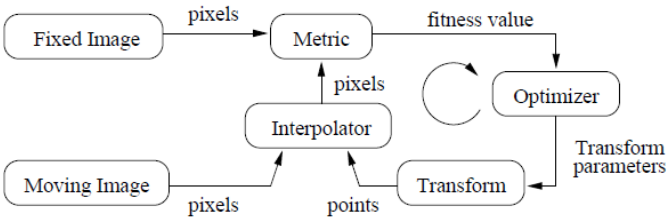

Figure 3.2: The basic components of the registration framework are two input images (fixed and moving images), a transform, a metric, an interpolator and an optimizer [21]

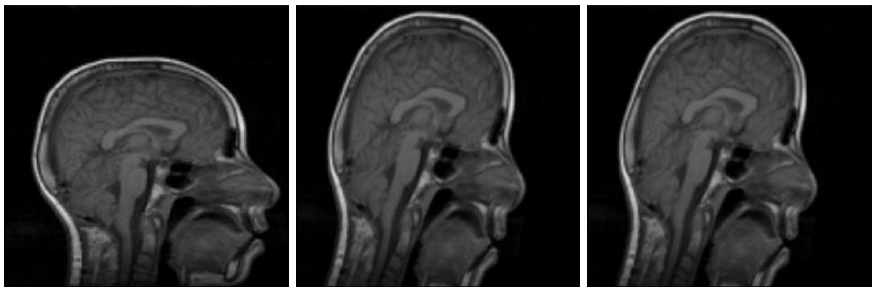

(a) Source **(b)** Target **(c)** Registration Result

Figure 3.3: Flowing from source to target: An "ideal" experiment [6]

Several studies have been developed in the field of MRI distortion correction by applying the method of Registration. Table 3.1 summarizes the set of methods studied with different registration components. It should be noted, that the Haselgrove *et al.* [22] study is also based on a method to register DW-MRI, where the second DW-MRI is registered to the first (b=0) and the transformation of the other DW-MRI is estimated based on the b-value.

Other studies were elaborated, but not in the field of Registration components. Mohammadi *et al.* [23] compares 2D and 3D registration to correct spatial distortion due to eddy-currents, concluding that a whole-brain registration will be more accurate than only a 2D registration. Daessle *et al.* [24]

in turn, developed a new optimization algorithm, NEWUOA (New Unconstrained Optimization Algorithm), applying it to some already existing registration methods; good results were obtained in terms of NEWUOA's accuracy and robustness in different registration cases.

Regarding optimization of registration speed performance, some studies have been made with multi-scale Registration, such as the Maes *et al.* study [25]. Multi-scale resolution begins the registration process with a lower resolution image (just part of the voxels are considered), converges the registration and then increases the resolution. This process is repeated to achieve the resolution of the original image. This process demonstrated to be computationally faster and the accuracy and precision of the registration continues to be good.

Table 3.1: Registration Methods Survey

Reference	Metric	Optimizer	Interpolator	Transform
Mangin[26]	MI with Parzen Window Correlation Ratio	Powell		Affine
Lau[27]	MI	Robbins-Munro GD	B-Spline	
Maes[28]	MI	Powell	Nearest Neighbour	Rigid Body
Rohde[29]	NMI	Gradient Ascent		
Netsch[30, 31]	MI Local Correlation	Least-Squares		Affine
Wu[32]	MI		B-Spline	Affine
Mistry[33]	MI	Lavenberg-Marquardt	Linear Cubic Fourier	Affine Fourier
Haselgrove[22]	Normalized Cross Correlation			Translation, Shearing and Scaling
Kim[34]	MI			SPM-based Affine
	Standard Deviation			AIR-based Affine
				AIR-based nonlinear transformation
Techavipoo[5]	NMI	Powell	Linear Partial Volume Estimated Histogram Shift Theorem Nearest Neighbour	Translation,Shearing and Scaling

MI = Mutual Information; GD = Gradient Descent; NMI = Normalized Mutual Information

3.3.2 Field Map Correction

According to Jezzard and Balaban [7], correcting spatial distortions in EPI with registration is difficult or impossible. The main cause of distortion in EPI is magnetic field inhomogeneities, which causea pixel shift in the phase-encoding direction and therefore, a spatial distortion. A possibel solution for this problem is to acquire a Field Map after the EPI.

A Field Map is a complex MRI that consists in acquiring two GRE images with different TE and subtracting the phase between them, obtaining an image that represents the field-inhomogeneity. This occurs because a phase image represents the signal given by equation (3.1) and the result of the phase subtraction is given by (3.2), where $\Delta\Phi(\vec{r})$ represents the field-inhomogeneities [10].

$$exp(-i\gamma\Delta B(\vec{j})TE \tag{3.1}$$

$$\Delta\Phi(\vec{r}) = exp(-\gamma\Delta B(\vec{j})\Delta TE \tag{3.2}$$

This way it is possible to find temporal field-inhomogeneity changes. This leads to the necessity of acquiring additional k-space data, which increases the acquisition time and, to avoid this, the field map usually is constrained by a low-pass filter or truncated from the total EPI k-space data [35].

Another way to acquire a field map is proposed in [7, 35, 36] and consists in collecting a pair of EPI images with opposing blipped phase encode gradient polarity that contain similar spatial distortion, but in opposite directions of the phase-encode direction. This method could induce some errors as it is necessary to change the acquisition sequence and this could induce some field-map changes, especially in regions with susceptibility induced field inhomogeneity [35]. Another disadvantage of this method is that the images need to be acquired twice, which will increase the scan time.

The field inhomogeneity map can be obtained according to the expression proposed by Jezzard and Balaban [7]:

$$\Delta B(x, y, z) = \frac{\Delta\Phi(x, y, z)}{2\pi\gamma\Delta T_E} \tag{3.3}$$

where $\Delta\Phi$ represents the difference phase map of the two structural images, γ is the gyrometric ratio for hydrogen and ΔTE is the difference between echo times. The authors also established that a smooth operation before the phase map calculation is beneficial, so as to prevent abrupt transitions between distinct images regions. Whit this method it is possible to correct spatial distortion in the phase-encoding directions.

Gallichan *et al.* [36] propose a sequence that can be useful to acquire the Field Map on *in vivo* MRI exams. This sequence (see figure 3.4) consists of an additional spin-echo with reversed phase-encoding direction instead of the standard spin-echo used in DTI, which has the advantage of minimizing the scan time, comparatively with a double acquisition. This sequence can be improved with the use of parallel acceleration that reduces the TE and increases the SNR.

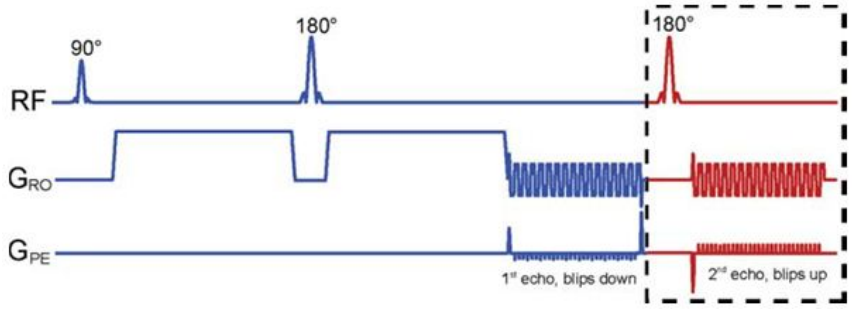

Figure 3.4: Proposed pulse-sequence diagram for dual-echo blip-reversed diffusion-weighted EPI [36]

Chapter 4

Methodology

As established in previous chapters, spatial distortion is an MRI issue that must be corrected for better visualization medical images. This project proposes study and comparison of several methods to correct this distortion: Registration, Field Map correction and a new proposed pipeline, which consists in performing a Field Map correction after a registration process. As a result, we expect to obtain comparisons between the three proposed methods for DW-MRI data with different field strength coefficients (b-values) and to assess how this coefficient influences accuracy and performance of these methods. As a conclusion of this project, we expect to establish the best correction method for DW-MRI for a given b-value.

Registration and Field Map correction are methods already described in literature. However, the combination of methods has not been studied yet. This pipeline combines advantages of two correction methods: Registration alignment and resampling, and specific correction of field inhomogeneities for Field Map correction. Another reason for choosing these methods was the implementation simplicity, when compared with other methods in literature. An advantage of these methods is that they are already totally or partially implemented. In the case of the Registration, the ITK[37] library in C++ has an extensive set of components and FSL [38, 39] has some registration components implemented, as well. FSL has the Field Map correction method already implemented, which will simplify the implementation part of the project.

For assessment of registration correction results, simulation of MRI data was required, in order to obtain images with distortion and their corresponding images without distortion. Simulated data was used to optimize registration parameters, in order to achieve optimal parameters for all combinations tested.

Registration combinations with new optimized parameters were tested and evaluated, by applying the metrics described in this chapter. Also, the same combinations of Registration were performed and evaluated for b=0 real data, to validate the simulated data correction. The best combinations were then used with real data. For that purpose, real DW-MRI data is acquired with different b-values and used to assess the three methods proposed, namely: Registration, Field Map correction and the new proposed pipeline and the correction accuracy in images with increasing b-values that

correspond to a decrease in SNR. We chose this type of image due to its great need for correction and the existing general need for a comparative study of these methods using this type of images, as it is poorly represented in reviewed literature.

The flowchart in figure 4.1 explains the procedure that was applied in this project.

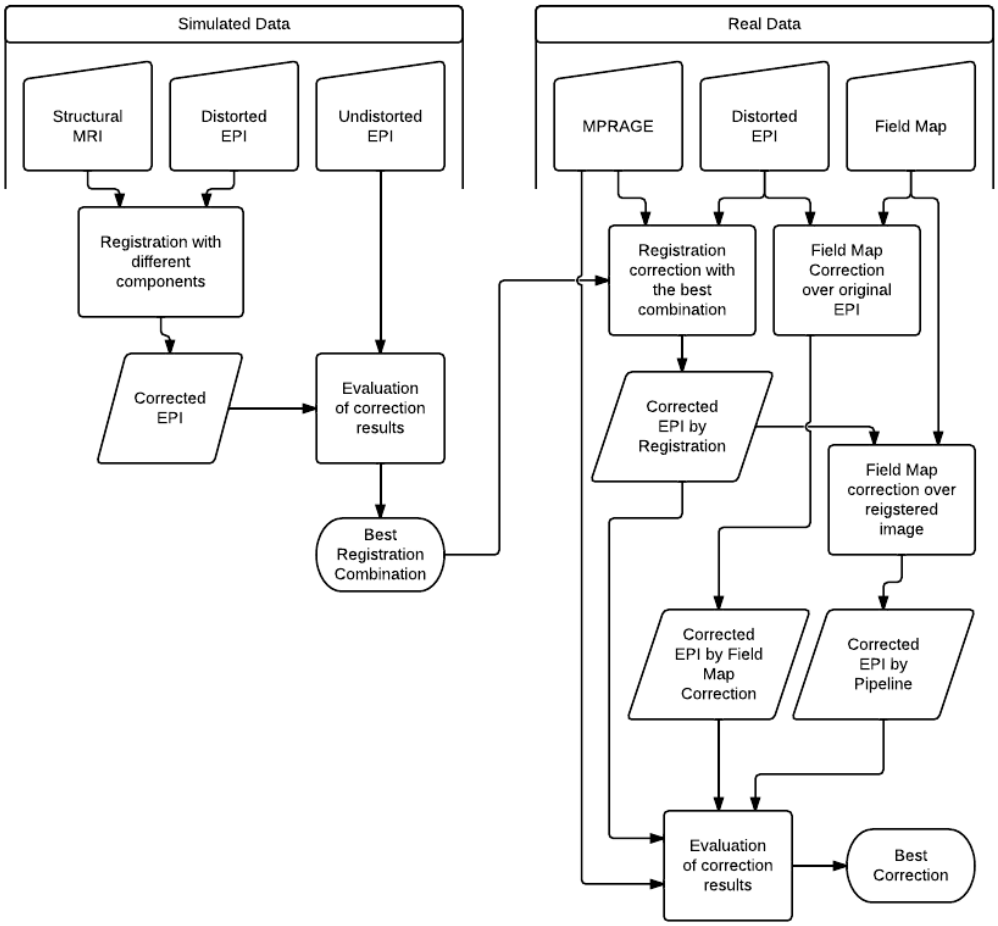

Figure 4.1: Correction process flowchart

4.1 Simulated Data

This part of the project ensures the evaluation of registration correction accuracy, as it is possible to simulate EPI data with and without distortion and structural images.

The simulation process of EPI data was performed using a FMRIB Software Library (FSL) tool [38, 39] called POSSUM [40, 41], described in appendix C.6. EPI data with (figure 4.2a) and without (figure 4.2b) distortion was simulated applying $TE = 3ms$, $TRSlice = 3s$, $TR = 150s$, a matrix size of 64x64x50 and a resolution of 3x3x3 mm^3, according to the usual values used in real acquisitions. Both images are based on an object given by FSL, although a B_0 inhomogeneity field was applied to the distorted EPI, also given by FSL, which is calculated based on the object previously used to simulate the EPI.

Also, a structural image was necessary to perform registration. For that, POSSUM [40, 41] was used again to generate a GRE with $TE = 35.7ms$, $TRSlice = 150ms$, $TR = 685,44s$, a resolution of 3x3x3 mm^3 and a size of 64x64x50 (figure 4.2c).

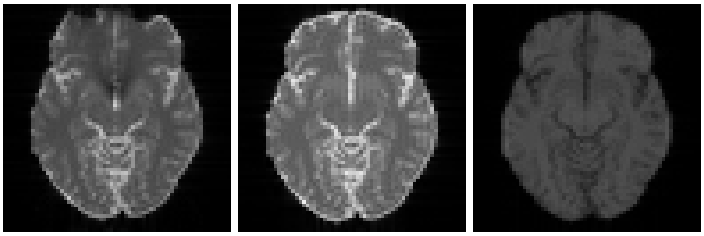

(a) Distorted EPI **(b)** Non-distorted EPI**(c)** Gradient-Eco MRI

Figure 4.2: Simulated MRI data

Regarding simulated data, it is important to say that they could have associated errors; this means that they do not completely represent the real data. In the case of POSSUM, Drobnjak and Jenkinson studied the influence of the voxel size in the error of the image [40], as shown in figure 4.3, where it is demonstrated that with increasing voxel size, the associated error also increase. With the voxel size used in this project (3x3x3 mm^3) the associated error between analytical and simulated data is of 3%. It is also important to state that this analysis is not a comparison between real and simulated data. However, it is closer, so it is important to validate simulated data. Another analysis performed by Drobnjak and Jenkinson *et al.* [40] was the time of simulation, related to the voxel size. However, this analysis was performed for normal simulations and this project used simulation with a B_0 field that increases the simulation time.

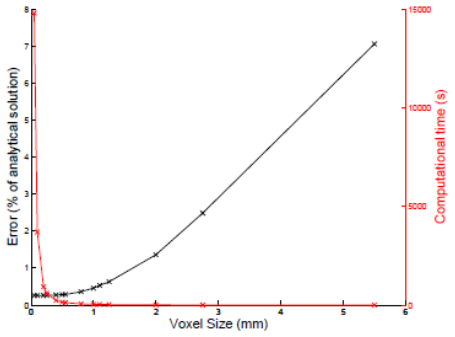

Figure 4.3: Relation between error and time of execution for the voxel size of a simulated MRI with POSSUM. The black line and black *y*-axis show the RMS based difference between the analytically calculated *k*-space and simulated *k*-spaces expressed as a percentage of the analytically calculated *k*-space signal. The red line and the red *y*-axis show the computational time which it took for the generation of the simulations [40]

4.2 Data Acquisition

Real data was obtained with a 3T Siemens MAGNETOM TRIO Tim system at IBILI. A distorted set of DW-MRI with *b*-values of 0, 1000, 4000 and 8000 was obtained. Acquisition parameters are described in table 4.1.

We acquired a structural MPRAGE image to correct the EPI distorted by Registration methods and a gradient echo field map image to correct with the Field Map method. This field map image was acquired with a ΔTE of $7.38ms$. Acquisition parameters of both images are also presented in table 4.1.

Table 4.1: Acquisition parameters of MRI data

	b-value	TR(ms)	TE(ms)	FA($\circ$)	TI(ms)	FOV(mm^3)	Resol.(mm^3)	Matrix Size
EPI	0	11300	121	90	-	256x256x120	2x2x2	128x128x60
	1000	11300	121					
	4000	12600	142					
	8000	14700	178					
MPRAGE	-	2980	2300	9	900	256x256x160	1x1x1	256x256x256
Field Map	-	423	-	60	-	256x256x120	4x4x3	64x64x40

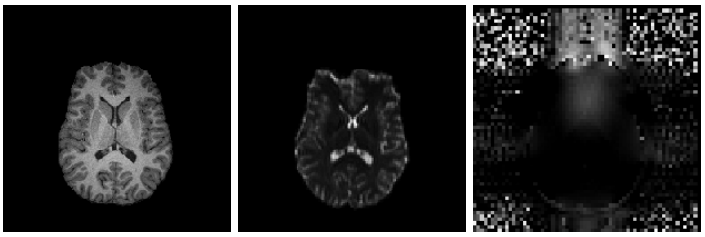

(a) MPRAGE **(b)** EPI - *b*=0 **(c)** Field Map

Figure 4.4: Real MRI data

4.3 Registration

As already explained in section 3.3.1, Registration consists in finding the best transformation that matches the source image to the reference image. This can be translated by equation (4.1) where A is the reference image, B the source image transformed by $T()$, $M()$ the similarity metric and $arg()$ represents the transformation argument of T [42].

$$arg\max M(A, T(B)) \tag{4.1}$$

In this section, several components (transformations, interpolators, metrics and optimizers) used in various registration techniques will be explained. All the components used are already implemented in ITK [37], and the following explanation is based on software features that are explicit in the ITK guide [21].

4.3.1 Transformations

Registration's transformation component is the function which changes the source image into an image that will be similar to the reference image. Transformation parameters are optimized by the iterative process until an image is obtained, where the metric value is at its maximum.

Transformations have several variables and an increasing number of variables will also increase the transformation's Degrees of Freedom (DOF), and therefore, a more reliable result will be obtained. On the other hand, a great quantity of variables will increase the processing time as well; therefore, a compromise between efficacy and performance is required.

Affine and B-Spline are the transformations used in this project. Affine is not considered to be a non-rigid transformation, but B-Spline is. These transformations are slower than others, due to the vast number of parameters. However, Affine transformation has fewer parameters than B-Spline, and thus it is faster than the second.

Affine

Affine transformation represents a linear transformation and can be performed in any space dimension. This can be interpreted as translation, rotation, anisotropic scaling and shearing. It is possible to represent this transformation with equation (4.2) that shows the three-dimensional problem. i' are the coordinates of the transformed image and i those of the original one, where $i = \{x, y, z\}$. M_{ab} are the matrix values that represent rotation, scaling and shearing transformations, and T_i represents translation. This transformation also gives the opportunity to determine the transformation centre by setting C_i to a value other than 0 and this feature was used to centre the transformation in the image space.

$$\begin{bmatrix} x' \\ y' \\ z' \end{bmatrix} = \begin{bmatrix} M_{00} & M_{01} & M_{02} \\ M_{10} & M_{11} & M_{12} \\ M_{10} & M_{11} & M_{12} \end{bmatrix} \cdot \begin{bmatrix} x - C_x \\ y - C_y \\ z - C_z \end{bmatrix} + \begin{bmatrix} T_x + C_x \\ T_x + C_y \\ T_z + C_z \end{bmatrix} \tag{4.2}$$

Another parameter used with Affine is the initial transformation, set to 0 for all values of equation (4.2), except C_i. Initialization is an important parameter for cases that present great differences between source and reference image. That is not the case, as the images are from the same subject, acquired with the same scanner and on the same day, therefore, they do not present great differences. Another factor that could induce big differences is movement during acquisitions, which in this study was considered null.

Scaling transformation parameters is an optimizer parameter related to transformations. In the case of Affine , it is possible and advisable according to the software guide [21], to set scales between translation and other parameters. Scaling is important due to differences in units and a scale of 1/1000 was chosen for translation parameters, as proposed by the software guide [21]. According to this scale, 1 voxel translation corresponds to 0.001 degree of rotation.

B-Spline

B-Spline is a heavier and more powerful transformation as it applies a deformation field to every sampled image point.

In this transformation the main parameter to determine is the Spline order that can be set from 1 to 5. An increase in Spline order increases the transformation accuracy, allowing more abrupt changes between voxels. However, this increment slows processing down.

Parameters regarding the B-Spline spacing grid were also set: Origin, Region and Direction. These were set according to reference and input images.

4.3.2 Interpolators

Interpolators are required for the registration process, because when a transformation is applied to the source image, the result is usually not in the same grid as the reference image. As shown in figure 4.5, the blue grid of the reference image and the black grid of the source image do not overlap.

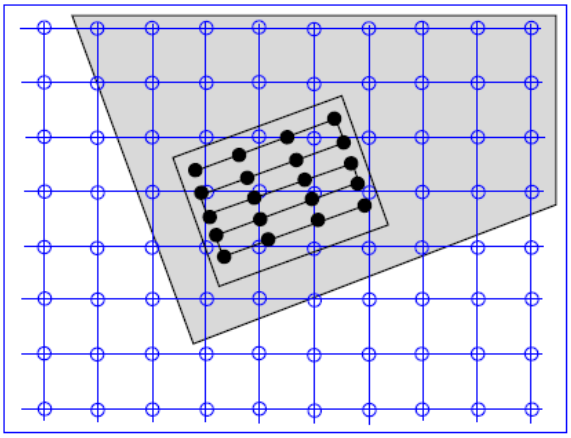

Figure 4.5: Grid positions of reference image map compared to non-grid positions of source image

In this project, three different interpolators are used: Linear, B-Spline and Nearest Neighbour, which will be explained below.

Linear

Linear interpolation assumes that pixel/voxel values vary linearly in the grid, and therefore, gradients are calculated. However, the gradient is not continuous for these grid positions. Depending on whether the object has 1, 2 or 3 dimensions, this type of interpolation is called linear, bilinear or trilinear, respectively. As all registrations are done with 3 dimensions, trilinear interpolation was used.

B-Spline

This interpolation method is heavier than linear and other polynomial interpolations, but on the other hand, it can produce better results for big orders. This is due to the fact that polynomial interpolators analyze the whole set of points, while B-Spline analyzes each grid point in time, and

therefore obtains a Spline curve. After that, all Splines are summed up, producing interpolation of the entire image.

Nearest Neighbour

This interpolation is simpler than the others explained before and requires less computation. It consists in assigning the intensity value of the nearest grid point to the point in study.

4.3.3 Metrics

The registration's similarity metric is the function that compares the transformed source image to the reference image. There are a series of metrics available in the ITK library [37], but in this project, only the Mutual Information (MI) was used. We chose this metric because of its advantage to register two images from different intensity weights, such as MPRAGE and EPI, which are used in this project, as pixel values are not compared directly.

Mutual Information

According to Pluim *et al.* [43], the literature presents three ways to apply MI. Following, we will explain how they are implemented in ITK [37].

The MI principle provides the quantity of uncertainty of one voxel in one image in relation with the other image (entropy). Therefore, it begins with the Shannon definition of entropy ($H(A)$) and joint entropy ($H(A, B)$) [44], given by equations (4.3) and (4.4).

$$H(A) = -\sum_{a} p_A(a) \log p_A(a) \tag{4.3}$$

$$H(A, B) = -\sum_{a,b} p_{AB}(a, b) \log p_{AB}(a, b) \tag{4.4}$$

Where $p_A(a)$ is the probability of intensity a in image A and $p_{AB}(a, b)$ is the prabably of intensities a and b occurs at the same voxels of images A and B.

When the two images are totally independent from each other $p_{AB}(a, b) = p_A(a)p_B(b)$, the joint entropy is obtained as in equation (4.5).

$$H(A, B) = H(A) + H(B) \tag{4.5}$$

MI value ($I(A, B)$) is given by the difference between the joint entropy, in case of independent images, and the real joint entropy from the two images, as demonstrated by equation (4.6).

$$I(A, B) = H(A) + H(B) - H(A, B) \tag{4.6}$$

The uncertainty that image A has relatively to image B decreases as the MI value increases; therefore, both images are closer to each other as the MI value becomes greater. The minimum value for this metric is 0 because in the worst case, the images are totally independent and the difference becomes 0.

ITK [37] includes some variants of MI. This project applies the metric proposed by Mattes *et al.* [45], which presents a variation that considers just a sample of points from two user-definable images, which increases the speed of similarity evaluation. This value cannot be too big, so it does not slow down registration, and it cannot be too small, so it does not impede the metric evaluation between two images in favourable conditions. The number of histogram bins also needs to be chosen because entropies and joint entropy are calculated from the intensity probabilities that are the values of the histogram. Using a great number of bins will increase the execution time, due to the increasing number of calculations. However, a small number of bins will decrease the accuracy of the metric, due to the low discrimination given by the few bins, thus less information. Another alteration in the Mattes MI comparatively to the original metric is that the two images are normalized to one.

4.3.4 Optimizers

In the registration process, optimizers are the component that analyzes the metric value and intends to achieve the minimum or maximum value (in case of MI the maximum is desired), considering the transformation function's several variables. This process is not always a simple one, because some local extremes can be reached during registration iteration, and consequently optimal registration is not achieved. For this project, two optimizers were chosen: Gradient Descent (GD) and Powell. Both optimizers minimize the metric, but ITK [37] allows changing a minimization problem into a maximization problem, by only considering the metric value's negative. Another important error that could occur during the implementation is interpolation errors that change the source image [43].

Gradient Descent

This optimizer consists in applying a gradient to each transformation variable p_n, as shown in equation (4.7). The gradient is the corresponding variable's derivative and the $learning\ rate$ is set by the user, scaling the optimization variations per iteration. One important characteristic of the $learning\ rate$ is that it must be adjusted for the transformation in cause, depending on the range and number of transformation parameters [29].

$$p_{n+1} = p_n + learning\ rate \cdot \frac{\partial f(p_n)}{\partial p_n} \tag{4.7}$$

This process has the disadvantage of not doing a convergence analysis, thus, optimization only finishes when the number of user-defined iterations is reached.

Powell

Compared to GD, the Powell optimizer has the great advantage of calculating the metric's minimum in a finite number of iterations, as it uses no derivatives. On the other hand, this is a heavy optimizer, due to the great quantity of calculations performed for each iteration.

This optimizer obtains the minimum for the metric function f in every n linearly independent direction ξ_r (transformation parameters), starting with the best known value of the metric function at point p_0 (initial function parameters). For that, a series of procedures is performed, changing the function parameters (p_r) along the iterations, as described below [46].

1. Calculation of a λ_r for $r = 1, 2, ..., n$ granting that $f(p_{r-1} + \lambda_r \xi_r)$ is at minimum
2. Define $p_r = p_{r-1} + \lambda_r \xi_r$
3. For $r = 1, 2, ..., n-1$ replace ξ_i by ξ_{r+1}
4. Replace ξ_n by $p_n - p_0$
5. Choose λ so that $f(p_n + \lambda \{p_n - p_0\})$ is at minimum
6. Replace p_0 by $p_0 + \lambda \{p_n - p_0\}$

For this optimizer it is necessary to set the tolerance value to stop optimization process and step length.

4.4 Field Map Correction

To execute this method, three images are necessary: a distorted EPI, a field map calculated from two phase images acquired with different TE and a magnitude image from the field map. The correction process can be described by the flowchart in figure 4.6.

Firstly, a brain extraction was performed on magnitude image and EPI data, in order to obtain only brain images. For that, BET [47, 48] tool was used (see appendix C.1).

After that, it had to be ensured that both magnitude image and field map present the same resolution. In this case, `fslinfo` was used (see appendix C.8.1) to see the image's resolution information. In cases where the resolution of both images was not identical, we executed a resampling of the structural MPRAGE (normally the image with highest resolution) for the field map image, with a script written in *C++* using the library ITK [37].

Field map was provided by the scanner as the difference between phase images. To begin with, a rescaling to $[-\pi, \pi]$ had to be performed, using `fslmaths` (see appendix C.8.5). Field map data

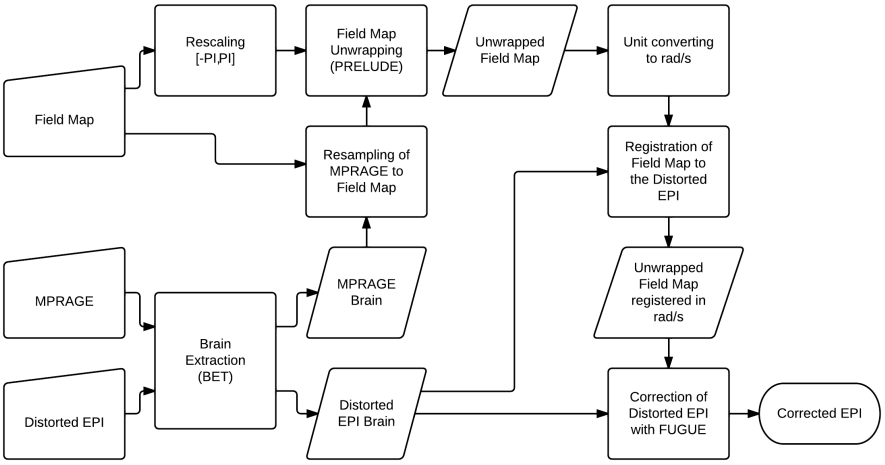

Figure 4.6: Flowchart used to correct image using Field Map process

needed to be unwrapped, which consists in fitting a surface to the phase map, in order to obtain a smoother map without 2π jumps, which are normal in wrapped phase images [49]. For this, PRELUDE (see appendix C.3) was used.

Data was now presented in radian units, but for correction purposes, radian per second (rad/s) was required. So, the unwrapped field map was divided by the difference of TE from the phase images, using `fslmaths` (see appendix C.8.5).

The result was a field map correctly unwrapped and presenting the desired unit. However, before performing the correction, it was necessary to resample the Field Map in the EPI space, which was executed with the same *C++* script used for MPRAGE. In order to perform the correction, FUGUE tool (see appendix C.4) was applied. This tool produced the shift estimation in one direction, represented by the field map, and readjusted the voxels' positions, therefore correcting the image. For this, $-y$ was set as unwrapping direction, which is the phase encoding acquisition and represents the direction where distortion occurs. Dwell time was also necessary, which is the effective echo spacing and can be calculated according to equation (4.8).

$$Dwell\ Time = \frac{1}{Bandwidth * Number\ of\ Phase\ Lines} \tag{4.8}$$

Finally, this resulted in the corrected EPI. All these processing steps are also described in appendix C.5, with different proceedings for different field map acquisitions.

4.5 Evaluation

After image correction, it is necessary to assess the correction qualitatively and quantitatively, in order to achieve the best correction method. For that, different methods were used, according to the image type. For simulated MRI, Root Mean Square (RMS) and Dice Coefficient of segmented images were used as evaluation method. For both, simulated and real data, we used other

three metrics: Normalized Mutual Information (NMI), Squared Correlation Coefficient (SCC) and Euclidean Distance of Centres of Mass (CM). Simulated data was evaluated regarding corrected images and distortion-free images. As it is not possible to have real non-distorted EPI data, a structural image was used as reference, and therefore, metrics were calculated between corrected images and MPRAGE volume. In both cases, a control case was calculated between original distorted data and reference images. It was expected that the correction evaluation improves when compared to the original control EPI.

It is important to say that the analysis is highly influenced by the image noise as said by De Wilde *et al.* [50]. Their study shows that a decrease of MRI noise, increases some assessment measures. So, image noise will influence the evaluation of the described metrics, and we must be careful with these results, especially for higher *b*-values, where the SNR is lower.

To perform the evaluation, it is necessary that both images have the same size; consequently, the MPRAGE and the correction results were resampled to correspond to the size of the original distorted EPI using the same script as for Field Map correction resampling. All the performed metrics were calculated in MATLAB® [51].

To choose the best registration combination of simulated data, each metric was ranked. The ranks obtained for each registration were summed up and those with the lowest sum were picked. From these, the combinations with lowest correction time were chosen to apply on real data.

For both simulated and real data, a qualitative analysis was performed, in order to evaluate the complete correction of each method.

4.5.1 Root Mean Square (RMS)

RMS measures the mean difference of all voxels of both images. In this measurement, the ideal values are the smallest ones, indicating fewer differences, which is what we expected from the correction.

This metric consists in applying equation (4.9) on two different images.

$$RMS = \sqrt{\frac{\sum_i^n (v_{ref}(i) - v_{eval}(i))^2}{n}} \tag{4.9}$$

where n is the total number of voxels, i is the current voxel position, v_{eval} is the image that is being evaluated (corrected image) and v_{ref} is the reference image that corresponds to a image without distortion. To allow the comparison of RMS values, an extra calculation was executed between the distorted and non-distorted EPI, which should produce the maximum RMS value.

4.5.2 Dice Coefficient of Segmented Images

The Dice Coefficient [52–54] evaluates the similarity of two samples. In the case of segmented images, the likeness of one tissue in both images is measured. The value obtained increases with

the samples' similarity, which is supposed to happen with the correction.

Segmentation of images was performed with FAST [55] (see appendix C.7). All images were segmented in 3 tissues, namely White Matter (WM), Gray Matter (GM) and Cerebrospinal Fluid (CSF).

The Dice coefficient [52–54] was calculated for WM, GM and CSF, according to equation (4.10).

$$Dice(S_1, S_2) = \frac{2\,|S_1 \cap S_2|}{|S_1| + |S_2|} \tag{4.10}$$

where S_1 and S_2 are the two samples, respectively, the corrected or distorted sample and the distortion-free EPI structural image of simulated data. The segmented EPI without distortion is used as the *Golden Standard* to evaluate correction performance, as this type of image has no distortions.

4.5.3 Normalized Mutual Information (NMI)

As explained before in section 4.3.3, MI is a comparison metric used by some authors to evaluate correction results [5, 17, 56], and there are several methods for calculating MI. In this assessment, NMI [57] are given by equation (4.11).

$$NMI(A, B) = \frac{H(A) + H(B)}{H(A, B)} \tag{4.11}$$

where $H(A)$ and $H(B)$ are entropy of images A and B given by equation (4.3) and $H(A, B)$ is the joint entropy of the same images given by equation (4.4). This way of calculating MI allows having a maximum value for the metric, which is the double of the number of histogram bins considered; this number was set to 50. Finally, the value obtained is divided by 100 (the double of 50) to obtain a value normalized to 1.

This method of calculating MI has a maximum value of 1, when one image has the same intensity distribution as the other. This value decreases, when both images differ.

This metric was calculated between the corrected image and the undistorted image, and the structural image is used for real data and the distortion-free EPI for simulated data.

4.5.4 Squared Correlation Coefficient (SCC)

This evaluation method is a metric that assesses the relationship between two variables, in this case two images. The equation (4.12) was used to calculate the correlation coefficient r [58, 59]. This equation was proposed by Pearson in 1985 and this coefficient is also known as Pearson product-moment correlation [58].

$$r = \frac{\sum (x_i - \overline{x})(y_i - \overline{y})}{\sqrt{\sum (x_i - \overline{x})^2 \sum (y_i - \overline{y})^2}} \tag{4.12}$$

where x and y are the two images' voxel intensities and $\overline{x}$ and $\overline{y}$ the respective mean values. The coefficient r varies between -1 and 1, the extreme value means inverse and direct relationship and 0 refers to no relationship between both images. The signal of r is not important for this evaluation, as the importance lies in the similarity between both images, so the coefficient r^2 was calculated, which has the range $[0, 1]$, where zero means no similarity and 1 means that both images are the same or the inverse of each other. It is expected that this metric value increases with corrections.

4.5.5 Euclidean Distance of Centres of Mass

This measurement indicates the spatial difference between two images. So, the distance will decrease with correction, as the two images are closer to each other.

The CM was calculated for each correction and compared to the CM of the distortion-free image. This measurement was executed using equations (4.13), (4.14) and (4.15) for each coordinate x, y and z.

$$CM_x = \frac{\sum I_x \cdot x}{Area_I} \tag{4.13}$$

$$CM_y = \frac{\sum I_y \cdot y}{Area_I} \tag{4.14}$$

$$CM_z = \frac{\sum I_z \cdot z}{Area_I} \tag{4.15}$$

where I_j represents the voxel intensities of the coordinate $j = x, y, z$ in question and $Area_I$ is the image area .

To assess the difference between the corrected images and the distortion-free images CM, the Euclidean Distance (equation (4.16)) between the respective CM's was calculated.

$$d(A, B) = \sqrt{(A_x - B_x)^2 + (A_y - B_y)^2 + (A_z - B_z)^2} \tag{4.16}$$

where A and B are the respective CM's and A_i and B_i their coordinates.

4.6 Experiments

This project applied correction algorithms based on both of the above explained methods (Registration and Field Map Correction) and the proposed Pipeline.

The registration-based correction was performed using simulated data with different components, in order to analyze their performance. Table 4.2 presents the different conjugations of components

used in this method. These conjugations were chosen based on review literature (see table 3.1).

Table 4.2: Components used in Registration

ID	Metric	Optimizer	Interpolator	Transformation
Reg1	MI	GD	Linear	Affine
Reg2				B-Spline
Reg3			B-Spline	Affine
Reg4				B-Spline
Reg5			Nearest Neighbour	Affine
Reg6				B-Spline
Reg7		Powell	Linear	Affine
Reg8				B-Spline
Reg9			B-Spline	Affine
Reg10				B-Spline
Reg11			Nearest Neighbour	Affine
Reg12				B-Spline

Before choosing the method for real data correction, an optimization of the registration parameters was performed. The parameters that were optimized are listed in table 4.3, according to the respective component and the initially tested value.

Table 4.3: Optimization Parameters

Component	Parameter	Initial	Values Tested						
MI	Histogram Bins	50	25		50		75		100
	Samples (%)	45000 (≈20)	10240 (5)	20480 (10)	40960 (20)	61940 (30)	81920 (40)	102400 (50)	
GD	Learning Rate	0.001 10	0.000001	0.00001	0.001	0.1	1	- 10	- 100
	Iterations	750	500		750		1000		1500
Powell Opt.	Step Length	0.001		0.00001	0.0001	0.001	0.01	0.1	
	Tolerance	0.000001		0.0000001	0.000001	0.00001	0.0001	0.001	
	Max. Iterations	750							
B-Spline Transf.	Spline Order	3		2		3		5	

The optimization process was initialized for the above described values. In case of the learning rate for GD optimizer, a value was chosen for each transformation, Affine and B-Spline, due to the huge difference in parameter numbers of each transformation [29].

All optimizations were performed with all parameters set to the initial value, only changing the value being studied. It is also important to say that each optimization was only performed for the best couple of combinations for the parameter in question, according to the evaluation measurements previously done. It was considered that the remaining combinations would present the same behaviour with simulated data for the same parameter variations. The optimization was done based on the evaluation of the metric values.

After executing registration corrections and optimizations, it was important to measure the quality of corrections in simulated data, using the explained metrics. To evaluate the best registration combinations among those with lower sum of calculated ranks, we evaluated the correction time of the process with a function of *C++* that permits measuring the number of the CPU's clock ticks. The registrations with lowest execution time are the best ones.

To validate the simulated data, the same combinations were applied that were used for simulated data, and the results were analyzed using the metrics explained above. For validation it was neces-

sary to perform a mean of ranks, because a different number of metrics was analyzed for real and simulated data. Finally, the two best registration combinations were chosen for real data, i.e. by choosing the lowest mean of evaluation metrics ranks and the lowest execution times.

The above proposed pipeline and the two simple correction methods (Registrations and Field Map Correction) were applied on several real DW-MRI data with different *b*-values, in order to achieve the best correction method for different DW-MRI data. To assess the pipeline's improvements over the other correction methods, the above explained metric values were calculated.

Chapter 5

Results

This chapter will present the results of this project and a brief explanation about them. Firstly it will show the results of simulated data and the optimization of registration parameters. After that, these results will be validated with real data, where they will be compared real and simulated data. Finally, we will present the real data results, the analysis performed for the several methods and the influence of *b*-value in the correction.

5.1 Simulated Data

In this part of the project the obtained results will be presented regarding the registration correction in simulated data, as well as, all the results on optimization and evaluation of the same data. All results in this part can be seen with more detail in appendix A.

5.1.1 Preliminary Results

Initially, the 12 combinations in table 4.2 were performed with the parameters set to the initial values of table 4.3. Consequently, we obtained the results in figure 5.1. Observing the results and comparing them with the original data (see figure 4.2), it is possible to see which combinations makes the simulated data more similar to the reference image (GRE from POSSUM [40, 41]). However, none of the combinations completely correct the images. The existent distortion in the anterior part of the brain continues to exist, contrary to distortion-free EPI, as shown by the red arrows in figure 5.2.

After that, the results of the proposed metrics were evaluated, which can be seen in table A.1 of appendix A.1. In the same table is the ranking of the metrics and the method's execution time in clock ticks of the computer. Calculating the sum of ranks of all metrics, we obtained the graphic in figure 5.3, where it is possible to see that Reg11 and Reg6 have obtained the lowest results in the sum of ranks, which indicates a better performance. In terms of execution time, Reg11 obtained the best results (13905 ticks).

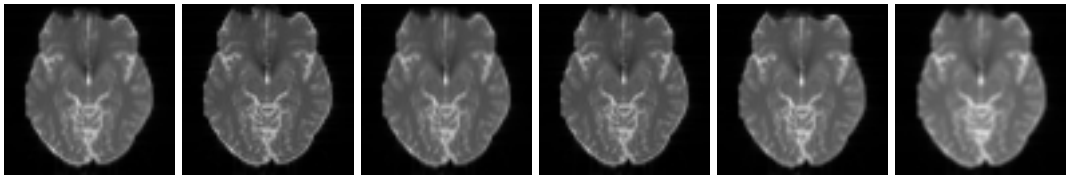

(a) Reg1 **(b)** Reg2 **(c)** Reg3 **(d)** Reg4 **(e)** Reg5 **(f)** Reg6

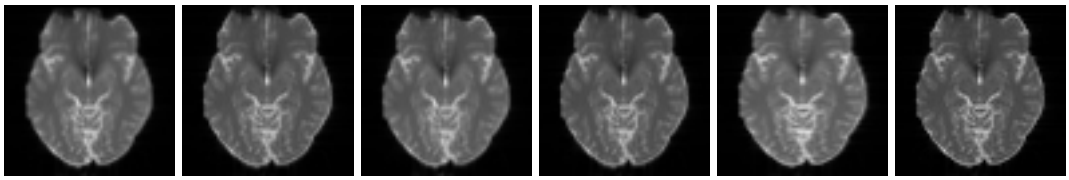

(g) Reg7 **(h)** Reg8 **(i)** Reg9 **(j)** Reg10 **(k)** Reg11 **(l)** Reg12

Figure 5.1: Preliminary results from registration correction methods using simulated data

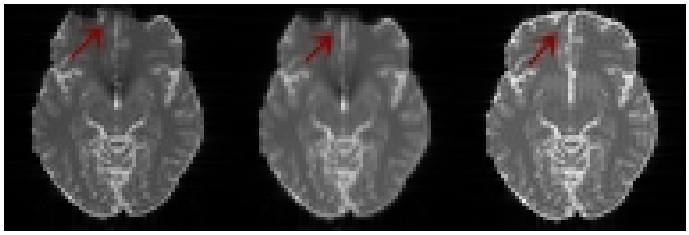

(a) EPI with distortion **(b)** Reg1 **(c)** EPI without distortion

Figure 5.2: Distortion correction results of simulated data. Red arrows indicate the spot of major distortions in the anterior part of the brain

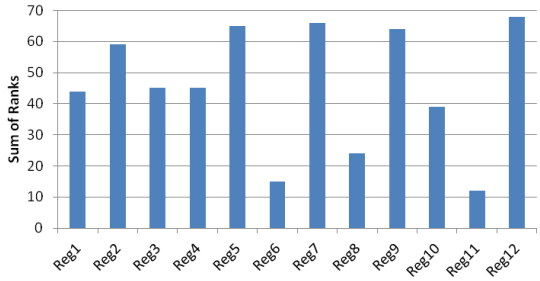

Figure 5.3: Sum of ranks of preliminary results for registration methods with simulated data

5.1.2 Optimization

To allow a correct used of registration components, it was necessary to optimize the registration parameters. Following, we will show the results of the optimizations indicated in table 4.3. The initial and final values of the tested parameters are shown in table 5.1.

Number of Bins in MI

For this optimization Reg6 and Reg11 were used, which obtained the best results in preliminary analysis. Observing the sum of ranks in figure 5.4, it is possible to see that Reg11 does not have

Table 5.1: Optimization Parameters

Component	Parameter	Initial	Result
MI	Histogram Bins	50	50
	Samples (%)	45000 ($\approx$ 20)	20480 (10)
GD	Learning Rate	0.001 10	0.00001 10
	Iterations	750	500
Powell Opt.	Step Length	0.001	0.001
	Tolerance	0.000001	0.00001
	Max. Iterations	750	500
B-Spline Transf.	Spline Order	3	3

variations. For Reg6 the best ranking value was 50 bins. Although the best results for both cases were not the same, the result of 50 bins was chosen for this optimization, due to the non-variation of metrics in Reg11.

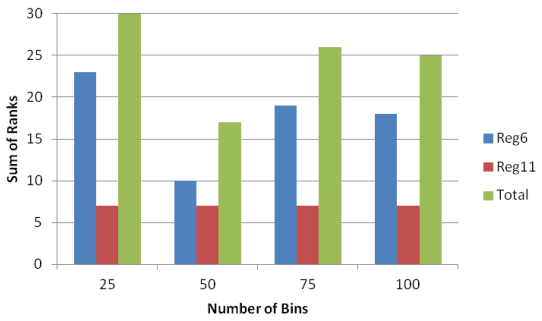

Figure 5.4: Optimization ranks of Number of Bins in MI

Number of Samples in MI

Analogously to the previous optimization Reg6 and Reg11 were used for the same reasons. Analyzing figure 5.5, it is possible to see that the number of samples does not influence the Reg11 results, since the results are the same for every parameter values tested. In the case of Reg6 the best result was achieved with 40% of sampled voxels. However, it is possible to see that above 10%, the differences between the metric values are inferior to 1%, in most cases. The execution time of the process rises in a larger scale with the increasing number of samples, so the value of 10% (Reg6 - 507952 ticks; Reg11 - 6371 ticks) was chosen, which was the second best result according to the ranking of metrics, and does not have a long execution time, as seen by the value for 40% (Reg6 - 1527140 ticks; Reg11 - 30836 ticks).

Learning Rate in GD Optimizer

For this parameter Reg1 and Reg6 were used because they were the best in preliminary analysis that used GD as optimizer and each one has a different transformation that could influence this parameter. This is due to the fact that the number and scale of the parameters influence the derivative

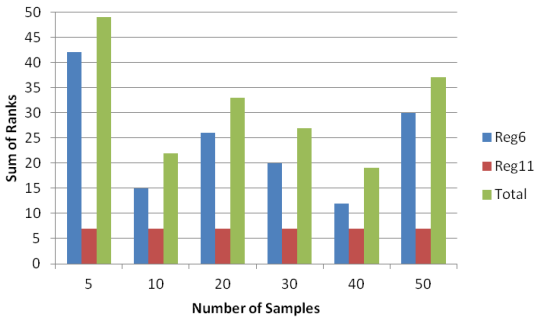

Figure 5.5: Optimization ranks of Number of Samples in MI

of GD [29]. This parameter had a different behaviour for each of the two registration combinations tested, as shown in figure 5.6. In case of Reg1, the best result was 0.00001 and it was not possible to perform the tests for 10 and 100, as the source image was outside of the reference image. In case of Reg6, the best result was 10, so we chose different values according to the combination. When the registration uses Affine transformation (Reg1, Reg3 and Reg5), we chose 0.00001 and for the cases with B-Spline transformation (Reg2, Reg4 and Reg6) we chose 10 as the learning rate value.

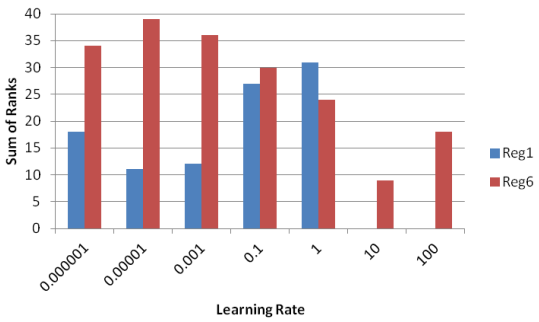

Figure 5.6: Optimization Ranks of Learning Rate in GD Optimizer

Number of Iterations in GD Optimizer

For this optimization, the same combinations as for the last one were used to test the parameter: Reg1 and Reg6. To perform the evaluation of the number of iterations that is needed to achieve the optimal result in the registration process along 1500 iterations, the metric value of Reg1 and Reg6 were tracked. In the figure 5.7 it is possible to see that at 500 iterations the metric of Reg1 has the best result, however Reg6 has the best value at 750 iterations. The final result shows the best result is at 500 iterations, which was chosen as optimized value for this parameter. Another fact that influenced this choice, was that from 500 iterations and higher, the metrics are more stable, which indicates that the transformations are more similar from this point, which is shown in table A.6 of appendix A.2.

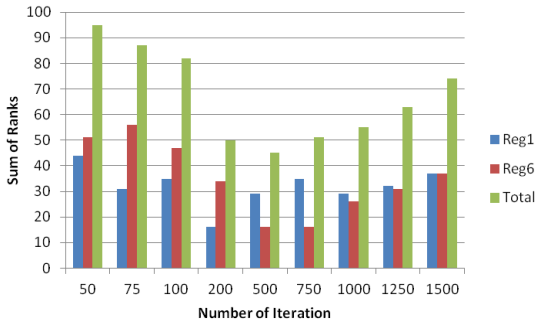

Figure 5.7: Optimization Ranks of Number of Iterations in GD Optimizer

Step Length in Powell Optimizer

For the optimization of Powell optimizer parameters, the combinations used were the two best registrations that used this optimizer. One of the combinations used Affine Transformation (Reg11) and the other B-Spline Transformation (Reg8). As shown in figure 5.8 the best result for Reg8 was 0.0001 and for Reg11 it was 0.001, but the final rank for 0.001 obtains the lowest rank and so it was chosen as optimized value of the parameter in cause.

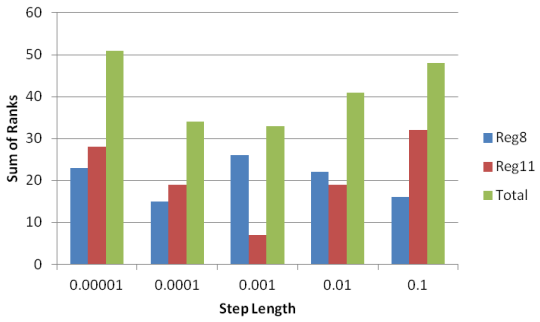

Figure 5.8: Optimization Ranks of Step Length in Powell Optimizer

Value of Tolerance in Powell Optimizer

The test performed for this parameter produced the same results for the tested values (0.0000001, 0.000001, 0.00001, 0.0001 and 0.001). So, it was chosen as the default value of ITK to be used in the registration methods, which is 0.00001 [21].

Maximum Number of Iterations in Powell Optimizer

As this value is only a security value to not perform infinite iterations, optimization tests were not performed; since in preliminary tests, the processes Reg8 and Reg11 have achieved the convergence and stopped at iteration 0 and 2 respectively. So, we chose the same result for Number of Iterations in GD, as explained above (500 iterations).

Order of Spline in B-Spline Transformation

The spline order in B-Spline transformation optimization was performed in combination with the best results obtained with this component is used (Reg6 e Reg8) for values 2, 3 and 5. Order 1 was not tested because it has the same linear transformation, and order 4 is not implemented in ITK [37]. Observing figure 5.9, the order with lowest sum of ranks for Reg6 is 3 and for Reg8 is 2, but the total rank is 3, so it was chosen as optimized parameter.

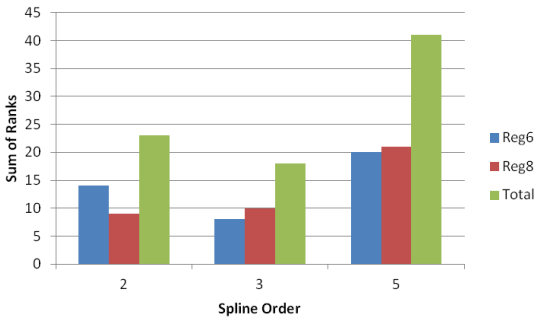

Figure 5.9: Optimization Ranks of Spline Order in B-Spline Transformation

5.1.3 Post-Optimization Analysis

After optimizing the registration parameters, all combinations were performed again. As an example, in figure 5.10 is a graphic of NMI values, before and after the optimization. It is possible to see that not all combinations produce an improvement when compared with the pre-optimization results. This is mainly due to the parameter optimizations that were made independently for each of the parameters. The results of all metrics for all combinations are shown in table A.2 of appendix A.1.

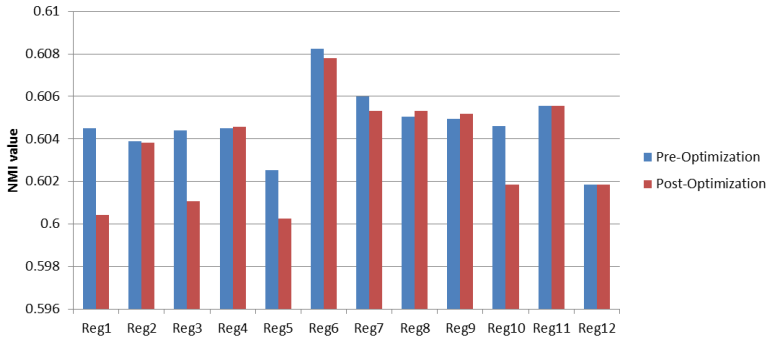

Figure 5.10: Comparison NMI values of pre- and post-optimization results

Figure 5.11 shows the comparison between the sum of ranks before and after optimizations, where it can be seen that the best registration combinations are Reg11, Reg6 and Reg8 which obtained the smallest values in the sum of ranks. Taking the three combinations into account, Reg11 and Reg6 have the smallest processing times, and so they were considered the best registration combinations for simulated data.

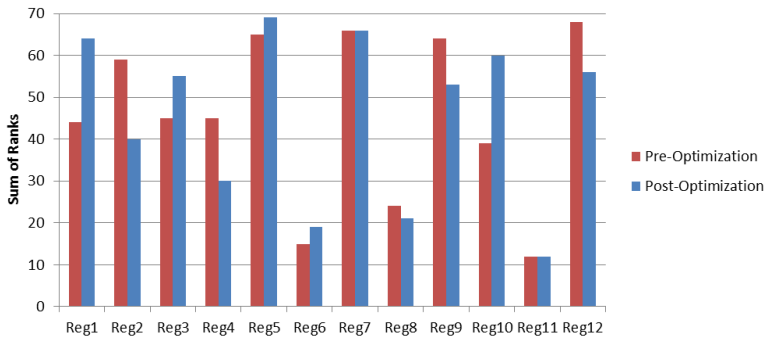

Figure 5.11: Sum of ranks of post-optimization results for registration methods using simulated data

5.1.4 Evaluation of Simulated Data

An important analysis is the comparison of registration components, because it allows undestanding the several components and their relationship. For Affine and B-Spline transformations, the mean results of sum of ranks are shown in figure 5.12a. There, it is possible to see that B-Spline obtains, in general, the best results, but the best combination of all (Reg11) used Affine transformation, which may be due to other registration components. The Kruskal-Wallis test was performed and it was possible to see that there is no significant statistical difference between the groups. In the time analysis, it is possible to see that the several combinations with B-Spline transformation had obtained a greater mean value of the execution time, than the combinations with Affine transformation (see figure 5.12b). This fact may be due to the larger number of parameters of B-Spline when compared with the other transformation. However, the ANOVA analysis shows that both cases have no significant statistical difference. So B-Spline is a better transformation in terms of performance. However, execution time is the longest.

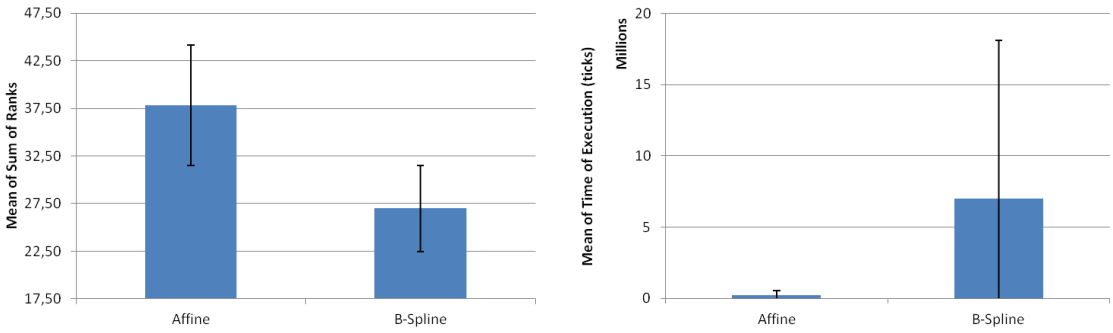

(a) Mean of Sum of Ranks

(b) Mean of Execution Time

Figure 5.12: Comparison of transformations in registration components

The interpolators studied were Linear, B-Spline and Nearest Neighbour and their mean sum of ranks values are shown in figure 5.13a. Nearest Neighbour interpolator has a better mean value compared with the other interpolators; this may be due to the Nearest Neighbour not creating new intensity values. The other two interpolators obtained similar values. However, B-Spline obtained the worst value. The Kruskal-Wallis test has showed again that the groups have no statistical difference. The execution time analysis (see figure 5.13b) shows that B-Spline combinations have

a greater mean value of execution time, due to the larger quantity of calculations in this kind of interpolator. B-Spline interpolator is followed by the Linear interpolation for the mean value of execution time. The interpolator with lowest time of execution was Nearest Neighbour, which is normal due to the small number of calculations performed, when compared with the other two. Once again, the ANOVA analysis shows that none of the groups are statistically different. In the interpolator analysis it is possible to see that Nearest Neighbour not only obtained the best mean value of ranks, as well as the lowest time of execution, being the better interpolator from all that were studied.

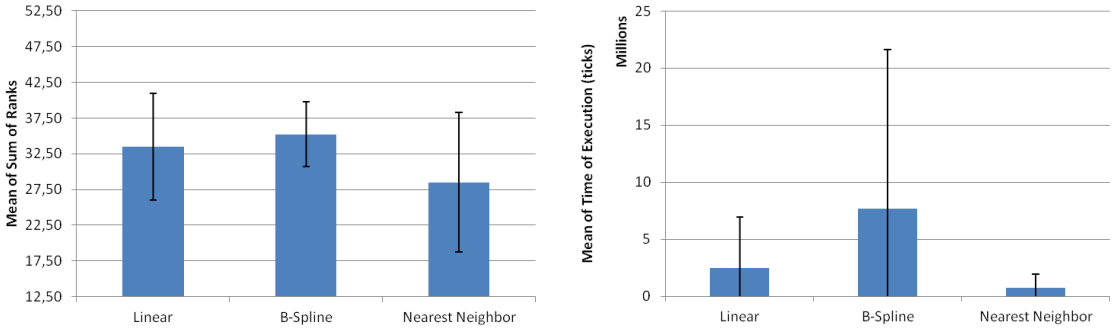

(a) Mean value of Sum of Ranks **(b)** Mean value of Execution Time

Figure 5.13: Comparison of interpolators in registration components

For the optimizers the mean values of the sum of ranks are shown in figure 5.14a. It can be observed that there is not a big difference, but Powell has a slight advantage over the GD optimizer. This may happen because Powell achieves the best metric value, while the GD stops at the user-defined number of iterations, and therefore the best metric value could not be obtained. The Kruskal-Wallis test produces a similar result as the anterior cases. The time analysis presented in figure 5.14b shows that the combination with Powell optimizer obtained a greater mean value than GD optimizer, maybe due to the greater number of calculations of the optimizer. The large standard deviation of the Powell optimizer is due to the variance of the number of iterations in this method that is not fixed, contrary to the mean GD optimizer. The ANOVA analysis shows that the groups are statistically similar, as in the previous cases. Concerning the optimizers, Powell obtained a better performance result. However, it obtained the greater time of execution in average.

Another important analysis performed, was the influence of RMS and Dice Coefficient on the assessment, due to the impossibility of performing these metrics in some or all the real data. RMS cannot be performed with all real data because this is an accuracy metric, and it is not possible to have the EPI without distortion, only an approximation, which is the structural MPRAGE. The problem of Dice Coefficient in real data analysis is the impossibility of performing a segmentation on the images with b=8000, due to very low SNR. The results from this analysis are shown in table 5.2, where the exclusion of RMS from the analysis does not change the best three results. The same happened with the exclusion of Dice Coefficient, and so real data can be analyzed without performing these two evaluation metrics.

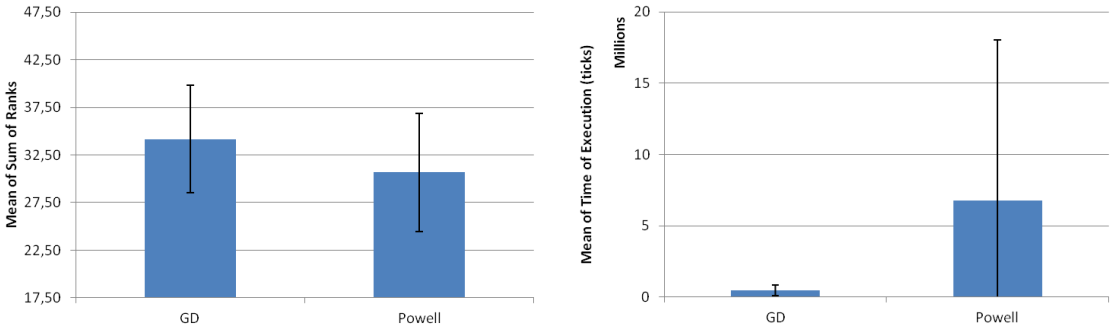

(a) Mean value of Sum of Ranks **(b)** Mean value of Execution Time

Figure 5.14: Comparison of optimizers in registration components

Table 5.2: Ranks comparison with and without RMS

	Reg11	Reg6	Reg8	Reg4	Reg2	Reg9	Reg3	Reg12	Reg10	Reg1	Reg7	Reg5
Complete	12	19	21	30	40	53	55	56	60	64	66	69
Without RMS	10	18	18	26	33	48	49	45	48	55	56	61
Without RMS+Dice	5	11	9	16	18	21	24	22	25	29	23	31

5.2 Validation of Simulated Data

After performing all the registration methods with simulated data and optimized parameters, it was necessary to perform the same combinations for real data with b=0, to ensure that results of simulated data are valid and the conclusions can be used for real data. Initially, the metric values for simulated and real data were compared (see table A.2 in appendix A.1 for simulated data results and table B.1 in appendix B.1 for real data). It is also important to say that the combinations Reg8, Reg10 and Reg12 were not completely performed for real data, due to the execution time that exceeded 8 hours of processing, and this is impracticable in a clinical environment, so we do not have evaluation results.

Figure 5.15 shows the comparison between the same metric values for real and simulated data. The NMI results are from a similar order of magnitude, but real data are slightly superior to simulated data (see figure 5.15a). SCC analysis shows that real data have lower results than simulated data (see figure 5.15b), this is maybe due to the difference between the corrected image and the structural data, that do not have the same intensities. For the Dice Coefficient analysis, the results were similar to the SCC comparison, maybe due to some divergences in two segmentations (MPRAGE and corrected EPI's). This could have happened because they are images from different sequences where tissues have different weights, which influences the segmentation and posterior analysis. Finally for Euclidean Distance of CM, it is possible to see by figure 5.15c, that the results from the combinations with GD optimizer and Affine transformation (Reg1, Reg3 and Reg5) have better results for real data than for simulated data. However, the combinations with the same optimizer and B-Spline transformations (Reg2, Reg4 and Reg6) have greater distances in real data than simulated data. The same happened to the combinations with Powell optimizer and Affine transformation, that obtained worse results for real data. It is not completely understood why the differences in the Euclidean Distance of CM occur. However, these are maybe due to the more difficult registration

in real data, due to the differences of intensities of MPRAGE and EPI, which also influence the analysis of CM.

These are interesting facts that show that there exists some similarity between real and simulated data with some metrics, but regarding others there exists a great discrepancy between simulated and real data. These differences may be due to the errors in simulated data described by Drobnjak *et al.* [40] that indicate an error of 3% for the size of voxels used in this project.

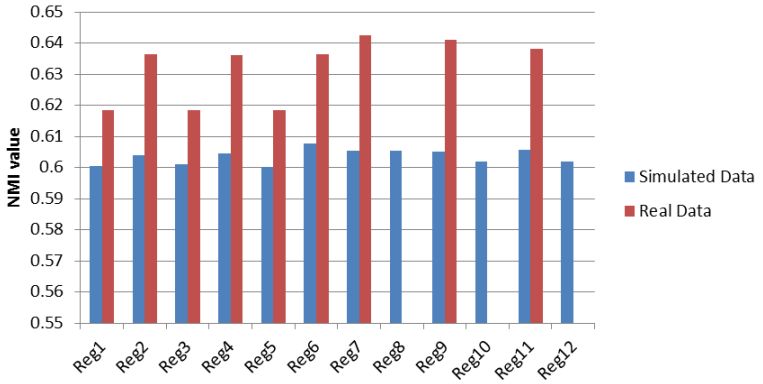

(a) NMI

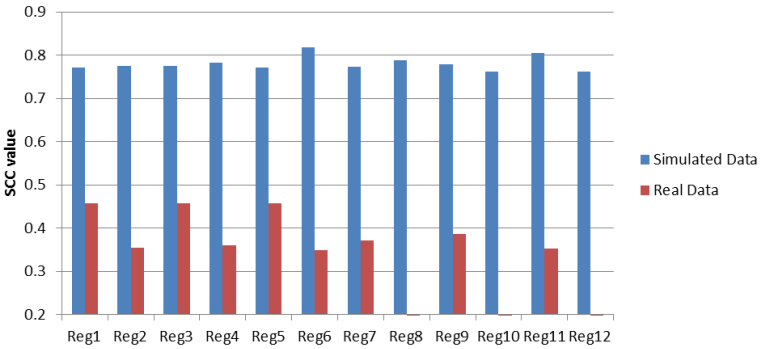

(b) SCC

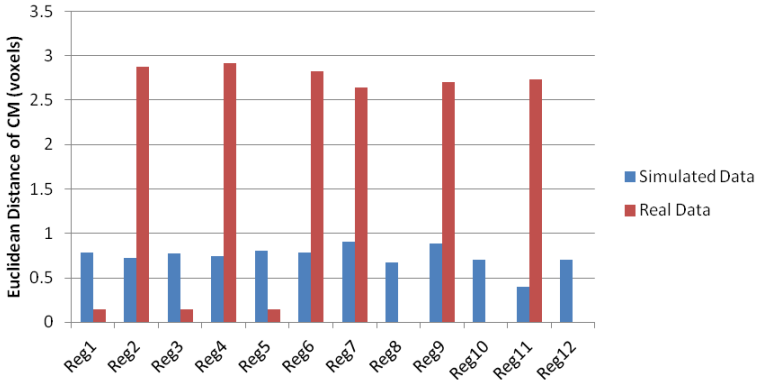

(c) Euclidean Distance of CM

Figure 5.15: Comparison of evaluation metrics, between real and simulated data. Reg8, Reg10 and Reg12 do not have values using real data, because they were not performed due to the long execution time

It was also important to perform an analysis of the comparison between the combinations, having in consideration the relation between them, for that we used the mean of ranks of the several

metrics, and the results are shown in figure 5.16. In this analysis, the sum of ranks was not used, because the number of metrics calculated in the real and simulated cases is different, so a mean value of the ranks of metrics gives values in the same range, contrary to the sum of ranks. Analyzing figure 5.16, it is possible to see that the best result in simulated data is one of the best for real data. However, the best result in real data is one of the worst for simulated data. The combinations with best results in metrics are Reg7, Reg9 and Reg11. However, considering the time of execution of the combinations, Reg7 and Reg11 obtain the best times (Reg7 - 2029883 ticks; Reg9 - 10554118 ticks; Reg11 - 1853831 ticks). Therefore, the combinations Reg7 and Reg11 were chosen, as they achieved the best results and lowest times of processing.

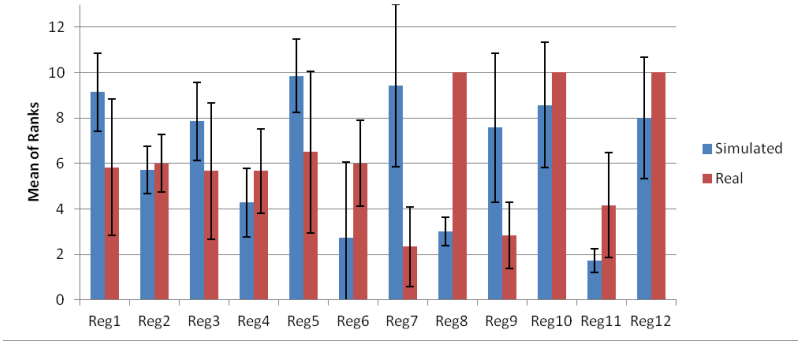

Figure 5.16: Comparison between mean of ranks of simulated and real data

5.3 Real Data

Here we show the results and evaluation of the different correction methods tested and the interference of the *b*-value in the correction process. The evaluation metrics of this section of the project were NMI, SCC and Euclidean Distance of CM and not all the metrics proposed for simulated data. This is explained on section 4.5 and corroborated by the results of table 5.2. The results of this part of the project are showed on appendix B.

5.3.1 Methods Evaluation

The results for *b*=0 of the correction methods proposed are showed on figure 5.17. Visually the results seem to be similar, but analyzing the results with the explained metrics, the results are different, as it is showed on table B.2 on appendix B.2. In figure 5.18 there is the sum of ranks of the evaluated metrics, and it is possible to see that all the methods improve the image when compared with the original distorted EPI. It is also possible to say that Registration methods obtain a better result than Field Map correction. Finally the pipeline used with Reg7 and Reg11 improved the result compared with the correspondent registration.

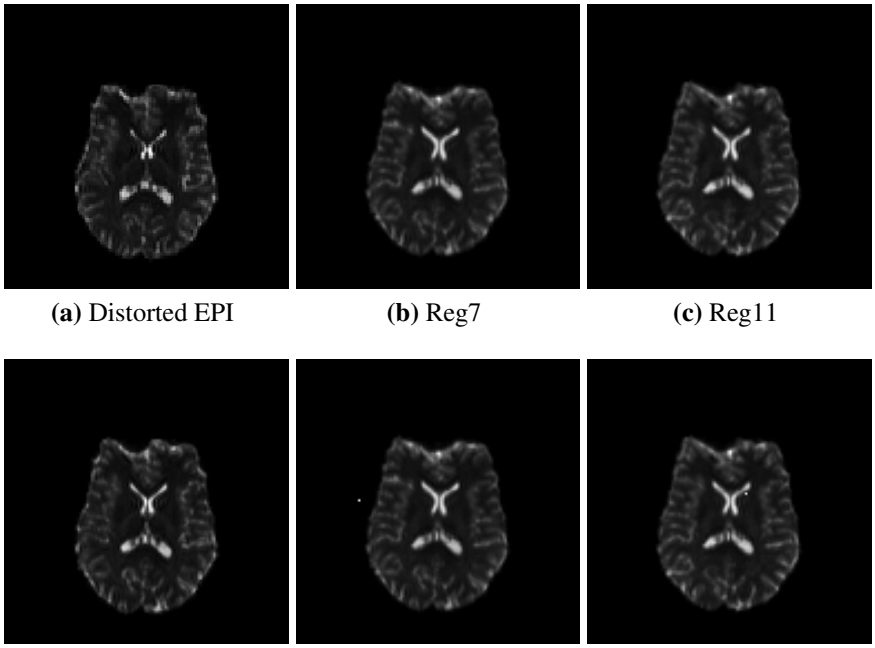

(a) Distorted EPI **(b)** Reg7 **(c)** Reg11

(d) Field Map **(e)** Reg7 + Field Map **(f)** Reg11 + Field Map

Figure 5.17: Results of real data correction for b=0

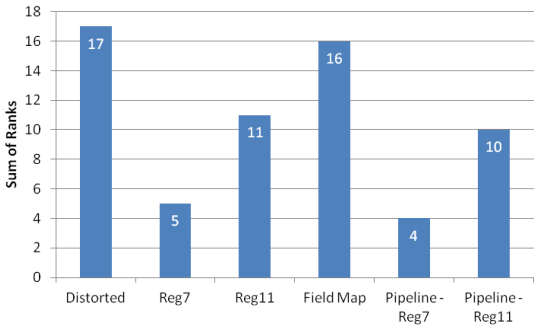

Figure 5.18: Sum of Ranks of correction methods used in real data with b=0

5.3.2 *b*-value Evaluation

To analyze the influence of b-value in the correction it was needed to group the results by the b-value, that is, for each b-value there are several images from different orientations and they were grouped together. Therefore, it was calculated the mean for each metric result and verified by an ANOVA statistics test and a Post-Hoc test that the groups are independent. Figures 5.19a, 5.20a and 5.21a show means of the groups for the each b-value for the three metrics studied and the respective values are showed on appendix B.3. The p-value of each case for all the metrics was smaller than 0.05, which means that the null hypothesis is rejected and that the major part of groups is statistically different. However, by the Post-Hoc analysis it was possible to see that not all the groups were statistically different. In case of NMI, in the Reg11-based methods only b=8000 are statistically different, and for the Field Map correction, the cases of b-values higher than 1000 were statistically different from the cases with b=0 and b=1000. For SCC, all the cases were statistically independent. Finally for the cases of Euclidean Distance of CM, b=8000 was

statistically similar for for all the methods, and in cases of the original distorted EPI and Field Map correction the b=0 was also statistically different.

Following will be showed the results of the metrics for the several b-values and methods. We will also shows the results of the percentage of improvement of the different metrics comparatively with the distorted EPI.

The results of NMI are showed on figure 5.19a, where we can see that the metric is decreasing with the increasing of b-value. At b=8000 this decreasing is abrupt, may be due to the quantity of noise on this kind of images and because it was not possible to perform BET over these images, due to the noise. The improvement results for NMI are showed on figure 5.19b, where it is possible to see that for b=1000 there is a decrease of improvement, relatively to b=0. After that, there is an increase of improvement with the increasing of the b-value. This relation between the b-values is maintained for all the methods except for Field Map correction, where the behaviour is inversely and from a lower order of magnitude. So, in most of cases, for NMI the increasing of b-values reduces robustness of the method. However, this increasing of b-value, also increase the improvement of the metric.

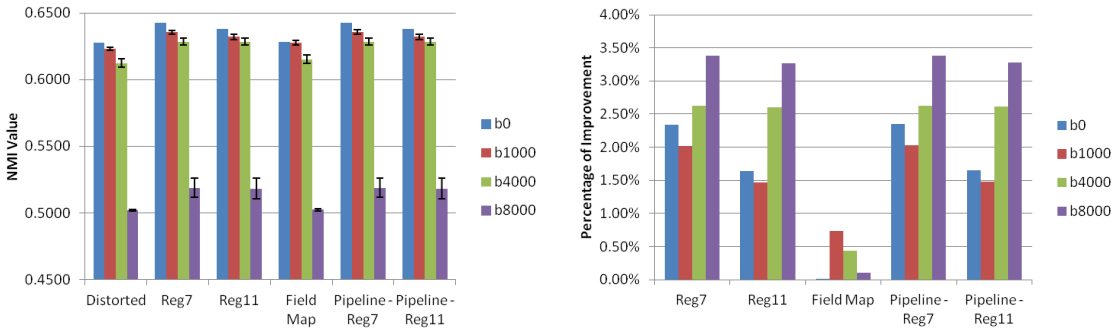

(a) Metric mean **(b)** Percentage of Improvement

Figure 5.19: Results of NMI for different methods and b-values

The metric results of SCC are showed on figure 5.20a, where it is possible to see that the b-value does not produce a monotonous trend. The b=1000 results increase the metric values, compared with b=0, and the same for b=4000. However for b=8000 the metric value decreases. For b=8000, the quantity of noise existent in the images, produces a small variance in the images, contrary to the MPRAGE that has a 'black' background, which will produce a variance over the brain intensities, decreasing the final value of the metric. The same should happen for the b-values of 1000 and 4000. However, this does not happen, maybe because the characteristics of the images, that in intensity are more similar with the MPRAGE intensities, thus improving the SCC value. The improvement analysis of SCC is showed on figure 5.20b, and the analysis is similar to the NMI analysis, however for b=8000 the improvement is much greater than for the other b-values. This greater improvement in b=8000 images is probably due to the low metric value of MPRAGE, where a small increasing in the metric causes a large improvement compared with the initial value.

Finally, analyzing metric results of Euclidean Distance of CM on figure 5.21a, we can see that it has a similar behaviour to SCC because there is an increasing of the metric for b-values of 1000 and

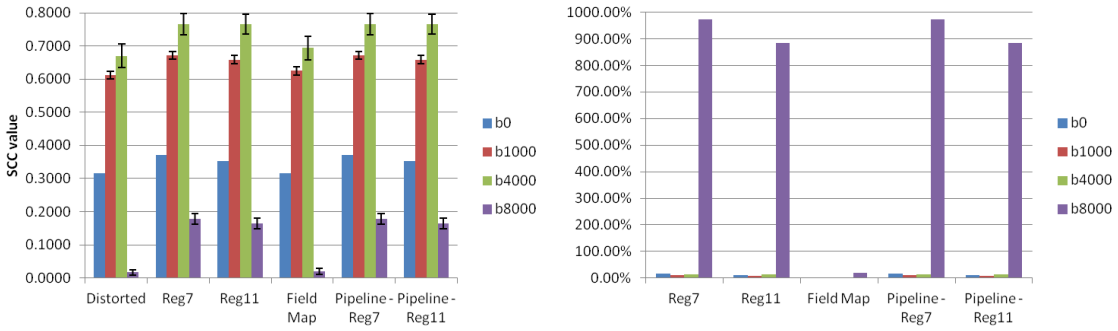

(a) Metric mean **(b)** Percentage of Improvement

Figure 5.20: Results of SCC for different methods and *b*-values

4000, which is transduced by a minor distance than the *b*=0. However, for the *b*=8000, the distance is even larger than *b*=0 and with a major variance. This is probably due to the impossibility of performing a brain extraction in this kind of images. The same explanation given for SCC about the unexpected behaviour of *b*-values equal to 1000 and 4000, can be given to Euclidean Distance of CM, because the CM are directly related with the voxels intensities. This fact does not happen for NMI, because with this metrics it is assessed the distribution of intensities (histogram and joint histogram) and not the intensities directly. The results of the improvement of Euclidean Distance of CM are showed on figure 5.21b and it is visible that the improvements increase with the increase of *b*-value until the value 4000, and after that there is an abrupt decrease for the value 8000. This fact can be related with the impossibility of performing a brain extraction, which influences the results of CM.

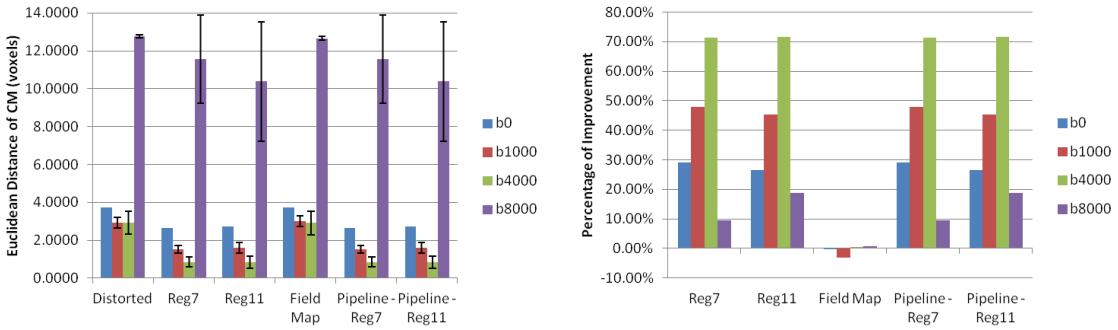

(a) Metric mean **(b)** Percentage of Improvement

Figure 5.21: Results of Euclidean Distance of CM for different methods and *b*-values

It is also important to say, that Field Map correction always shows the lowest results in the metrics values and in the percentage of improvements. In some cases the results of the improvements obtained negative values. These results can be explained by a misalignment of the results of Field Map correction, when compared with the Registration-based method results, which have an alignment in their own method, improving the results.

5.3.3 Global Evaluation

Finally, it was important to analyze globally the results, comparing the influence of the methods and the *b*-value simultaneously. For that purpose, all the values of each evaluation metric were ranked for each *b*-value and summed respectively between them, for example the rank of distorted EPI for *b*=0 in the NMI results were summed with the correspondent result in SCC and Euclidean Distance of CM and it was created a table of *b*-value versus the methods evaluated (see figure 5.22), which shows the comparison of the different methods in the different *b*-value images. It is possible to see that the correction over different *b*-values have similar behaviours. However, the difference between the sums of ranks is not the same; this means that for a specific *b*-value, the result of sum of ranks is not the same for all the *b*-values. For example, for *b*-values equal to 0 and 1000 the sum of ranks of the Distorted EPI are 17, while for the other *b*-values are 18, which indicates that we obtain worse ranks results in more metrics.

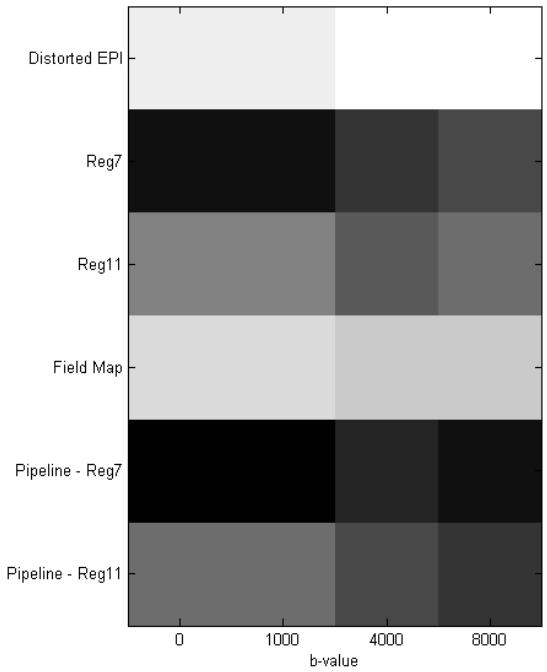

Figure 5.22: Ranking of methods VS *b*-value. Lighter colours mean worse results, and darker colours mean better results

Chapter 6

Discussion

In this chapter the results obtained in this project it will be explained. First the simulated data was used to optimize the registration parameters. The real data was used to chose the best combination of registration, to compare the three correction methods used (Registration, Field Map and the Pipeline proposed) and to evaluate the performance of correction methods with variance of *b*-value.

6.1 Simulated Data

6.1.1 Optimization

The optimization of registration parameters has the importance of achieving the parameters values that produce the best results in a reasonable time. This is because if a parameter value change results in a minor improvement when compared with a major increasing of time, it is considered a unsatisfactory optimization. This fact has a major importance in the number of samples in MI, and in the number of iterations in the registration process. In the first case it can be seen by the results that the increasing of number of samples does not make great improvements in the process, but increases the time greatly, so it was chosen a small number of samples that maintain the performance of the method and did not increase the time of execution of the process. For the number of iterations in GD the optimization was not only based on the best result, it was also considered the point from where the metrics becomes more stable, which happens at 500 iterations. The other parameters had a simpler optimization, and it was chosen the best result for each parameter. It should be noted that the optimization of learning rate in GD optimizer does not produce a simple value, but two. One for the combinations with Affine transformation and other for the methods with B-Spline transformation. This happened due to the large difference in the number of parameters of transformations [29], B-Spline has more parameters than Affine and so it needs a big learning rate to be able to optimize all the parameters of the transformation in the same number of iterations.

6.1.2 Evaluation

The post-optimization results show that the best combinations are Reg11, Reg6 and Reg8. But the time of execution is an important factor, so it must be considered in the analysis. The time of execution is important, because a very good combination in the metrics evaluation with a very high execution time, is not a good process. This happens because these methods are supposed to be used in clinical environment, and so the processing time is an important issue. So from the three best combinations, there were chosen the two with slower execution time, they were Reg6 and Reg11.

It was also compared the difference in the results for each registration components. Optimizers and Interpolators do not show a big difference between them, but Powell optimizer has a slight advantage over GD and Nearest Neighbour obtained by best mean results when compared with the other two interpolators. Transformation analysis shows that B-Spline obtains a better result in the majority of the combinations than Affine transformation. It was also noted that Affine transformation obtained a best time of execution, due to the less number of parameters when compared with B-Spline. Nearest Neighbour also obtain the lower time of execution due to the less computation needed to this interpolator. Finally, GD optimizer also obtained the best time of execution, due to the less calculations performed by this optimizer when compared with Powell. It was also interesting to see that Powell had a high standard deviation in time of execution, probably because the differences in the number of iterations of this methods, that is not fixed as GD optimizer.

It was seen that the RMS evaluation does not change the best methods, as well as the Dice Coefficient. So they were removed from the posterior analysis. This is important because RMS cannot be performed on real data, because it is an accuracy measure, that can only be performed if the reference image is a EPI without distortion and not the MPRAGE, that has different intensities. The same was made for Dice Coefficient, that was not performed in real data too, due to the b=8000 where is not possible to perform segmentation due to the low SNR.

6.2 Validation of Simulated Data

With the comparison between the real and simulated data it was possible to see that there is some similarity and some divergences between the two. It is true that the best combination for simulated data is one of the best in real data, but the best combination in real data is one of the worst in simulated data. So, the simulated data is not invalidated in analysis of the correction methods, however, it is necessary to have precaution in future works, and compare with real data to understand the similarities and divergences between both.

6.3 Real Data

6.3.1 Methods Evaluation

Assessing the methods tested for b=0 it is possible to say that Registration and pipeline methods obtained best values than the Field Map method. It is also possible to say that there is not a big difference between the registration and pipeline methods, maybe because its difference is only the application of Field Map method over the registered image. However, the Field Map method produces an improvement relatively to the original data. The results of Field Map correction were not so good as expected maybe due to the misalignment of the resultant image with the control structural data (MPRAGE). This misalignment is showed by the Euclidean Distance of CM, where the Field Map correction obtained results similar with the distorted EPI, so it is not spatially closer to the MPRAGE. This does not happen in registration based methods, where the images are aligned by the method itself, which not happen in Field Map correction, because the image is only resampled for the respective size and not registered. These results can also be related to the evaluation metrics, which could induce in error the result.

6.3.2 *b*-value Evaluation

In the analyzed cases, the worst results were obtained for b=8000. This is caused by the quantity of noise of these images, and the impossibility to perform a brain extraction. This is an important fact, because the noise can influence the evaluation metrics as said by De Wilde *et al.* [50]. The quantity of noise can also influence the registration damaging the result. The unexpected result of improvement of the metrics SCC and Euclidean Distance of CM for the b-values of 1000 and 4000, is probably due to the images intensities, that can be similar to the MPRAGE intensities, causing better results than for b=0.

However, if we analyze the improvement in percentage, the higher b-values obtain best results for NMI and SCC. For the CM, the improvements increase until b=4000, and for 8000, the values decrease for smaller values than the other b's, maybe due to it was not possible to perform a brain extraction, because of the quantity of noise of these type of images. Also in the improvements, it was possible to see that Field Map correction obtained lower values of improvement, and in some cases negative values. This fact can be explained, again, by the misalignment of the result of this method with the MPRAGE, because the method do not include a alignment, which happens with the registration-based methods.

6.3.3 Global Evaluation

Globally, the results obtained are similar for all the b-value in terms of ranking between the methods, which indicates that b-value does not influence the methods between them. So, it is possible to say that the correction can have different results of metrics and improvements, but the relation-

ship between them (ranks) has the same behaviours for the different *b*-values, thus all the images studied must be corrected.

Chapter 7

Conclusion

The main objective of this project was to find the best correction method for spatial distortions from the studied ones (Registration, Field Map and Proposed Pipeline) and study the influence of the *b*-value in the correction. The methods, Registration and Field Map, were chosen because they are the most used in the literature, and a new one, that is the combination of those with the intention of obtaining the advantages of both of them.

It was used simulated and real data in this project. The simulated data was used to optimize the registration parameters, due to the possibility of using accuracy metrics such as RMS and Dice Coefficient.

Before the analysis of the methods proposed in the real data results, it was necessary to validate the simulated data, performing the same combinations of Registration in the real data. The results are showed on image 7.1 where it is possible to see that Reg7, Reg9 and Reg11 obtained the best results in the performance analysis. However it was chosen Reg7 and Reg11 to apply in the real data due to the lower time of execution. It was concluded that the use of simulated data should be done with caution, because there are some divergences with the real data, already described by Drobnjak *et al.* [40]. These errors make difficult the validation of simulated data.

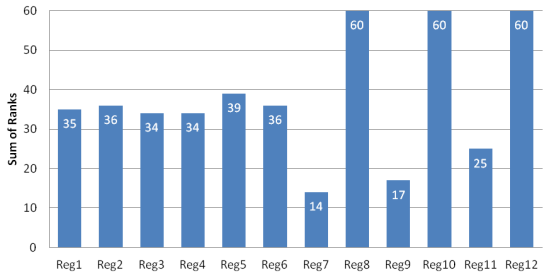

Figure 7.1: Sum of ranks of registration methods in real data

For the real data, it was used *b*=0 to evaluate which is the best method. The results are showed on figure 7.2 where it is possible to see that the registration-based methods are better than Field Map.

Finally the study of the influence of *b*-value in the correction shows that the higher *b*-values obtained worst results in absolute values than lower *b*-values, except for *b*=8000. Taking into account

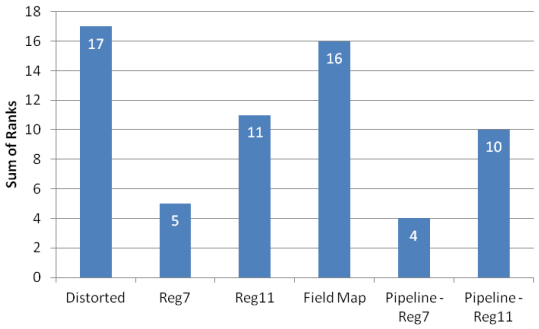

Figure 7.2: Sum of Ranks of correction methods used in real data with b=0

the percentage of improvement (percentage of change in metric value) relatively to the control image, the best results are obtained by the higher *b*-values too. So, for higher *b*-values the metrics became best, and obtain a greater improvement to the control image relative to the original image. However, this fact can be related with the characteristics of the image itself and not the correction. So it is important to correct images with all the *b*-values tested, to decrease the quantity of spatial distortion that the images have.

In brief, this project was useful in the field of Spatial Distortion correction of MRI, particularly DW-MRI, to a better understanding of the studied methods and the influence of *b*-value in the correction methods. It was also important to understand that noise influences the results.

7.1 Limitations and Future Work

The simulated images do not completely mimic the real images, which is a major problem. This was most seen in the Field Map correction, since it was not possible to perform this correction with simulated data. A possible solution to this problem is to develop a MRI simulator that permits to obtain images closer to the real data and that permits to create diffusion MRI data, so that is possible to analyze this sequence more accurately.

Another wide field of interest in Spatial Distortions correction that could replace the simulated data and their inherent errors is the study of corrections over phantoms. This study is already being done, however for DW-MRI it can be improved with new physical phantoms designs [3, 18–20]. This area has great interest in this field because joins the existence of a *Gold Standard*, as simulated data, but with a real acquisition, that includes real noise a distortions from the MR systems, as real data.

Another problem was the long time that some registration methods take to perform. This makes it nearly impossible to test more combinations and make more exhaustive tests of the optimization level. In a longer research, probably it would be possible to investigate these factors, and obtain a more thorough analysis of Registration.

The validation of simulated data with the real data was a big concern and could be a very important field of research in the future, due to the high uncertainty in the behaviour of simulated data, and

its lack of similarity to real images.

The noise of the images was another issue especially in the assessment of the results. Noise is a major factor in the metrics, and influences the results. It could influences the correction methods, and the evaluation metrics. Some studies about the noise influence were already done [50]. However it should be performed a study not only about the influence of noise in the images e metrics, but over the evaluation metrics itself, where it would be considered the noise and the characteristics of the images, being of great utility in further research.

7.2 Final Work Assessment

This project has greatly contributed to my improvement, in personal, academic and professional ways. It gave me the chance to learn a lot of new concepts in the fields of MRI, spatial distortion and image processing, which enlarges my knowledge scope.

During the project, I needed to learn and interact with software tools which are an added value to my curriculum, and which are likely to be useful to my future. One of these tools was FSL, which given me the chance of develop a software guide (see appendix C) that was useful not only for me, but to all persons in the research group.

Working in a research group was important to me, because it was possible to discuss ideas with PhD and MSc, hence improving my projects.

It was possible to submit one extended abstract named *"Pipeline for Spatial Distortion Correction in MRI"* for the *"4th International Symposium on Applied Sciences in Biomedical and Communication Technologies"* (ISABEL 2011). This paper (see appendix D) has been accepted and will be presented in October at Barcelona and published in *ACM Digital Library*, which is important for project validation.

The company environment was of a great value to me, because I learned how a company works inside, and how people can work together towards the same objective.

This project had some hurdles during its development, but they were useful to understand some of my weaknesses, and challenged me in a positive way.

In brief, I think this project has gone well, due to the learned skills and to the experience obtained.

Bibliography

[1] D. Xu, M. C. Lee, J. Carballido-Gamio, M. Barkovich, S. Majumdar, D. B. Vigneron, and S. J. Nelson, "Quantitative analysis of spatial distortion of diffusion techniques at 3T," *Magnetic Resonance Imaging*, no. 28, pp. 451–454, 2010.

[2] H. Johansen-Berg and T. E. J. Behrens, *Diffusion MRI - From quantitative measurement to in vivo neuroanatomy*, 1st ed. London: Academic Press, 2009.

[3] D. M. Wang and D. M. Dodrell, "Geometric distortion in structural magnetic resonance imaging," *Current Medical Imaging Reviews*, vol. 1, no. 1, pp. 49–60, 2005.

[4] P. Jezzard and S. Clare, "Sources of distortion in functional MRI data," *Human Brain Mapping*, vol. 8, pp. 80–85, 1999.

[5] U. Techavipoo, J. Lackey, J. Shi, X. Guan, and S. Lai, "Estimation of mutual information objective function based on Fourier shift theorem: an application to eddy current distortion correction in diffusion tensor imaging," *Magnetic Resonance Imaging*, vol. 27, pp. 1281–1292, 2009.

[6] P. J. Kostelec and S. Periaswamy, "Image registration for MRI," *MSRI Publications*, vol. 46, 2003.

[7] P. Jezzard and R. S. Balaban, "Correction for geometric distortion in echo planar images from b0 field variations," *Magnetic Resonance in Medicine*, vol. 34, no. 1, pp. 65–73, 1995.

[8] L. N. Baldwin, K. Wachowicz, and B. G. Fallone, "A two-step scheme for distortion rectification of magnetic resonance images," *Medical Physics*, vol. 36, no. 9, pp. 3917–3926, 2009.

[9] P. S. Morgan, R. W. Bowtell, D. J. O. McIntyre, and B. S. Worthington, "Correction of spatial distortion in EPI due to inhomogeneous static magnetic fields using the reversed gradient method," *Journal of Magnetic Resonance Imaging*, vol. 19, no. 4, pp. 499–507, 2004.

[10] D. Holland, J. M. Kuperman, and A. M. Dale, "Efficient correction of inhomogeneous static magnetic field-induced distortion in echo planar imaging," *Neuroimage*, vol. 50, no. 1, pp. 175–183, 2010.

[11] E. M. Haacke, *Magnetic resonance imaging: physical principles and sequence design*. J. Wiley & Sons, 1999.

[12] M. A. Brown and R. C. Semelka, *MRI - Basic Principles and Applications*, 3rd ed. Hoboken, New Jersey, USA: Wiley-Liss - John Wiley & Sons, Inc, 2003.

[13] A. Hendrix, "Magnets, spins, and resonances - an introduction to the basics of magnetic resonance," Germany: Siemens AG Medical Solutions, 2003.

[14] D. Weishaupt, V. D. Köchli, and B. Marincek, *How does MRI work?* San Diego: CA: Academic Press, 2000.

[15] J. T. Bushberg, *The essential physics of medical imaging*. Lippincott Williams & Wilkins, 2002.

[16] C. Westbrook and C. Kaut, *MRI in practice*, 2nd ed. Oxford: Blackwell Publishing, 1998.

[17] R. Cusack, M. Brett, and K. Osswald, "An evaluation of the use of magnetic field maps to undistort echo-planar images," *NeuroImage*, no. 18, pp. 127–142, 2003.

[18] D. Wang, D. M. Doddrell, and G. Cowin, "A novel phantom and method for comprehensive 3-dimensional measurement and correction of geometric distortion in magnetic resonance imaging," *Magnetic resonance imaging*, vol. 22, no. 4, p. 529–542, 2004.

[19] S. Mattila, V. Renvall, J. Hiltunen, D. Kirven, R. Sepponen, R. Hari, and A. Tarkiainen, "Phantom-based evaluation of geometric distortions in functional magnetic resonance and diffusion tensor imaging," *Magnetic Resonance in Medicine*, vol. 57, no. 4, p. 754–763, 2007.

[20] M. Perrin, C. Poupon, B. Rieul, P. Leroux, A. Constantinesco, J. F. Mangin, and D. LeBihan, "Validation of q-ball imaging with a diffusion fibre-crossing phantom on a clinical scanner," *Philosophical Transactions of the Royal Society B: Biological Sciences*, vol. 360, no. 1457, p. 881, 2005.

[21] L. Ibáñez and Insight Software Consortium, *The ITK software guide: updated for ITK version 2.4*. Kitware, 2005.

[22] J. C. Haselgrove and J. R. Moore, "Correction for distortion of echo-planar images used to calculate the apparent diffusion coefficient," *Magnetic Resonance in Medicine*, vol. 36, no. 6, pp. 960–964, 1996.

[23] S. Mohammadi, H. E. Möller, H. Kugel, D. K. Müller, and M. Deppe, "Correcting eddy current and motion effects by affine whole-brain registrations: Evaluation of three-dimensional distortions and comparison with slicewise correction," *Magnetic Resonance in Medicine*, 2010.

[24] N. Wiest-Daesslé, S. Prima, S. P. Morrissey, and C. Barillot, "Validation of a new optimization algorithm for registration tasks in medical imaging," in *Biomedical Imaging: From Nano to Macro, 2007. ISBI 2007. 4th IEEE International Symposium on*, 2007, pp. 41–44.

[25] F. Maes, D. Vandermeulen, and P. Suetens, "Comparative evaluation of multiresolution optimization strategies for multimodality image registration by maximization of mutual information," *Medical Image Analysis*, vol. 3, no. 4, pp. 373–386, 1999.

[26] J. F. Mangin, C. Poupon, C. Clark, D. L. Bihan, and I. Bloch, "Distortion correction and robust tensor estimation for MR diffusion imaging," *Medical Image Analysis*, vol. 6, no. 3, pp. 191–198, 2002.

[27] H. Lau, A. J. Ruys, P. Carter, X. Wang, and Q. Li, "Spatial correction of echo planar imaging deformation for subject specific diffusion tensor MRI analysis," in *IT in Medicine and Education, 2008. ITME 2008. IEEE International Symposium on*, 2008, pp. 703–708.

[28] F. Maes, A. Collignon, D. Vandermeulen, G. Marchal, and P. Suetens, "Multimodality image registration by maximization of mutual information," *Medical Imaging, IEEE Transactions on*, vol. 16, no. 2, pp. 187–198, 1997.

[29] G. K. Rohde, A. S. Barnett, P. J. Basser, S. Marenco, and C. Pierpaoli, "Comprehensive approach for correction of motion and distortion in diffusion-weighted MRI," *Magnetic Resonance in Medicine*, vol. 51, no. 1, pp. 103–114, 2004.

[30] T. Netsch and A. van Muiswinkel, "Image registration for distortion correction in diffusion tensor imaging," *Biomedical Image Registration*, pp. 171–180, 2003.

[31] T. Netsch and A. van Muiswinkel, "Quantitative evaluation of image-based distortion correction in diffusion tensor imaging," *Medical Imaging, IEEE Transactions on*, vol. 23, no. 7, pp. 789–798, 2004.

[32] M. Wu, L. C. Chang, L. Walker, H. Lemaitre, A. Barnett, S. Marenco, and C. Pierpaoli, "Comparison of EPI distortion correction methods in diffusion tensor MRI using a novel framework," *Medical Image Computing and Computer-Assisted Intervention - MICCAI 2008*, pp. 321–329, 2008.

[33] N. N. Mistry and E. W. Hsu, "Retrospective distortion correction for 3D MR diffusion tensor microscopy using mutual information and Fourier deformations," *Magnetic resonance in medicine*, vol. 56, no. 2, pp. 310–316, 2006.

[34] D. J. Kim, H. J. Park, K. W. Kang, Y. W. Shin, J. J. Kim, W. J. Moon, E. C. Chung, I. Y. Kim, J. S. Kwon, and S. I. Kim, "How does distortion correction correlate with anisotropic indices? a diffusion tensor imaging study," *Magnetic Resonance Imaging*, vol. 24, no. 10, pp. 1369–1376, 2006.

[35] D. T. B. Yeo, J. A. Fessler, and B. Kim, "Concurrent correction of geometric distortion and motion using the map-slice-to-volume method in echo-planar imaging," *Magnetic Resonance Imaging*, no. 26, pp. 703–714, 2008.

[36] D. Gallichan, J. L. R. Andersson, M. Jenkinson, M. D. Robson, and K. L. Miller, "Reducing distortions in Diffusion-Weighted echo planar imaging with a Dual-Echo Blip-Reversed sequence," *Magnetic Resonance in Medicine*, no. 64, pp. 382–390, 2010.

[37] "ITK - insight segmentation and registration toolkit."

[38] S. M. Smith, M. Jenkinson, M. W. Woolrich, C. F. Beckmann, T. E. Behrens, H. Johansen-Berg, P. R. Bannister, M. De Luca, I. Drobnjak, D. E. Flitney *et al.*, "Advances in functional and structural MR image analysis and implementation as FSL," *Neuroimage*, vol. 23, pp. 208–219, 2004.

[39] M. W. Woolrich, S. Jbabdi, B. Patenaude, M. Chappell, S. Makni, T. Behrens, C. Beckmann, M. Jenkinson, and S. M. Smith, "Bayesian analysis of neuroimaging data in FSL," *Neuroimage*, vol. 45, no. 1, pp. 173–186, 2009.

[40] I. Drobnjak and M. Jenkinson, "FMRI simulation and its application in modeling the interaction of motion and b0-inhomogeneities," in *Proceedings of 10th International conference for Functional Mapping of the Human Brain*, Budapest, 2004.

[41] I. Drobnjak, D. Gavaghan, E. S\Ã¼li, J. Pitt-Francis, and M. Jenkinson, "Development of a FMRI simulator for modeling realistic rigid-body motion artifacts," *Magnetic Resonance in Medicine*, vol. 56, no. 2, pp. 364–380, 2006.

[42] J. P. W. Pluim, J. B. A. Maintz, and M. A. Viergever, "Interpolation artefacts in mutual information-based image registration," *Computer vision and image understanding*, vol. 77, no. 2, pp. 211–232, 2000.

[43] ——, "Mutual-information-based registration of medical images: a survey," *Medical Imaging, IEEE Transactions on*, vol. 22, no. 8, pp. 986–1004, 2003.

[44] C. E. Shannon, "A mathematical theory of communication," *bell System Technical Journal*, vol. 27, no. 3, pp. 379–423, 1948.

[45] D. Mattes, D. R. Haynor, H. Vesselle, T. K. Lewellen, and W. Eubank, "Nonrigid multimodality image registration," in *Medical Imaging: 2001: Image Processing, PTS 1-3*, ser. Proceeding of Society of Photo-Optical Instrumentation Engineers (SPIE), Sonka, M and Hanson, KM, Ed., vol. 2, no. 27, 2001, pp. 1609–1620, Medical Imaging 2001 Conference, San Diego, CA, FEB 18-22, 2001.

[46] M. J. D. Powell, "An efficient method for finding the minimum of a function of several variables without calculating derivatives," *The Computer Journal*, vol. 7, no. 2, pp. 155 – 162, Jan. 1964.

[47] S. M. Smith, "Fast robust automated brain extraction," *Human Brain Mapping*, vol. 17, no. 3, pp. 143–155, 2002.

[48] M. Jenkinson, M. Pechaud, and S. Smith, "BET2: MR-based estimation of brain, skull and scalp surfaces," in *Eleventh annual meeting of the organization for human brain mapping*, 2005, pp. 12–16.

[49] M. Jenkinson, "Fast, automated, n-dimensional phase-unwrapping algorithm," *Magnetic resonance in medicine*, vol. 49, no. 1, pp. 193–197, 2003.

[50] J. De Wilde, J. Lunt, and K. Straughan, "Information in magnetic resonance images: evaluation of signal, noise and contrast," *Medical and Biological Engineering and Computing*, vol. 35, no. 3, p. 259–265, 1997.

[51] "MATLAB - the language of technical computing," 2009.

[52] T. Tasdizen, S. P. Awate, R. T. Whitaker, and N. L. Foster, "MRI tissue classification with neighborhood statistics: A nonparametric, entropy-minimizing approach," *Medical Image Computing and Computer-Assisted Intervention–MICCAI 2005*, p. 517–525, 2005.

[53] B. Johnston, M. S. Atkins, B. Mackiewich, and M. Anderson, "Segmentation of multiple sclerosis lesions in intensity corrected multispectral MRI," *Medical Imaging, IEEE Transactions on*, vol. 15, no. 2, p. 154–169, 1996.

[54] J. Ashburner and K. J. Friston, "Unified segmentation," *Neuroimage*, vol. 26, no. 3, p. 839–851, 2005.

[55] Y. Zhang, M. Brady, and S. Smith, "Segmentation of brain MR images through a hidden Markov random field model and the expectation-maximization algorithm," *Medical Imaging, IEEE Transactions on*, vol. 20, no. 1, p. 45–57, 2001.

[56] S. Ardekani and U. Sinha, "Geometric distortion correction of high-resolution 3 t diffusion tensor brain images," *Magnetic resonance in medicine*, vol. 54, no. 5, pp. 1163–1171, 2005.

[57] C. Studholme, D. L. Hill, and D. J. Hawkes, "An overlap invariant entropy measure of 3D medical image alignment," *Pattern recognition*, vol. 32, no. 1, p. 71–86, 1999.

[58] J. L. Rodgers and W. A. Nicewander, "Thirteen ways to look at the correlation coefficient," *The American Statistician*, vol. 42, no. 1, p. 59–66, 1988.

[59] A. Asuero, A. Sayago, and A. González, "The correlation coefficient: An overview," *Critical Reviews in Analytical Chemistry*, no. 36, pp. 41–59, 2006.

[60] M. Jenkinson, P. Bannister, M. Brady, and S. Smith, "Improved optimization for the robust and accurate linear registration and motion correction of brain images," *Neuroimage*, vol. 17, no. 2, pp. 825–841, 2002.

[61] M. Jenkinson and S. Smith, "A global optimization method for robust affine registration of brain images," *Medical image analysis*, vol. 5, no. 2, pp. 143–156, 2001.

[62] "FSL," http://www.fmrib.ox.ac.uk/fsl/, Mar. 2011. [Online]. Available: http://www.fmrib.ox.ac.uk/fsl/

[63] "BrainWeb: simulated brain database," http://mouldy.bic.mni.mcgill.ca/brainweb/, Mar. 2011. [Online]. Available: http://mouldy.bic.mni.mcgill.ca/brainweb/

[64] C. A. Cocosco, V. Kollokian, K. S. Remi, G. B. Pike, and A. C. Evans, "Brainweb: Online interface to a 3D MRI simulated brain database," in *NeuroImage*, 1997.

[65] D. L. Collins, A. P. Zijdenbos, V. Kollokian, J. G. Sled, N. J. Kabani, C. J. Holmes, and A. C. Evans, "Design and construction of a realistic digital brain phantom," *Medical Imaging, IEEE Transactions on*, vol. 17, no. 3, pp. 463–468, 1998.

[66] R. Kwan, A. Evans, and G. Pike, "An extensible MRI simulator for post-processing evaluation," in *Visualization in Biomedical Computing*, 1996, pp. 135–140.

[67] R. K. Kwan, A. C. Evans, and G. B. Pike, "MRI simulation-based evaluation of image-processing and classification methods," *Medical Imaging, IEEE Transactions on*, vol. 18, no. 11, pp. 1085–1097, 1999.

[68] D. W. McRobbie, *MRI from picture to proton*. Cambridge University Press, 2003.

Appendix A

Results and Optimization of Simulated Data

A.1 Registration Results in Simulated Data

Table A.1: Evaluation of Preliminary Results of Registration Methods in Simulated Data

	RMS		NMI		SCC		CM		Dice WM		Dice GM		Dice CSF		Sum of Rank	Time of Execution
	Value	Rank	Value	Rank	Value	Rank	Value	Rank	Value	Rank	Value	Rank	Value	Rank		
Reg1	13.7230	4	0.6045	7	0.7858	4	0.8438	9	0.7033	9	0.4798	3	0.5785	8	44	408639
Reg2	14.0640	11	0.6039	10	0.7760	11	0.7206	5	0.7084	5	0.4608	10	0.5825	7	59	1100889
Reg3	13.7330	5	0.6044	9	0.7851	5	0.7907	8	0.7051	8	0.4756	4	0.5832	6	45	2638904
Reg4	13.8550	8	0.6045	8	0.7819	8	0.7662	6	0.7096	3	0.4677	7	0.5850	5	45	3206067
Reg5	13.7350	6	0.6025	11	0.7842	6	0.9053	11	0.6962	12	0.4633	9	0.5689	10	65	311831
Reg6	12.4890	1	0.6082	1	0.8209	1	0.6939	3	0.7068	6	0.5326	1	0.5983	2	15	905654
Reg7	13.9220	10	0.6060	2	0.7813	9	0.9141	12	0.6973	10	0.4547	11	0.5637	12	66	153450
Reg8	13.6880	3	0.6051	4	0.7866	3	0.6787	2	0.7088	4	0.4696	5	0.5859	3	24	23835096
Reg9	13.9210	9	0.6050	5	0.7807	10	0.8877	10	0.6966	11	0.4667	8	0.5683	11	64	1179375
Reg10	13.8280	7	0.6046	6	0.7827	7	0.7697	7	0.7100	2	0.4692	6	0.5850	4	39	66057798
Reg11	13.0590	2	0.6056	3	0.8048	2	0.3970	1	0.7103	1	0.4919	2	0.5996	1	12	13905
Reg12	14.5520	12	0.6019	12	0.7623	12	0.7034	4	0.7051	7	0.4482	12	0.5779	9	68	5749660

Table A.2: Evaluation of Final Results of Registration Methods in Simulated Data

	RMS		NMI		SCC		CM		Dice WM		Dice GM		Dice CSF		Sum of Rank	Time of Execution
	Value	Rank	Value	Rank	Value	Rank	Value	Rank	Value	Rank	Value	Rank	Value	Rank		
Reg1	14.1760	9	0.6004	11	0.7714	10	0.7813	8	0.7062	7	0.4275	11	0.5734	8	64	109860
Reg2	14.0890	7	0.6038	7	0.7753	6	0.7248	5	0.7083	4	0.4599	6	0.5822	5	40	403839
Reg3	14.0820	6	0.6011	10	0.7744	7	0.7753	7	0.7066	6	0.4329	10	0.5733	9	55	799356
Reg4	13.8550	4	0.6046	6	0.7820	4	0.7476	6	0.7096	2	0.4702	4	0.5848	4	30	1053163
Reg5	14.1440	8	0.6002	12	0.7722	9	0.8023	10	0.7054	8	0.4245	12	0.5725	10	69	95575
Reg6	12.6080	1	0.6078	1	0.8175	1	0.7887	9	0.7080	5	0.5240	1	0.5997	1	19	354080
Reg7	14.2180	10	0.6053	3	0.7726	8	0.9094	12	0.6928	12	0.4435	9	0.5538	12	66	65126
Reg8	13.6160	3	0.6053	4	0.7887	3	0.6777	2	0.7095	3	0.4705	3	0.5872	3	21	9187671
Reg9	13.9830	5	0.6052	5	0.7792	5	0.8850	11	0.6973	11	0.4645	5	0.5687	11	53	391519
Reg10	14.5550	12	0.6019	9	0.7622	12	0.7038	4	0.7051	9	0.4482	8	0.5779	6	60	28564572
Reg11	13.0590	2	0.6056	2	0.8048	2	0.3970	1	0.7103	1	0.4919	2	0.5996	2	12	6996
Reg12	14.5520	11	0.6019	8	0.7623	11	0.7034	3	0.7051	9	0.4482	7	0.5779	7	56	2566386

A.2 Optimization Results of Registration Parameters in Simulated Data

Table A.3: Results of Optimization of Number of Bins in MI

	RMS		NMI		SCC		CM		Dice WM		Dice GM		Dice CSF		Time of Execution	
	Reg6	Reg11	Reg6	Reg11	Reg6	Reg11	Reg6	Reg11	Reg6	Reg11	Reg6	Reg11	Reg6	Reg11	Reg6	Reg11
25	12.6997	13.0593	0.6066	0.6056	0.8148	0.8048	0.6348	0.3970	0.7015	0.7103	0.5063	0.4919	0.5861	0.5996	885336	13906
50	12.4890	13.0593	0.6082	0.6056	0.8209	0.8048	0.6939	0.3970	0.7068	0.7103	0.53259	0.4919	0.59833	0.5996	905654	13905
75	12.5400	13.0593	0.6073	0.6056	0.8195	0.8048	0.6957	0.3970	0.7042	0.7103	0.5244	0.4919	0.4921	0.5996	1040661	13922
100	12.6510	13.0593	0.6065	0.6056	0.8162	0.8048	0.9384	0.3970	0.7108	0.7103	0.5260	0.4919	0.6056	0.5996	1213969	17851

Lighter colours = best results; Darker colours = worst results;

Table A.4: Results of Optimization of Number of Samples in MI

	RMS		NMI		SCC		CM		Dice WM		Dice GM		Dice CSF		Time of Execution	
	Reg6	Reg11	Reg6	Reg11	Reg6	Reg11	Reg6	Reg11	Reg6	Reg11	Reg6	Reg11	Reg6	Reg11	Reg6	Reg11
5	14.0565	13.0593	0.6005	0.6056	0.7741	0.8048	1.3040	0.3970	0.6926	0.7103	0.4202	0.4919	0.5649	0.5996	342004	3499
10	12.4920	13.0593	0.6085	0.6056	0.8208	0.8048	0.7205	0.3970	0.7074	0.7103	0.5333	0.4919	0.5996	0.5996	507952	6371
20	12.5500	13.0593	0.6075	0.6056	0.8191	0.8048	0.651	0.3970	0.7034	0.7103	0.5235	0.4919	0.5912	0.5996	851810	12036
30	12.5298	13.0593	0.6084	0.6056	0.8197	0.8048	0.7539	0.3970	0.7088	0.7103	0.5334	0.4919	0.6021	0.5996	1228141	17859
40	12.5250	13.0593	0.6085	0.6056	0.8198	0.8048	0.7499	0.3970	0.7090	0.7103	0.5339	0.4919	0.6023	0.5996	1527140	23595
50	12.5535	13.0593	0.6072	0.6056	0.8191	0.8048	0.6942	0.3970	0.7036	0.7103	0.5222	0.4919	0.5909	0.5996	1866567	30836

Lighter colours = best results; Darker colours = worst results;

Table A.5: Results of Optimization of Leaning Rate in GD Optimizer

	RMS		NMI		SCC		CM		Dice WM		Dice GM		Dice CSF		Time of Execution	
	Reg1	Reg6	Reg1	Reg6	Reg1	Reg6	Reg1	Reg6	Reg1	Reg6	Reg1	Reg6	Reg1	Reg6	Reg1	Reg6
0.000001	14.1471	14.5552	0.6003	0.6018	0.7722	0.7622	0.8024	0.7038	0.7052	0.7051	0.4276	0.4881	0.5715	0.578	430111	933993
0.00001	13.7227	14.5552	0.6045	0.6018	0.7858	0.7622	0.8438	0.7038	0.7033	0.7051	0.4798	0.4492	0.5785	0.5779	408639	933484
0.001	13.7227	14.5529	0.6045	0.6019	0.7857	0.7623	0.8438	0.7039	0.7033	0.7052	0.4798	0.4479	0.5785	0.578	436091	938699
0.1	15.6106	14.3384	0.5922	0.6031	0.7246	0.7683	0.8226	0.7136	0.6762	0.7062	0.3662	0.453	0.5283	0.5801	330717	1017327
1	26.0673	13.5272	0.5419	0.6056	0.3115	0.7911	0.7955	0.8941	0.4333	0.707	0.0489	0.4777	0.2656	0.5827	414016	970429
10		12.489		0.6082		0.82085		0.6939		0.7068		0.5326		0.5983		905654
100		12.6182		0.607		0.8172		0.6116		0.702		0.509		0.5874		1009796

Lighter colours = best results; Darker colours = worst results; Black = no result produced;

Table A.6: Results of Optimization of Number of Iterations in GD Optimizer

	RMS		NMI		SCC		CM		Dice WM		Dice GM		Dice CSF		Time of Execution	
	Reg1	Reg6	Reg1	Reg6	Reg1	Reg6	Reg1	Reg6	Reg1	Reg6	Reg1	Reg6	Reg1	Reg6	Reg1	Reg6
50	14.0675	13.6225	0.6031	0.6055	0.7755	0.7884	0.6982	0.8409	0.7059	0.7087	0.4531	0.478	0.5801	0.5844	23725	67602
75	13.0995	13.5263	0.6038	0.6056	0.7806	0.7911	0.7044	0.8929	0.7065	0.7071	0.4688	0.4772	0.5828	0.5828	37734	101813
100	13.8058	13.4234	0.6043	0.6059	0.7833	0.7941	0.723	0.873	0.7062	0.7077	0.4722	0.4833	0.5841	0.5845	46193	136509
200	13.6231	13.0774	0.6052	0.6073	0.7886	0.804	0.7783	0.8244	0.7057	0.7086	0.4791	0.5014	0.5835	0.5909	93110	265290
500	13.7223	12.5073	0.6045	0.6084	0.7858	0.8203	0.8435	0.7295	0.7034	0.708	0.478	0.5321	0.5786	0.6009	283626	625244
750	13.723	12.489	0.6045	0.6082	0.7858	0.8209	0.8438	0.6939	0.7033	0.7068	0.4798	0.5326	0.5785	0.5983	408639	905654
1000	13.7227	12.5151	0.6045	0.6076	0.7857	0.8202	0.8438	0.7039	0.7034	0.7053	0.4784	0.5266	0.5787	0.5946	568608	1233529
1250	13.7227	12.5666	0.6045	0.6073	0.7857	0.8186	0.8439	0.6421	0.7034	0.7028	0.4782	0.5193	0.5787	0.5898	578261	1615264
1500	13.7227	12.6297	0.6045	0.607	0.7857	0.8168	0.8439	0.6391	0.7034	0.7023	0.4779	0.5097	0.5785	0.5869	829860	1859241

Lighter colours = best results; Darker colours = worst results;

Table A.7: Results of Optimization of Step Length in Powell Optimizer

	RMS		NMI		SCC		CM		Dice WM		Dice GM		Dice CSF		Time of Execution	
	Reg8	Reg11	Reg8	Reg11	Reg8	Reg11	Reg8	Reg11	Reg8	Reg11	Reg8	Reg11	Reg8	Reg11	Reg8	Reg11
0.00001	13.8039	14.1471	0.6047	0.6003	0.7834	0.7722	0.7489	0.8072	0.7103	0.7048	0.4719	0.4266	0.5864	0.5709	3465030	3276
0.0001	13.6633	14.0613	0.6052	0.6010	0.7873	0.7749	0.6855	0.7634	0.7090	0.7075	0.4700	0.4323	0.5863	0.575	12263170	8608
0.001	13.6880	13.0590	0.6051	0.6056	0.7866	0.8048	0.6787	0.3970	0.7088	0.7103	0.4696	0.4919	0.5859	0.5996	23835096	13905
0.01	13.6843	13.7801	0.6050	0.6018	0.7867	0.7833	0.6774	0.7965	0.7088	0.7028	0.4703	0.4372	0.5858	0.5743	29411186	100084
0.1	13.6850	14.1702	0.6051	0.60008	0.7867	0.7715	0.6767	0.7596	0.7089	0.7010	0.4712	0.4221	0.5860	0.5706	37782113	17339

Lighter colours = best results; Darker colours = worst results;

Table A.8: Results of Optimization of Order of B-Spline in B-Spline Transform

	RMS		NMI		SCC		CM		Dice WM		Dice GM		Dice CSF		Time of Execution	
	Reg6	Reg8	Reg6	Reg8	Reg6	Reg8	Reg6	Reg8	Reg6	Reg8	Reg6	Reg8	Reg6	Reg8	Reg6	Reg8
2	12.5671	13.6884	0.6073	0.6051	0.8186	0.7866	0.6347	0.6775	0.7028	0.7089	0.5187	0.4701	0.5895	0.5858	12431312	64052733
3	12.4890	13.6880	0.6082	0.6051	0.8209	0.7866	0.6939	0.6787	0.7068	0.7088	0.5326	0.4696	0.5983	0.5859	905654	23835096
5	14.5552	14.5552	0.6018	0.6018	0.7622	0.7622	0.7038	0.7038	0.7050	0.7050	0.448	0.4480	0.5779	0.5779	15223157	10537287

Lighter colours = best results; Darker colours = worst results; Bold = best ranked parameter

Appendix B

Results of Real Data

B.1 Validation of Simulated Data

Table B.1: Evaluation of results in real data for validation of simulated data

	NMI		SCC		CM		Dice WM		Dice GM		Dice CSF		Sum of Rank	Time of Execution
	Value	Rank	Value	Rank	Value	Rank	Value	Rank	Value	Rank	Value	Rank		
Reg1	0.6184	8	0.4582	2	0.1460	2	0.5068	8	0.4701	7	0.2112	8	35	2757381
Reg2	0.6363	5	0.3549	7	2.8704	8	0.6203	5	0.5440	5	0.2509	6	36	9156340
Reg3	0.6184	7	0.4584	1	0.1478	3	0.5069	7	0.4699	9	0.2118	7	34	15240339
Reg4	0.6361	6	0.3600	6	2.9202	9	0.6229	4	0.5478	4	0.2515	5	34	19584661
Reg5	0.6184	9	0.4581	3	0.1436	1	0.5066	9	0.4700	8	0.2109	9	39	2499669
Reg6	0.6364	4	0.3497	9	2.8199	7	0.6194	6	0.5416	6	0.2621	4	36	7827233
Reg7	0.6426	1	0.3714	5	2.6385	4	0.6475	1	0.5656	1	0.2812	2	14	2029883
Reg8		10		10		10		10		10		10	60	*
Reg9	0.6411	2	0.3856	4	2.7024	5	0.6328	2	0.5513	3	0.3276	1	17	10554118
Reg10		10		10		10		10		10		10	60	*
Reg11	0.6382	3	0.3528	8	2.7316	6	0.6323	3	0.5534	2	0.2640	3	25	1853831
Reg12		10		10		10		10		10		10	60	*

Result at black, represents an unfinished combination

* Possible time is higher than 8 hours

B.2 Methods Evaluation

Table B.2: Results of real data for b=0

	NMI		SCC		CM		Sum of Rank
	Value	Rank	Value	Rank	Value	Rank	
Distorted	0.6279	6	0.3153	6	3.7212	5	17
Reg7	0.6426	2	0.3714	2	2.6385	1	5
Reg11	0.6382	4	0.3528	4	2.7316	3	11
Field Map	0.6280	5	0.3155	5	3.7219	6	16
Pipeline - Reg7	0.6426	1	0.3715	1	2.6399	2	4
Pipeline - Reg11	0.6383	3	0.3529	3	2.7329	4	10

B.3 *b*-value Evaluation

Table B.3: Mean values of NMI for different b-values

b	0			1000			4000			8000		
	Mean	STDEV	Improvement	Mean	STDEV	Improvement	Mean	STDEV	Improvement	Mean	STDEV	Improvement
Distorted	0.6279	0		0.6230	0.0012		0.6124	0.0032		0.5019	0.0007	
Reg6	0.6426	0	0.0234	0.6356	0.0015	0.0202	0.6285	0.0025	0.0262	0.5189	0.0073	0.0338
Reg11	0.6382	0	0.0164	0.6322	0.0021	0.0147	0.6284	0.0025	0.0260	0.5183	0.0076	0.0327
Field Map	0.6280	0	0.0001	0.6276	0.0016	0.0074	0.6151	0.0032	0.0044	0.5024	0.0010	0.0010
Pipeline - Reg6	0.6426	0	0.0235	0.6356	0.0015	0.0203	0.6285	0.0025	0.0263	0.5189	0.0073	0.0338
Pipeline - Reg11	0.6383	0	0.0165	0.6322	0.0021	0.0148	0.6284	0.0025	0.0261	0.5183	0.0076	0.0327

Table B.4: Mean values of SCC for different *b*-values

b	0			1000			4000			8000		
	Mean	STDEV	Improvement	Mean	STDEV	Improvement	Mean	STDEV	Improvement	Mean	STDEV	Improvement
Distorted	0.3153	0		0.6125	0.0119		0.6705	0.0361		0.0167	0.0076	
Reg6	0.3714	0	0.1782	0.6723	0.0112	0.0977	0.7659	0.0318	0.1424	0.1789	0.0161	9.735
Reg11	0.3528	0	0.1192	0.6584	0.0124	0.0750	0.7657	0.0297	0.1419	0.1639	0.0157	8.8397
Field Map	0.3155	0	0.0007	0.6248	0.0125	0.0202	0.6935	0.0351	0.0344	0.0200	0.0087	0.1986
Pipeline - Reg6	0.3715	0	0.1784	0.6724	0.0112	0.0979	0.7661	0.0318	0.1426	0.1789	0.0161	9.7374
Pipeline - Reg11	0.3529	0	0.1194	0.6585	0.0124	0.0752	0.7658	0.0297	0.1422	0.1640	0.0157	8.8433

Table B.5: Mean values of Euclidean Distance CM for different *b*-values

b	0			1000			4000			8000		
	Mean	STDEV	Improvement	Mean	STDEV	Improvement	Mean	STDEV	Improvement	Mean	STDEV	Improvement
Distorted	3.7212	0		2.9155	0.2880		2.9248	0.5915		12.7753	0.0870	
Reg6	2.6385	0	0.2910	1.5160	0.2096	0.4800	0.8385	0.2582	0.7133	11.5654	2.3216	0.0947
Reg11	2.7316	0	0.2659	1.5947	0.2662	0.4530	0.8313	0.3063	0.7158	10.3831	3.1432	0.1872
Field Map	3.7219	0	-0.0002	3.0072	0.2812	-0.0315	2.9129	0.6147	0.0041	12.6657	0.0884	0.0086
Pipeline - Reg6	2.6399	0	0.2906	1.5178	0.2095	0.4794	0.8395	0.2594	0.7130	11.5647	2.3215	0.0948
Pipeline - Reg11	2.7329	0	0.2656	1.5964	0.2662	0.4524	0.8323	0.3076	0.7154	10.3827	3.1433	0.1873

Appendix C

FMRIB Software Library (FSL) Guide

FSL [38, 39] is a library of tools created by FMRIB Analysis Group, Oxford, UK for analysis of MRI, fMRI and DW-MRI data. This appendix wants to explain the principal applications of FSL used in this thesis.

In the following guide the commands that appear between angle brackets '< >' are obligatory and the ones that appear between brackets '[ ]' are optional.

C.1 Brain Extraction Tool (BET)

BET [47] receives a head image and returns just the brain, removing all the non-brain parts. A new BET version was developed, BET2 [48]. It has more accurate results and comes with the tool BETSURF that is capable of estimating the inner and outer skull surfaces and the outer scalp surface with a high-resolution T1 and T2 images. BET2 has the same options as BET and more, because of that it will be used only BET2. The basic command to use BET2 is:

```
bet2 <input volume> <output volume> [options]
```

The default options of BET2 usually are enough to execute the brain extraction, but in some difficult cases it is necessary to modify some of the default values. In the table C.1 are described the principal options that can be modified and some optional functions that could be useful in BET2. This tool has Graphical User Interface (GUI) application with the same options of the Command-Line Interface (CLI).

Image C.1 is an example of a BET application in a T1-weighted MRI. Where C.1a is the original image and C.1b is the result of brain extraction.

Table C.1: Options of BET2 tool from FSL

Optional Command	Function	Default Value
-m	Generates a binary brain mask	N/A
-f <frac>	Fractional intensity threshold [0;1]. With smaller values a larger brain outline is estimate.	0,5
-g <grad>	Vertical gradient in fractional intensity threshold [-1;1]. Positive values give a larger brain outline at the bottom.	0
-r <rad>	Head radius in mm	N/A
-c <x y z>	Center-of-gravity of the head in voxels	N/A

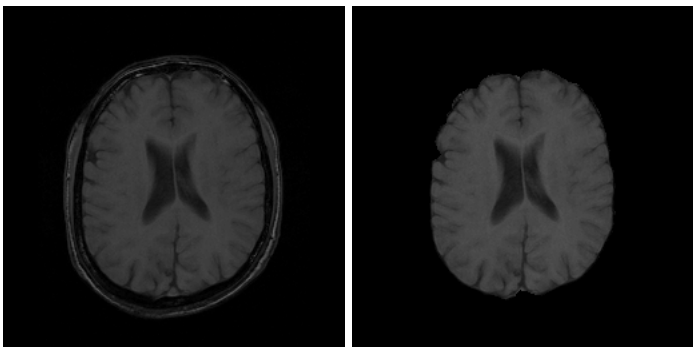

(a) Original Image **(b)** Result Image

Figure C.1: Brain Extraction Example with BET2

C.2 FMRIB's Linear/Nonlinear Image Registration Tool (FLIRT/FNIRT)

These tools [60, 61] are used to register two images, this means that place different images in the same space. To perform a registration is important that the source image has more resolution that the reference image for not appearing errors in the process, which is not always possible.

These two tools have the difference that FLIRT can just do linear transformations between the source and the target images while FNIRT can only do nonlinear transformations. To use FNIRT it is needed to first run the FLIRT to a robust transformation.

FLIRT has four components that are very important in registration that are the Cost Function Weighting, the Degrees of Freedom (DOF), the Interpolation Method and the Cost Functions. The Cost Function Weighting is used when it is wanted that some parts of the source and reference images have more or less importance in the registration. The DOF are important to configure the type of transformation, being that more DOF corresponds to more types of transformations (rotation, scaling, shearing...) but it is not always better, that is the case of intra-subject registration where a minor DOF is better. The Interpolation Methods are important to understand how the image voxels are filled with some value and the FLIRT gives some interpolation alternatives, such as Nearest Neighbour, Trilinear, Sinc, Spline and k-Space Methods. Finally the Cost Functions are the component that measure the quality of the alignment and are provided some functions with FLIRT such as Least Squares, Normalized Correlation, Correlation Ratio, MI and NMI that must

be chosen depending on the type of images.

In FLIRT many options of the registration need to be inputted to have better results, the most important are showed in the table C.2 and the structure of the CLI for this tool is one of the next three, considering:

- If it will be done a normal registration and receive an output image;

```
flirt [options] -in <input volume> -ref <reference volume> -out
    <output volume>
```

- If it will be done a registration but the output is the mask of the transformation;

```
flirt [options] -in <input volume> -ref <reference volume> -omat
    <output matrix>
```

- Or if we already have a mask and want to do a registration from this mask.

```
flirt [options] -in <input volume> -ref <reference volume>
    -applyxfm -init <matrix> -out <output volume>
```

In the case of using a matrix to apply a transformation it is also needed to input the reference image to establish the resolution of the output image.

Table C.2: Options of FLIRT tool from FSL

Optional Command	Function	Default Value
-omat <matrix file>	Generates a 4x4 mask that can be applied in other image.	N/A
-cost < >	Define the cost function from one of the options mutualinfo, corratio, normcorr, normmi, leastsq, labeldiff	corratio
-interp < >	Define the interpolation to use from one of the options trilinear, nearestneighbour, sinc	Trilinear
-dof < >	Number of degrees of freedom	12
-refweight <volume>	Use weights for reference volume	N/A
-inweight <volume>	Use weights for input volume	N/A
-2D	Use 2D rigid body mode and ignores DOF	N/A

In image C.2 is an example of a brain registration from a T2-weighted MRI (image C.2a) to a T1-weighted MRI (image C.2b) with the result on image C.2c.

In the other hand, FNIRT is a much more powerful and complex tool. It is important to say that FNIRT is more sensitive to errors in brain extraction than FLIRT so the BET result must be very good. The CLI of the FNIRT is the following:

```
fnirt --in=<input volume> --ref=<reference volume>
    [--config=<configuration file>] [options]
```

As showed on the CLI, FNIRT gives the opportunity to create a configuration file (`*.cnf`) with all the parameters to the registration. This file must have a parameter by line and must be in the same format as it was in CLI. Responsible from FMRIB advise to use the configuration files provided

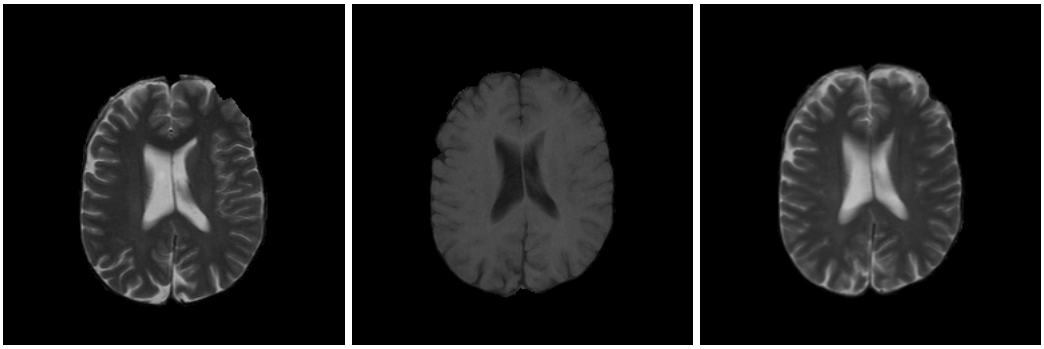

(a) Original Image **(b)** Reference Image **(c)** Registered Image

Figure C.2: Brain Registration Example with FLIRT

by them with FNIRT and make small alterations depending the job in cause. It is also important to say that if a parameter is in the configuration file and in the CLI, the second has precedence over the configuration file. So it advisable that use the FMRIB configuration files and make the alterations in the CLI.

The options that are available in FNIRT are an extended list and are available in the FNIRT page of FSL website [62].

C.3 Phase Region Expanding Labeller for Unwrapping Discrete Estimates (PRELUDE)

PRELUDE [49] is a tool that unwraps a phase map and can be used by CLI in one of the two ways:

```
prelude -c <raw phase> -o <unwrapped phase> [options]

prelude -p <phase volume> -a <abs volume> -o <unwrapped phase>
    [options]
```

The first receive a phase map with complex data (phase and magnitude together) while the second method receives phase and magnitude inputs separated. The two methods have as output the unwrapped phase map.

The most important options that can be used in PRELUDE are described in table C.3.

Table C.3: Options of PRELUDE tool from FSL

Optional Command	Function
-f,–force3D	Forces all processing to be full 3D.
-m	Uses the user-defined mask such as a BET mask.

C.4 FMRIB's Utility for Geometrically Unwarping EPI's (FUGUE)

FUGUE is a tool to correct images from EPI sequences in which its distortion has been caused by magnetic field inhomogeneities. This method needs a field map that measures the inhomogeneities, an EPI data set to correct and some parameters from the acquisition. This tool can be performed in CLI or in GUI of FEAT (FMRI Expert Analysis Tool).

FUGUE has two possible execution methods:

```
fugue -i <epi> -p <unwrapped phase> --dwell=<dwell to asym ratio> -u
   <result> [options]

fugue -i <epi> --loadfmap=<field map> --dwell=<dwell to asym ratio>
   --unwarpdir=<unwarpping direction> -u <output>

fugue -i <unwarped image> -p <unwrapped phase> --dwell=<dwell to asym
   ratio> -w <epi like result> [options]
```

The first and second are used to correct an EPI data set due the field inhomogeneities, where `--dwell` corresponds to echo spacing (sec) in the EPI. The `--unwarpdir` is the direction of warping of the phase images and usually it is the phase encoding direction. This parameter can be defined as x, y, z, x-, y- and z- whereas the default value is y. In the first it uses the unwrapped phase image as input to correct the EPI, while on second case it is used the field map, that comes from the unwrapped phase map, as will be explained the section C.5. The last one is used to create a distorted image from an undistorted using the field map. The image created can be used for a registration target for the EPI distorted data. The field map used must be in rad/sec.

There are some options that can be useful to regularize the field map, such as:

- *-s* <*sigma*> - 2D Gaussian smoothing
- *–smooth3*=<*sigma*> - 3D Gaussian smoothing
- *-m* - 2D median filtering
- *–poly*=<*n*> - 3D polynomial fitting of degree *n*
- *–fourier*=<*n*> - 3D sinusoidal fitting of degree *n*

C.5 Procedures to Undistort EPI images with Unwrapping Method using FSL tools

EPI suffers from geometric distortion due the field inhomogeneities especially in high-field MR scanners (3T or more) [38]. A way to correct these distortions is with the help of a Field Map.

To achieve that goal, FSL has a series of tools described above to correct the distortion, such as PRELUDE(section C.3) and FUGUE(section C.4). This set of tools can also be found in FEAT from FSL library.

The first procedure to be done is to obtain a magnitude field map that could come directly from the exam data or in a complex image and in this case the command that needs to be applied is:

```
fslcomplex -realabs <complex data> <fieldmap abs>
```

Again, if the field map comes in a complex data, the following commands must be executed to obtain the two phase maps with the different echo times in radians:

```
fslcomplex -realphase <complex data> <fieldmap phase0 rad> 0 1
fslcomplex -realphase <complex data> <fieldmap phase1 rad> 1 1
```

However if the phase comes separately from the magnitude field map is important to verify if the resolution is the same for phase and magnitude, to do that use `fslinfo`.

```
fslinfo <MRI>
```

If they have not the same resolution it must be performed a resampling or a registration using FLIRT. By example if the magnitude image as a high resolution should be applied the following command:

```
flirt -in <fieldmap phase> -ref <fieldmap abs> -out <fieldmap phase
    high resolution>
```

Usually when the phase maps come separated, they come in integer that represents the radians (see `fslinfo` to know what type of data is in the image). It is important to transform it into the real radian scale, to do that execute the following commands:

```
fslmaths orig_phase0 -mul 3.14159 -div 2048 phase0_rad -odt float
fslmaths orig_phase1 -mul 3.14159 -div 2048 phase1_rad -odt float
```

It is important to say that the value 2048 could be incorrect and probably must be adjust for each different site/scanner/sequence to be correct for the maximum value. If the result does not have a range of approximately 0 to 6.28 the scale must be corrected.

The next step is to unwrap the two phase maps using PRELUDE by the next form:

```
prelude -a <fieldmap abs> -p <fieldmap phase0 rad> -o <fieldmap phase0
    rad unwrapped rad>
prelude -a <fieldmap abs> -p <fieldmap phase1 rad> -o <fieldmap phase1
    rad unwrapped rad>
```

After unwrapping the phase field maps are important to calculate the field map in rad/sec. If you have two phase maps in radians, do the following command where TE is the difference between the echo times:

```
fslmaths <phase1 unwrapped rad> -sub <phase0 unwrapped rad> -mul 1000
    -div <TE> <fieldmap rads>
```

However, it is possible that the data from the exam comes with only one phase field map which consists in the already subtracted phase maps with different TE. In these cases it is also necessary to convert them in radians by the next script:

```
fslmaths orig_phase -mul 3.14159 -div 2048 phase_rad -odt float
```

After that the unwrap process must be done with PRELUDE like in the first case but just for one image and after that the phase map must be converted to rad/s with `fslmaths` by the next way:

```
fslmaths phase_unwarp -mul 1000 -div <TE> fieldmap_rads -odt float
```

In some cases the field map must be regularized due to some noise or contamination around the edges of the brain. To correct it is used the regularization functions from FUGUE (see appendix C.4).

From this point it is possible to correct the EPI distortion by two ways: with the FEAT GUI and with the FUGUE CLI that will be explained below.

About FEAT GUI it is important to say that it is a tool to analyze fMRI activation but in this case it will only be used the pre-stats tools that run FUGUE. To choose just the 'Pre-stats' option press the option in the right combo-box at the top as showed on image C.3a. After that, in the 'Data' tab (image C.3b) choose the EPI data clicking in 'Select 4D data' and the 'Output directory' on the appropriate space. In the 'Pre-stats' tab (image C.3c) choose the field map and magnitude field map as the information about the acquisition in the 'B0 unwrapping' frame. Finally press 'Go' and the browser will open with the log of the process and the results that also are in the chosen directory.

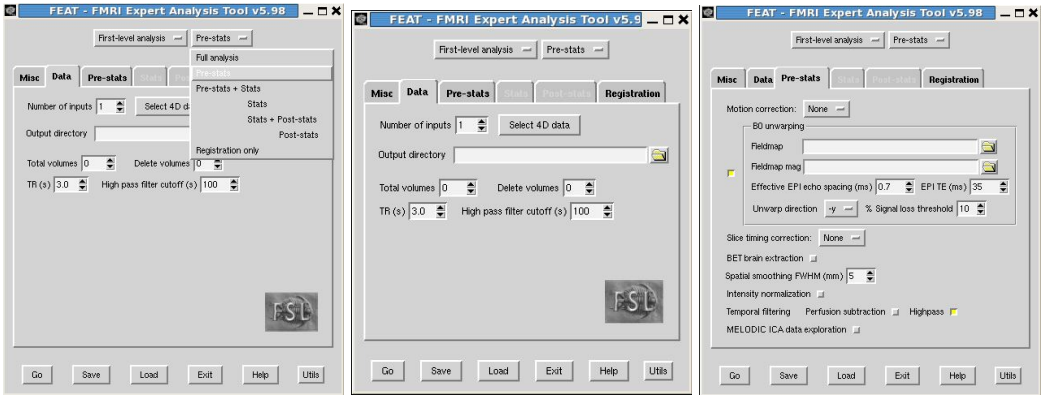

(a) **(b)** **(c)**

Figure C.3: FEAT GUI

The FUGUE CLI consists in running the following script:

```
fugue -i <EPI> --loadfmap=<field map> --dwell=<echo spacing>
   --unwarpdir=<unwarpping direction> -u <output>
```

In FUGUE CLI it is not necessary to input the magnitude field map and the signal loss threshold such as in FEAT GUI, but this probably is because the GUI has some parameters that are not only for correction and FUGUE only does the distortion correction process.

All these procedures can be summarized in the flowchart from image C.4

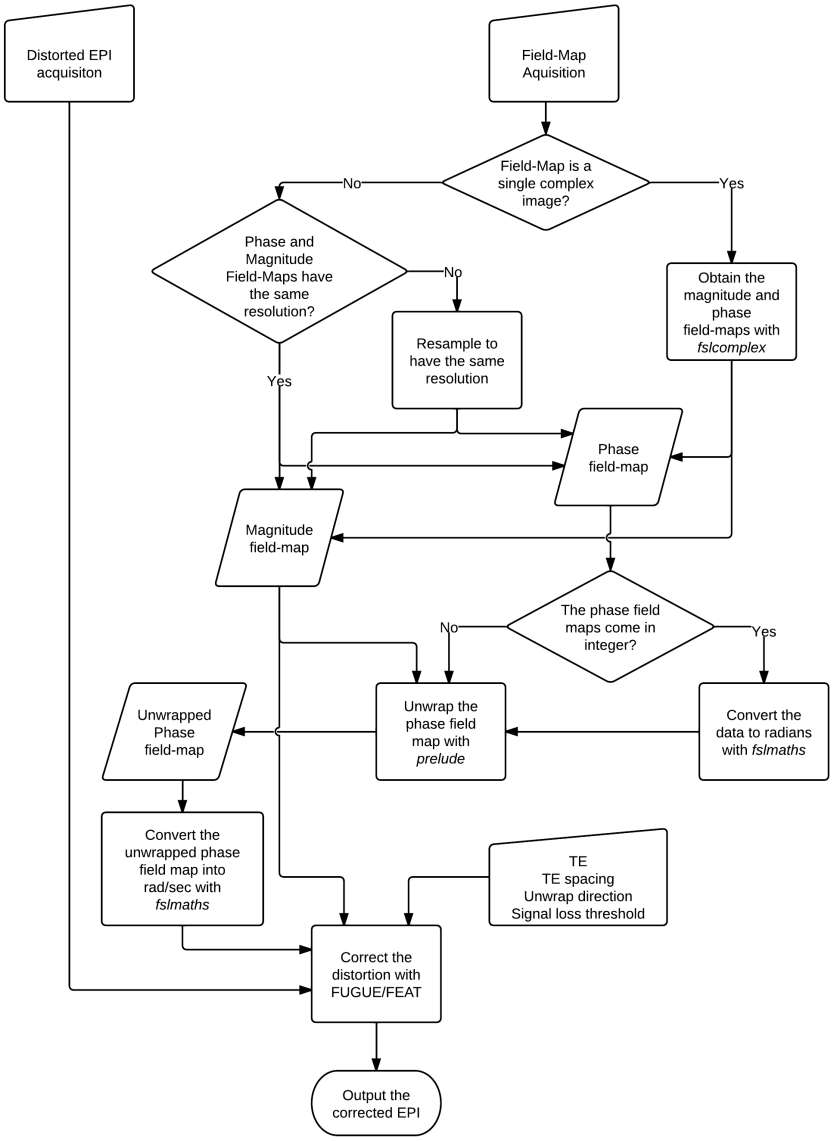

Figure C.4: Procedure to a Field Map Correction

Image C.5 has an example of the correction process. C.5d is the original EPI image. In C.5a is the magnitude field map necessary to unwrap the phase field map (image C.5b, that in this case came together the two phase maps) getting the result of the image C.5c. Finally the image C.5e is the result of the EPI correction and the image C.5f is the difference between the two EPI's (distorted and undistorted).

C.6 Physics-Oriented Simulated Scanner for Understanding MRI (POSSUM)

With POSSUM [40, 41] is possible to simulate MRI and fMRI images, and this tool has several parts such as sequence generation, signal generation, noise generation and image reconstruction.

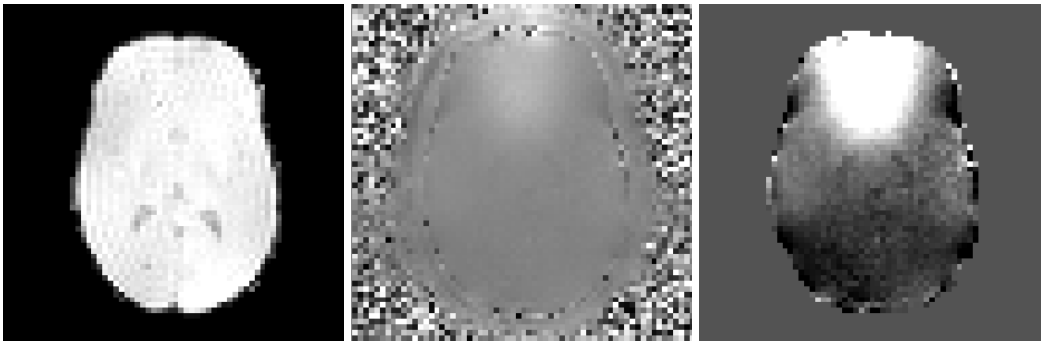

(a) Magnitude Field Map **(b)** Wrapped Phase Field Map **(c)** Unwrapped Phase Field Map

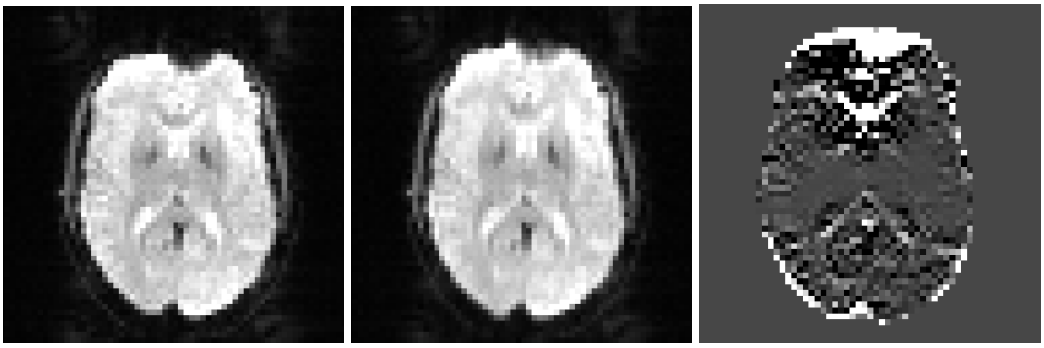

(d) Distorted EPI **(e)** Undistorted EPI **(f)** EPI difference

Figure C.5: Example of a EPI correction with Field Map

There are several inputs that could be entered in POSSUM such as the object model, the MR parameters, the pulse sequence, the slice profile, the motion, the B0 inhomogeneities and the activation, but in this project it will not be concerned the motion and activation.

An object should be placed as a model to create the MRI, in this case will be used a model provided by BrainWeb [63–67]. The MR parameters are related with the tissue and are characteristics such as relaxation times, spin density and chemical shift value which are already described in a POSSUM file and it will be used without any changes and the values are showed on table C.4.

Table C.4: Tissue's Characteristics

Tissue Type	T1(s)	T2*(s)	ρ	Δ_{CS} (ppm)
Gray Tissue	1331e-03	51e-03	0.86	0
White Tissue	832e-03	44e-03	0.77	0
CSF	3700e-03	500e-03	1	0

It is important to say the model image must be a segmented image where each volume corresponds to a different tissue and the volumes must be in the same order and number that the tissues described in the MR parameters file (see table reftab:tissue). For this exists some tools described in section C.8 such as *fslsplit* and *fslmerge* that can be use in an image from BrainWeb [63–67]. Other way is segmented a T1 structural image and merge them the various segments in a single image with *fslmerge*.

The pulse sequence can also be programmed using the tool PULSE which gives the chance of

choosing between an EPI and a GRE sequence. The general use of this tool is showed next:

```
pulse -i <object> -o <pulse> [options]
```

Where the object is the model described above and pulse is the output file with all the parameters of the sequence. The main options to choose in this tool are described on the table C.5

Table C.5: Options of PULSE tool from FSL

Optinal Command	Function	Default Value
–seq	epi, ge OR none	epi
–angle	Flip angle in degrees	90
–te	Echo time TE	0.03 s
–tr	Repetition time TR	3 s
–trslc	The time that takes for the acquisition of one slice	0.12 s
–nx	Resolution in x of the output image	64
–ny	Resolution in y of the output image	64
–dx	Image voxel x-dimension	0.004 m
–dy	Image voxel y-dimension	0.004 m
–maxG	Maximum gradient strength	0.055 T/m
–riset	Time it takes for the gradient to reach its max value	0.00022 s
–bw	Receiving bandwidth	100000 Hz
–numvol	Number of volumes	1
–numslc	Number of slices	1
–slcthk	Slice thickness	0.006 m
–gap	Gap between the slices in m	0 m
–zstart	The lowest position in the slice direction in m	0 m
–slcdir	x+, x-, y+, y- or z+ or z- slice direction/orientation	z-
–phasedir	x, y, or z phase encode direction	y
–readdir	x, y, or z read encode direction	x
k,–kcoord	saving k-space coordinates	no

The slice profile is a matrix that describes the RF pulse and once again POSSUM comes with a standard profile that will be used in this project.

Finally POSSUM gives the opportunity to simulate MRI with B0 field inhomogeneities. Once again POSSUM comes with a generic B0 inhomogeneity field for the standard object in *ppm*.

But it is also possible to create other inhomogeneity field if other object will be used, for that are two ways of doing that. The first consists in having a good 3D tissue/air segmentation image, where tissue value must be 1 and air must be 0, and run the following command where the output comes for a field of 1T:

```
b0_calc -i <tissue air segmentation> -o <b0>
```

Where `<tissue air segmentation>` is the 3D tissue/air segmentation image and `<b0>` is the b0 output file that come in *T*. But for other fields it is only needed to multiply the field given by the desired field strength. For example if we have a scanner with 3T the following command must be performed:

```
fslmaths <b0 inhomogeneity field 1T> -mul 3 <b0 inhomogeneity field 3T>
```

It is also possible to convert the Tesla b0 field in units of *ppm*, for that it is only need to run `fslmaths` to perform the equation (C.1) that describe the relationship between the variance in the b0 field (variation) with the corresponding measure in *ppm* [68].

$$Inhomogeneity(ppm) = \frac{Variation(T)}{Magnetic\ Field\ Strength(T)} * 10^6 \tag{C.1}$$

With the b0 inhomogeneities in units of *ppm* it is not need to convert them for different fields strengths, because in this case the measure is for all the field strengths.

The other way to generate a b0 inhomogeneity field is with a structural image and a field map, applying the following command line:

```
generate_b0 <structural> <field_map> <TE difference>
```

The output inhomogeneity map file will have the name '`<field_map>_possum`'.

After defining all these parameters it is possible to run the POSSUM by the execution of the following command:

```
possum -i <phantom volume> -x <MR parameters matrix> -p <pulse> -f <RF
    slice profile> -b <b0 inhomogeneity> -o <output signal matrix>
    [options]
```

There are some optional parameters in POSSUM but they are not important for this project.

POSSUM also has tools to add noise to the simulated data, for that use the command line on the output file `signal_nonoise` in the output directory:

```
systemnoise [options] -in=<signal without noise> -out=<signal with
    noise> --sigma=<value>
```

Where *sigma* is the standard deviation of the white noise. And after that, transform the obtained signal in an MRI image using the following script:

```
signal2image [options] -i <signal> -p <pulse> -o <image>
```

With this tool is then possible to generate MR images with or without spatial distortion due the B0 inhomogeneities.

C.7 FMRIB's Automated Segmentation Tool Brain Segmentation and Bias Field Correction (FAST)

FAST [55] is a FSL tool that performs segmentation over a MRI data. This tool has GUI and CLI but it is only be explained the second. The structure of CLI is the following:

```
fast [options] <file(s)>
```

FAST permits one input or a multi-channel input, performing the segmentation considering the series of images inputted. If only one image is given, FAST has the possibility to choose the kind of image inserted (T1, T2 or DP) to consider the weights of the tissues in the segmentation. FAST also gives the opportunity of segment the image in many classes as it is wanted. The main options of FAST are described on table C.6.

Table C.6: Options of FAST tool of FSL

Optinal Command	Function	Default Value
-S <n>, –channels=<n>	Number of image channels	1
t <n>, –type=<n>	Type of image (n=1 for T1, n=2 for T2, n=3 for PD)	1
-o <base>, –out=<base>	Base name of the output files	N/A
-n <n>, –class=<n>	Number of tissue-type classes	3
-s <file>, –manualseg=<file>	Input a file specifying initial tissue-type means	N/A

FAST also gives the opportunity of correction of bias field inhomogeneity, which will not be explained in this guide due it is not used in this project.

The are various possible outputs in FAST, as listed above:

Partial Volume Maps An image per class with a range of [0-1] representing the probability of the voxel in the correspondent class. A voxel can be in various classes.

Binary Segmentation: Single Image An image with a different intensity per class. This is, class 1 has the value 1, class 2 has the value 2, and so on. Each voxel is only in one class.

Binary Segmentation: One image per class The same information as on the previous output, but each different class is on a different image. Each image has the value 1 on voxels that belongs to the class and 0 in the rest of the image.

As an example it was performed a segmentation of a structural MRI into 3 classes, and the results as showed of figure C.6. Where C.6a are the original data and C.6b are the results of the 3 classes segmented.

C.8 Other tools of FSL

A series of other tools are available in FSL to help manipulating MR images. This section will described some of the more important to the current project.

C.8.1 fslinfo

This tool has the main characteristic of providing the basic information of an image, such as the resolution, dimension of the voxels of the MRI, the format of the image (NifTI,DICOM,...) and the data format of the voxels. The command line to execute this tool is:

```
fslinfo <filename>
```

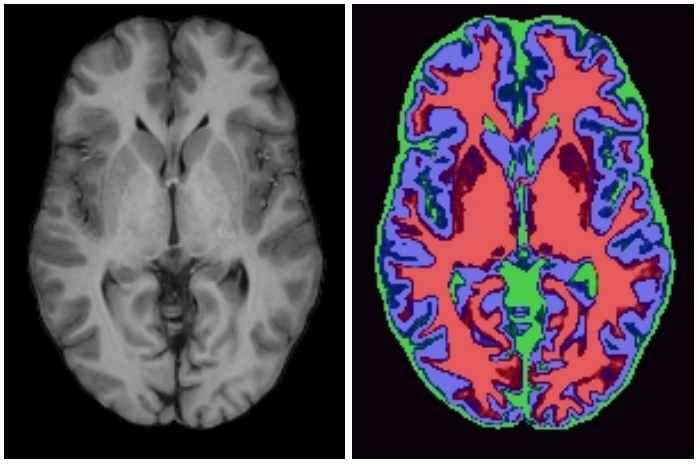

(a) Structural Image **(b)** Segmented Image

Figure C.6: Segmentation Example with FAST

C.8.2 fslswapdim

With `fslswapdim` it is possible to change the orientation of the image, in other words, permits to change the coordinate x with the z or other combinations according to the following CLI structure:

```
fslswapdim <input> <a> <b> <c> [output]
```

Where `a`, `b` and `c` represent the final *x*, *y* and *z* axis and they can take the values, `-x`, `x`, `-y`, `y`, `-z`, and `z`. If no output is defined the changes will be performed in the input file. This is an important tool because different sequences can have different orientations.

C.8.3 fslsplit

This tool consists in split a 4D volume in as many 3D volumes as the extension of 4^{th} dimension that can be *x*, *y*, *z* and *time* (by default). The command line of this tools is:

```
fslsplit <input> [output_basename] [-t/-x/-y/-z]
```

C.8.4 fslmerge

Unlike the previous tool, this as the function to concatenate a series of `n` equal dimensions MRI, in just one. For example a series of 3D images, obtaining a 4D image. This tools has the capability to concatenate images time, *x*, *y* and *z* directions and have yet an option (`-a`) to choose the appropriate concatenating option. The command line to use this tools is the following:

```
fslmerge <-t/-x/-y/-z/-a> <output file> <input1 input2 ... inputN>
```

C.8.5 fslmaths

This tool have the capability to perform a series of mathematical operations over a MRI or under several MRI's. It can provide since the basic operation's to some filtering functions. And it is important to say that with this tool is possible to choose the type of data that comes in the output, such as float, integer or double. The main command line of this tools is:

```
fslmaths [-dt <input data type>] <first input> [operations and inputs]
    <output> [-odt <output data type]
```

To better know the list of possibilities of this tool, it is advisable to visit the FSL website [62] or see the help of these tools in FSL software typing `fslmaths` in the CLI

C.8.6 fslcomplex

This tools permits to perform some complex calculus over MRI volumes. The main CLI structure is the following:

```
fslcomplex <output type> <input> <output> [start volume [end volume]]
```

`fslcomplex` has some functions as obtaining the real or imaginary part of a complex data or calculate the complex data from the real and imaginary data. For more information write `fslcomplex` in CLI and see the several options to perform this tool.

Appendix D

Paper for 4th International Symposium on Applied Sciences in Biomedical and Communication Technologies (ISABEL)

Pipeline for Spatial Distortion Correction in MRI *

Pedro Mendes
Siemens SA
Healthcare Sector
Porto, Portugal
Faculty of Sciences and Technologies
University Nova of Lisbon
Caparica, Portugal
mendes.pmt@gmail.com

Liliana Caldeira
Siemens SA
Healthcare Sector
Porto, Portugal
University of Lisbon
Faculty of Sciences
Institute of Biomedical Engineering and Biophysics
Lisbon, Portugal
liliana.caldeira@siemens.com

Filipe Janela
Siemens SA
Healthcare Sector
Porto, Portugal
Filipe.janela@siemens.com

Nicolas F. Lori
Institute of Biomedical Research in Light and Image
Faculty of Medicine
University of Coimbra
Brain Imaging Network
Coimbra, Portugal
nflori@fmed.uc.pt

Mário forjaz Secca
Faculty of sciences and Techonologies
University Nova of Lisbon
Caparica, Portugal
mfs@fct.unl.pt

ABSTRACT

The recent advances in Magnetic Resonance Imaging gradient, regarding strength and computation speed, led to the development of Echo-Planar Imaging pulse-sequences with faster acquisition times. This kind of sequence is used in functional MRI and diffusion-weighted Magnetic Resonance Imaging and it presents more distortions than slower sequences. This work aims to compare different spatial distortion correction methods for Echo-Planar Imaging sequences with a new proposed pipeline which consists in performing a Field Map correction after a registration process.

Categories and Subject Descriptors

J.3 [**Computer Applications**]: Life and Medical Sciences

General Terms

Algorithms

Keywords

Distortion Correction, Field Map, Magnetic Resonance, Registration, Spatial Distortion.

*Financial support of FCT projects *Ciência 2007* and *PTDC/SAU-BEB/100147/2008*

ISABEL '11, October 26-29, Barcelona, Spain

1. INTRODUCTION

The growth of Magnetic Resonance Imaging (MRI) led to the development of new hardware with higher magnetic fields and faster sequences, improving spatial and temporal resolution. However, these improvements result in intensity and spatial distortions that limit MRI quality, especially in faster sequences, such as Echo-Planar Imaging (EPI), which is used in functional MRI (fMRI) and diffusion-weighted MRI (DW-MRI). Particularly, spatial distortions must be corrected to obtain a more reliable similarity to structural images.

In this paper, we will explore two methods of spatial distortion correction, namely Registration [5] and Field Map Correction [4, 1, 3]. These methods were chosen because they are the most used in the literature. After setting the best registration method for the data in concern, we performed a pipeline which runs the Field Map correction on the best registered image.

1.1 Registration

Registration is a method that consists in aligning two images [5]: a *source image* A with a *reference image* B. In the case of spatial distortion correction, the *source image* presents distortion and the *reference image* presents no distortion. However, this is not completely true, since the second image might present distortions as well. This technique is used in fMRI and DW-MRI, when it is necessary to align a series of images.

The registration process can be divided into four components: the *transformation model*, the *interpolator*, the *similarity metric* and the *optimizer*. These four components are applied to obtain the arguments arg of transformation $T()$ that maximize the metric M, presented in equation (1) [6].

$$arg\max M(A, T(B)) \quad (1)$$

Table 1: Combination of components for registration correction

ID	Metric	Optimizer	Interpolator	Transform
Reg1	MI[1]	GD[2]	Linear	Affine
Reg2				B-Spline
Reg3			B-Spline	Affine
Reg4				B-Spline
Reg5			Nearest Neighbor	Affine
Reg6				B-Spline
Reg7		Powell	Linear	Affine
Reg8				B-Spline
Reg9			B-Spline	Affine
Reg10				B-Spline
Reg11			Nearest Neighbor	Affine
Reg12				B-Spline

MI - Mutual Information; GD - Gradient Descent; NN - Nearest Neigbor

1.2 Field Map Correction

The principal cause of distortion in EPI images are magnetic field inhomogeneities causing a pixel shift in the phase encoding direction and, therefore, a spatial distortion. An approach to correct this problem is based on the acquisition of a field map after the EPI. A Field Map is a complex MRI procedure that consists in acquiring two gradient echo images with different echo times (TE) and subtracting the phase between them ($\Delta\Phi$). The result is an image that represents the field-inhomogeneity (ΔB) [4] described by equation (2).

$$\Delta B(x, y, z) = \frac{\Delta\Phi(x, y, z)}{2\pi\gamma\Delta T_E} \quad (2)$$

where γ is the gyrometric ratio for hydrogen and ΔTE is the difference between the echo times of the phase images. Unfortunately, this method has the disadvantage of needing an extra acquisition and subsequently increasing the scan time.

2. SUJECTS AND METHODS

2.1 Real Data Acquisition

We acquired one DW-MRI volume for correction with a field strength coefficient (b-value) equal to 0 that corresponds to a simple EPI. We also acquired a Magnetization Prepared Rapid Gradient Echo (MPRAGE) image as a structural image for registration and a Gradient Echo Field Map for Field Map Correction.

2.2 Registration

For the registration process we chose 12 combinations of components, which are the most used in literature (see table 1). This process was implemented in *C++*, using the ITK library [2], where the components are already implemented. Registration was performed with the EPI data, using the MPRAGE data as reference image.

2.3 Pipeline for EPI correction

This pipeline consists in applying a Registration followed by a Field Map correction. The Field Map Correction was performed using FSL software [7] in particular FUGUE and PRELUDE. For comparison we applied the same Field Map correction to the original EPI, without registration.

2.4 Evaluation

Table 2: Evaluation of Correction Methods Results

	MI	Corr	CM	Dice GM	Dice WM
Reg1	0,6291	0,3809	2,172	0,5321	0,5899
Reg2	0,6311	0,3588	2,918	0,5472	0,6224
Reg3	0,6445	0,3623	2,624	0,5588	0,6321
Reg4	0,6288	0,3606	2,997	0,5460	0,6214
Reg5	0,6216	0,3787	2,160	0,5267	0,5799
Reg6	0,6317	0,3516	2,873	0,5450	0,6249
Reg7	0,6380	0,3881	2,787	0,5521	0,6298
Reg8	0,6308	0,3573	2,918	0,5459	0,6219
Reg9	0,6362	0,3679	2,663	0,5574	0,6440
Reg10	0,6114	0,3596	3,415	0,5263	0,5904
Reg11	0,6260	0,3633	3,020	0,5454	0,6181
Reg12	0,5947	0,3462	3,849	0,5043	0,5786
Field Map	0,6129	0,3199	3,801	0,5145	0,5954
Pipeline	0,6555	0,3886	2,969	0,5675	0,6440
Distorted EPI	0,5952	0,3153	3,721	0,4934	0,5753

GM Gray Matter; WM - White Matter

To evaluate the different registration methods and the proposed pipeline, we used four metrics: Mutual Information (MI), Squared Correlation Coefficient (Corr), Euclidean Distance of Centres of Mass (CM) and Dice Coefficient of the segmented images. All metrics were calculated between the corrected and the MPRAGE images. As control, metric values were also calculated between the original distorted EPI and the MPRAGE data. Segmentation was performed using FAST from FSL [7], and all evaluation metrics were calculated in Matlab®.

3. RESULTS AND DISCUSSION

After performing the 12 registration combinations, we calculated the evaluation metrics; the results can be seen in table 2. To choose the best registration, we performed a ranking of each metric. The ranks obtained for each metric were summed up and the methods with lowest sum of ranks were chosen, which in fact were Reg3, Reg7 and Reg9. To choose which registration method to use in the pipeline, we evaluated the correction time. The times were, respectively, 203.652, 140.653, 518.939 clock ticks. Consequently the combination Reg7 was chosen to perform the pipeline as it presents the lowest execution time.

After choosing the best registration process and performing resampling of Field Map to the MPRAGE space, we applied a Field Map Correction to both registered image and original data. The evaluation results are also shown in table 2 and we can see that they are suitable for the pipeline. As we can see in table 2, the pipeline always improves the correction for all considered evaluation metrics, when compared to the simple Field Map correction. This new pipeline also improves the results, when compared to the simple registration, except for CM. This might be related to an increase of the CM value produced by by the Field Map method. This increase was also verified in the simple Field Map correction, where the CM value is worse than in the Distorted EPI, influencing the pipeline results.

4. CONCLUSIONS

The results of the new proposed pipeline were better than the results obtained for simple Field Map and Registration, which indicates that the correction improves images. As future work we want to evaluate this correction pipeline for images with different b-values and analyze the effect of this

parameter in the correction process. In summary, this correction pipeline brings improvements to Field Map and Registration methods, and it is important for EPI images of any kind, including DW-MRI.

5. ACKNOWLEDGMENTS

The authors would like to thank the Brain Imaging Network in Portugal for the assistance in MRI data acquisition, especially Miguel Castelo-Branco, Gil Cunha, and Carlos Ferreira.

6. REFERENCES

[1] L. Baldwin, K. Wachowicz, and B. Fallone. A two-step scheme for distortion rectification of magnetic resonance images. *MEDICAL PHYSICS*, 36(9):3917–3926, 2009.

[2] I. S. Consortium. ITK - insight segmentation and registration toolkit, 2010.

[3] D. Holland, J. M. Kuperman, and A. M. Dale. Efficient correction of inhomogeneous static magnetic field-induced distortion in echo planar imaging. *NEUROIMAGE*, 50(1):175–183, 2010.

[4] P. Jezzard and R. S. Balaban. Correction for geometric distortion in echo planar images from b0 field variations. *MAGNETIC RESONANCE IN MEDICINE*, 34(1):65–73, 1995.

[5] P. Kostelec and S. Periaswamy. Image registration for MRI. *MSRI Publications*, 46, 2003.

[6] J. P. Pluim, J. B. A. Maintz, and M. A. Viergever. Interpolation artefacts in mutual information-based image registration. *Computer vision and image understanding*, 77(2):211–232, 2000.

[7] S. M. Smith, M. Jenkinson, M. W. Woolrich, C. F. Beckmann, T. E. Behrens, H. Johansen-Berg, P. R. Bannister, M. D. Luca, I. Drobnjak, D. E. Flitney, et al. Advances in functional and structural MR image analysis and implementation as FSL. *Neuroimage*, 23:S208–S219, 2004.